Government of Western Australia

Department of
Mines and Petroleum

REPORT
136

A MAGNETOTELLURIC SURVEY ACROSS THE KIMBERLEY CRATON, NORTHERN WESTERN AUSTRALIA

by J Spratt, MC Dentith, S Evans, ARA Aitken, M Lindsay, JA Hollis, IM Tyler, A Joly, and J Shragge

Centre for EXPLORATION TARGETING

Moombarriga Geoscience

The University of Western Australia
Achieving International Excellence

Geological Survey of Western Australia

Government of **Western Australia**
Department of **Mines and Petroleum**

REPORT 136

A MAGNETOTELLURIC SURVEY ACROSS THE KIMBERLEY CRATON, NORTHERN WESTERN AUSTRALIA

by
J Spratt[1], MC Dentith[2], S Evans[3], ARA Aitken[2], M Lindsay[2], JA Hollis, IM Tyler, A Joly[2], and J Shragge[4]

1 Consultant, Wakefield, Quebec, Canada
2 Centre for Exploration Targeting, The University of Western Australia, 35 Stirling Hwy, Crawley WA 6009, Australia
3 Moombarriga Geoscience, Box 1184, West Perth WA 6872, Australia
4 Centre for Petroleum Geoscience and CO2 Sequestration, The University of Western Australia, 35 Stirling Hwy, Crawley WA 6009, Australia

Perth 2014

Geological Survey of Western Australia

REFERENCE
The recommended reference for this publication is:
Spratt, J, Dentith, MC, Evans, S, Aitken, ARA, Lindsay, M, Hollis, JA, Tyler, IM, Joly, A and Shragge, J 2014, A magnetotelluric survey across the Kimberley Craton, northern Western Australia: Geological Survey of Western Australia, Report 136, 92p.

National Library of Australia Cataloguing-in-Publication entry:

Author:	Spratt, J. author.
Title:	A magnetotelluric survey across the Kimberley craton,northern Western Australia / J Spratt, MC Dentith, S Evans, A Aitken, M Lindsay, JA Hollis, IM Tyler, A Joly, J Shragge.
ISBN:	9781741685626 (ebook)
Subjects:	Magnetotelluric prospecting--Western Australia--Kimberley. Geological surveys--Western Australia--Kimberley.
Other Authors/Contributors:	Dentith, Mike, author. Evans, Shane, author. Aitken, Alan, author. Lindsay, M., author. Hollis, J. A., author. Tyler, I. M., author. Joly, Aurore, author. Shragge, J., author. Geological Survey of Western Australia, issuing body.
Dewey Decimal Classification:	622.15309941

ISSN 1834–2280

Grid references in this publication refer to the Geocentric Datum of Australia 1994 (GDA94). Locations mentioned in the text are referenced using Map Grid Australia (MGA) coordinates, Zones 51 and 52. All locations are quoted to at least the nearest 100 m.

Copy editor: RL Hitchings
Cartography: M Prause, AK Symonds
Desktop publishing: RL Hitchings
Printed by Images on Paper, Perth, Western Australia

Published 2014 by Geological Survey of Western Australia
This Report is published in digital format (PDF) and is available online at <www.dmp.wa.gov.au/GSWApublications>.

Further details of geological publications and maps produced by the Geological Survey of Western Australia are available from:
Information Centre
Department of Mines and Petroleum | 100 Plain Street | EAST PERTH | WESTERN AUSTRALIA 6004
Telephone: +61 8 9222 3459 Facsimile: +61 8 9222 3444 **www.dmp.wa.gov.au/GSWApublications**

Cover photograph: Programming magnetotelluric acquisition equipment in the north Kimberley

Contents

Figures

Table

A magnetotelluric survey across the Kimberley Craton, northern Western Australia

by

J Spratt[1], MC Dentith[2], S Evans[3], A Aitken[2], M Lindsay[2], JA Hollis, IM Tyler, A Joly[2], J Shragge[4]

Abstract

Magnetotelluric soundings at 155 locations throughout the Kimberley region have provided two-dimensional (2D) conductivity models of the crust and uppermost lithospheric mantle beneath four regional transects and four local transects. Dimensionality and geoelectric strike analysis on these data reveal variable strike directions from west to east across the survey area. 2D modelling reveals a near-surface conductive layer up to 5 km in thickness, interpreted as the volcanic and sedimentary rocks of the Kimberley Basin, which is underlain by a resistive upper crust to depths of 15–35 km. Several steeply dipping, less resistive features are revealed in the upper crust that correlate with the location of faults mapped in the central Kimberley Basin, and with major structural boundaries within the King Leopold and Halls Creek Orogens. Regionally, a conductive lower crust is imaged that appears to be discontinuous at, or near, major inferred crustal block boundaries. Along the eastern margin of the Kimberley Basin, a northwestward-dipping resistive slab extending from the surface to at least 60 km depth is interpreted as ancient lithospheric material subducted during collisional orogenesis associated with the Halls Creek Orogeny. The variable electric strike directions suggest the need for 3D modelling of the data.

KEYWORDS: Bouguer anomaly maps, geophysical models, magnetotelluric surveys, TMI maps

Introduction

A magnetotelluric (MT) survey has been completed in the Kimberley region in northern Western Australia, funded by the Kimberley Science and Conservation Strategy and administered by the Geological Survey of Western Australia (GSWA). The general aim of the survey was to identify and map major structures in the deep crust and upper mantle. The principal reason for the survey was to address a major information gap regarding the concealed basement of the Kimberley Craton, and the geometry of the major tectonic structures within the craton and the adjacent King Leopold and Halls Creek Orogens. Information on the geometry of these structures is limited due to a cover of younger rocks.

1 Consultant, Wakefield, Quebec, Canada

2 Centre for Exploration Targeting, The University of Western Australia, 35 Stirling Hwy, Crawley WA 6009, Australia

3 Moombarriga Geoscience, Box 1184, West Perth WA 6872, Australia

4 Centre for Petroleum Geoscience and CO2 Sequestration, The University of Western Australia, Crawley WA 6009, Australia

The MT method is a deep-penetrating, natural source electromagnetic technique used to image the electrical conductivity structure of the Earth's crust and upper mantle. MT has been shown to be a useful tool in mapping the deep lithosphere beneath Archean terranes, for example, the Slave Craton in northern Canada (Davis et al., 2003; Jones et al., 2003), the Kaapvaal Craton in South Africa (Muller et al., 2009; Jones et al., 2009b; Evans et al., 2011), and the Yilgarn Craton (Dentith et al., 2013). The MT method has been successfully applied to mapping ancient orogenic sutures in Australia, North America and Europe, such as the Trans Hudson Orogen (Jones et al., 1993; Jones et al., 2005) and Iapetus Suture (Banks et al., 1996); in delineating major terrane boundaries, such as between the Wopmay Orogen and the Slave Craton (Spratt et al., 2009); and identifying major lithospheric structures such as the Great Slave Lake Shear Zone (Wu et al., 2002), and faults beneath the Melville Peninsula of the Rae Craton (Spratt et al., 2013a).

For this study, MT data were acquired at 155 locations, comprising four regional and four local traverses crossing the King Leopold Orogen to the southwest, the Halls

Creek Orogen to the southeast and extending northward across the central part of the Kimberley Craton (Fig. 1). This Report describes the data processing, analysis, 2D modelling and interpretation of these data. Analysis and modelling of the MT data region reveal major structures in the deep crust and upper lithospheric mantle that provides important information on the tectonic framework of the region and its prospectivity at the regional scale.

Regional geology

The regional geology and tectonic history of the study area is summarized in the map and time–space diagram in Figure 2. The outcropping geology of the Kimberley region is dominated by flat-lying fluvial and shallow marine sandstones of the Paleoproterozoic Speewah and Kimberley Basins. Sediments of the Speewah and Kimberley Basins were deposited onto the denuded Paleoproterozoic Lamboo Province — exposed in the Halls Creek and King Leopold orogenic belts that outcrop at the basin margins (Figs 1 and 2) — and possibly also onto an older, unexposed Archean crustal block. The unexposed basement to the Speewah and Kimberley Basins is known as the Kimberley Craton. The Speewah and Kimberley Basins are in part overlain by younger, Paleo-, Meso- and Neoproterozoic sedimentary rocks including the c. 1200 Ma Carr Boyd Group in the northeast Halls Creek Orogen (Pidgeon et al., 1989) and the 635–560 Ma Mount House Group in the south central Kimberley (Coats and Preiss, 1980). The Lamboo Province and the margins of the Speewah and Kimberley Basins were deformed and metamorphosed during several orogenic events: the c. 1835 to 1810 Ma Halls Creek Orogeny (Tyler et al., 1995; Blake et al., 2000; Bodorkos et al., 2000; Page et al., 2001; Sheppard et al., 2001); the c. 1000–800 Ma Yampi Orogeny (Tyler and Griffin, 1990; Shaw et al., 1992; Griffin et al., 1993; Bodorkos and Reddy, 2004); and the c. 560 to 530 Ma King Leopold Orogeny (Tyler and Griffin, 1990; Shaw et al., 1992; Griffin et al., 1993).

The Precambrian rocks of the Kimberley region are unconformably overlain by Phanerozoic sedimentary rocks. In the east these comprise the Ord and Southern Bonaparte Basins. The Ord Basin deposits are of Cambrian to Devonian age and overlie the Halls Creek Orogen (Fig. 2). In the survey area the Ord Basin is represented mainly by mafic volcanic rocks of the 510 Ma Antrim Plateau Volcanics (Hanley and Wingate, 2000; Glass and Phillips, 2006). In the area of the MT survey the Antrim Plateau Volcanics are unconformably overlain by the lowermost units of the onshore Southern Bonaparte Basin, specifically the late Devonian clastic and carbonate sediments of the Cockatoo Formation. The deposits in the Ord and Southern Bonaparte Basins are probably only some hundreds of metres thick in the survey area (Mory, 1990a,b) and as such will have little influence on the MT data. Immediately adjacent to the King Leopold Orogen is the Lennard Shelf, which is part of the Canning Basin. Further to the southwest, across the Pinnacle Fault system, is the deep (>10 km) Fitzroy Trough. The sediments of the Canning Basin unconformably overlie the King

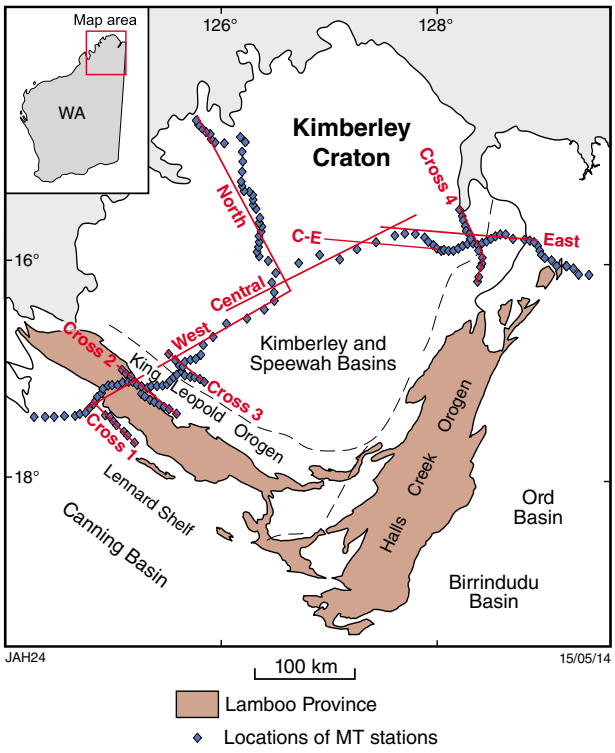

Figure 1. Map of the main geological elements of the Kimberley region in Western Australia (Tyler et al., 2012). The blue symbols mark the location of the MT stations. The solid red lines show the location of 2D model profiles.

Leopold Orogen rocks and also granitic basement inliers of the Lennard Shelf. The Fitzroy Trough is a structural and depositional basin with sediments varying in age from early Paleozoic to late Mesozoic (Kennard et al., 1994). It contains mainly Upper Paleozoic clastic and carbonate sediments. The Canning Basin has a complex tectonic history with several phases of extension and transpression/transtension recognized (Shaw et al., 1995). The geological affinity of the basement to the Canning Basin is unknown, various types of metamorphic rocks having been intersected in a handful of exploration wells.

Basement of the Kimberley Craton

The Kimberley Craton is one of several crustal blocks that together form the Archean to Proterozoic North Australian Craton (Myers et al., 1996; Betts et al., 2002; Betts and Giles, 2006; Cawood and Korsch, 2008). It has been proposed that an Archean Kimberley Craton was a stable root against which the adjacent Proterozoic orogenic domains were deformed (Gellatly, 1971; Griffin et al., 2000). Alternatively, it has been suggested that the Proterozoic domains extend beneath the Kimberley Basin (Plumb and Gemuts, 1976; Gunn and Meixner, 1998; Downes et al., 2007).

As there is no known outcrop of the basement beneath the Kimberley Basin, its nature must be inferred indirectly. Indirect evidence for the nature of the basement includes isotopic data for granites of the 1865–1850 Ma Paperbark Supersuite, along the inferred margin of the Kimberley Craton (Griffin et al., 2000), for granite xenoliths within the Aries kimberlite in the central Kimberley (Downes et al., 2007), and for the Argyle Lamproite and Seppelt kimberlite (Graham et al., 1999). These indicate that partial melting of Archean crust must have played a role in their formation, and thus the unexposed Kimberley Craton probably has an Archean component. Collins et al. (2003) compared the 1D seismic velocity structure under the Kimberley Craton with that of the Yilgarn and Pilbara Cratons, concluding that they exhibit the same characteristics and so suggest that there is Archean crust in the Kimberley. Saygin and Kennett (2012) presented continental-scale, shear-wave velocity models obtained from ambient noise tomography. The Kimberley Craton is characterized by high wave speeds, similar to the Archean Pilbara and Yilgarn Cratons.

Conversely, unpublished work by Stockdale Prospecting supports the presence of Paleoproterozoic crust beneath the basin. Granite sampled by Stockdale Prospecting near Carey Creek is interpreted as outcropping basement. U–Pb dating of zircon yielded an age of 1867 ± 10 Ma (contemporaneous with the early stages of the Hooper Orogeny and emplacement of the Paperbark Supersuite of the Lamboo Province), which was interpreted as the age of crystallization and emplacement of the granite (RT Pidgeon, unpublished data, 1987; B Wyatt, pers comm., 2013).

There is also evidence for (pre-Lamboo Province) Paleoproterozoic terranes in the Kimberley Craton. Tyler et al. (1999) analysed detrital zircons from the c. 1870 Ma Marboo Formation, the oldest unit in the western zone of the Lamboo Province. The zircons provide information about the source terrain, inferred to be the unexposed Kimberley Craton. Detrital zircons were dated at 2500–2400, 2300, 2200–2050, 1970, and 1910 Ma. The data shows the source is largely early Paleoproterozoic in age, rather than Archean as previously assumed. The composition of the metasedimentary rocks suggests a source comprising mature continental crust and recycled orogens or magmatic-arcs. The spread in ages indicates that the time between the formation of Neoarchean basement in northern Australia, and the formation of the Paleoproterozoic orogens, was marked by ongoing crust formation and crustal reworking.

The Lamboo Province

The Lamboo Province formed between 1910 and 1790 Ma and includes deformed and metamorphosed plutonic, volcanic, and sedimentary units. The Lamboo Province is divided into three tectonostratigraphic terranes: the western, central, and eastern zones are defined by their geological histories and are bounded by major fault systems (Figs 1 and 2; Tyler et al., 1995, 2012). The western zone includes turbiditic metasedimentary rocks of the c. 1870 Ma Marboo Formation and is dominated by 1855–1850 Ma felsic volcanic rocks of the Whitewater Volcanics and cogenetic granites of the 1865–1850 Ma Paperbark Supersuite with accompanying mafic and ultramafic intrusive bodies. These rocks are thought to have formed by partial melting of Paleoproterozoic to Archean intermediate to felsic, calc-alkaline rocks along the Kimberley margin in an extensional setting (Sheppard et al., 1999, 2001; Griffin et al., 2000). The central zone includes deformed and metamorphosed mafic volcanic rocks, volcaniclastics, and turbidites of the 1865 Ma Tickalara Metamorphics. These rocks, intruded by sheets of 1850–1845 Ma tonalite, have been interpreted to represent an island-arc environment along the margin of the Kimberley Craton above a southeasterly dipping subduction zone (Sheppard et al., 1999). The central zone also includes mafic and felsic volcanic rocks, as well as sedimentary rocks of the 1843 Ma Koongie Park Formation, possibly formed in a rifted-arc or back-arc setting (Page et al., 1994; Orth, 2002; Tyler et al., 2005). The eastern zone comprises siliciclastic sedimentary rocks, and mafic and volcanic rocks of the Halls Creek Group, deposited between 1910 and 1845 Ma on the passive continental margin of the North Australian Craton.

The central and eastern zones were intruded by syntectonic granite plutons of the 1835–1805 Ma Sally Downs Supersuite. Granitic magmatism accompanied a period of deformation and medium- to low-grade regional metamorphism of the Halls Creek Orogeny, marking the amalgamation of the eastern zone with the already combined western and central zones (Tyler et al., 1995).

Speewah and Kimberley Basins

The siliciclastic rocks of the 1.5 km-thick Speewah Group were unconformably deposited in the 1835 Ma Speewah Basin during the Halls Creek Orogeny and overlie the western zone of the Lamboo Province (Sheppard et al., 2012; Tyler et al., 2012). The Speewah Group thins to the west and is overlapped by the Kimberley Group in the southeast. The Speewah Basin is believed to have formed in a retro-arc foreland basin behind the active arc on the eastern margin of the Kimberley Craton (Sheppard et al., 2012). The 4 km-thick Kimberley Group was deposited at c. 1800 Ma in the post-collisional, shallow marine Kimberley Basin, and comprises siliciclastic sedimentary rocks and mafic volcanic rocks that disconformably overlie the Speewah Group and the Lamboo Province (Gellatly et al., 1970). Outside of the Halls Creek and King Leopold Orogens, the Kimberley Basin succession is relatively undeformed and has a low metamorphic grade (Tyler and Griffin, 1990).

The Speewah and lower Kimberley Groups are intruded by the 1797 Ma Hart Dolerite, a network of connected massive dolerite sills and dykes with some granophyres. These intrusive bodies resulted from a post-collisional magmatic event and were generated from subduction-modified mantle beneath the Kimberley Craton (Sheppard et al., 2012). The c. 1800 Ma Carson Volcanics, exposed through the central part of the Kimberley Basin, range in thickness from 400–1100 m and consist mainly of tholeiitic basalts interlayered with sandstone, siltstone and chert, and locally have disseminated sulfides.

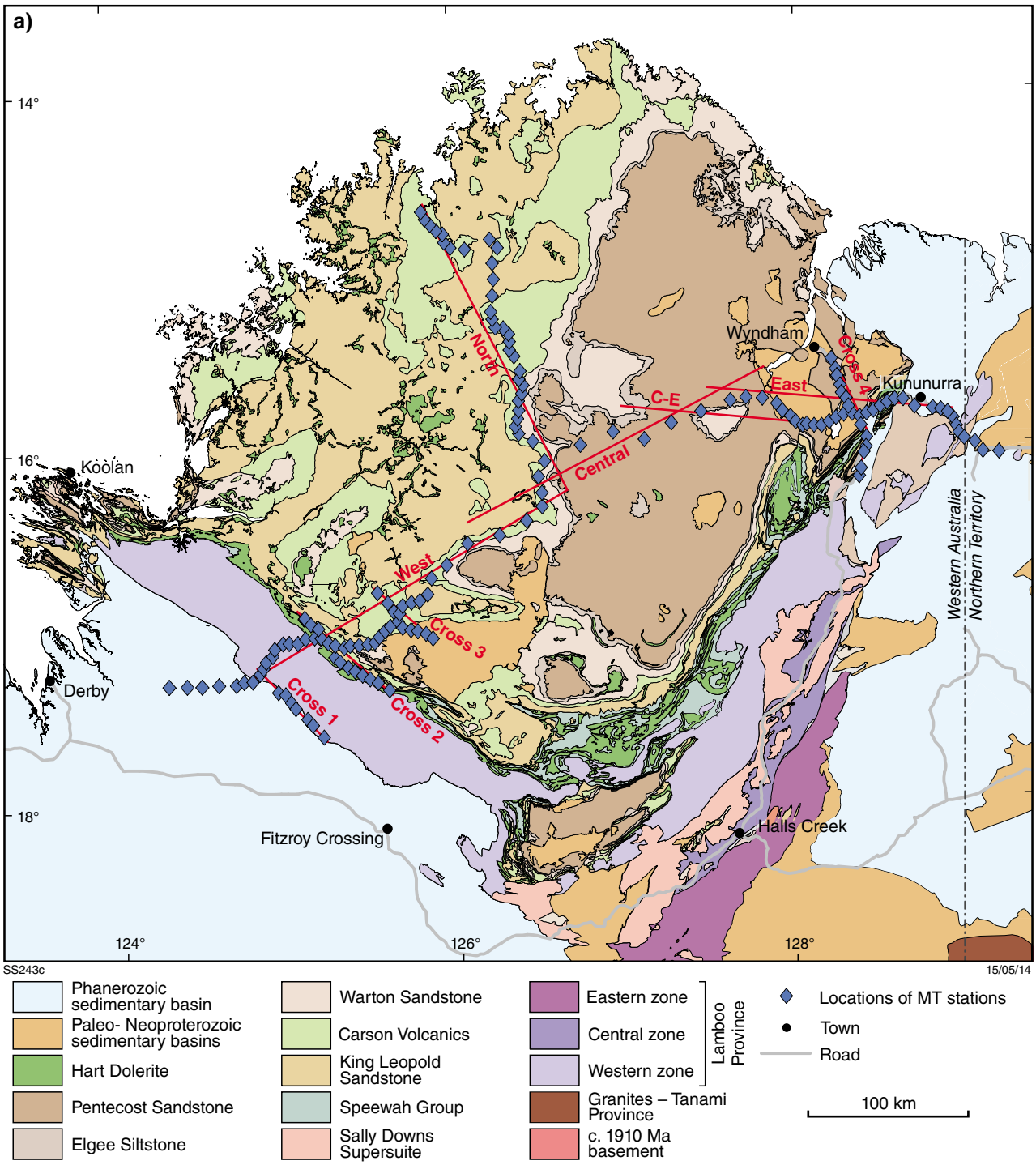

Figure 2. a) Summary geological map for the Kimberley region; b) (facing) time–space diagram. Dmd = diamond

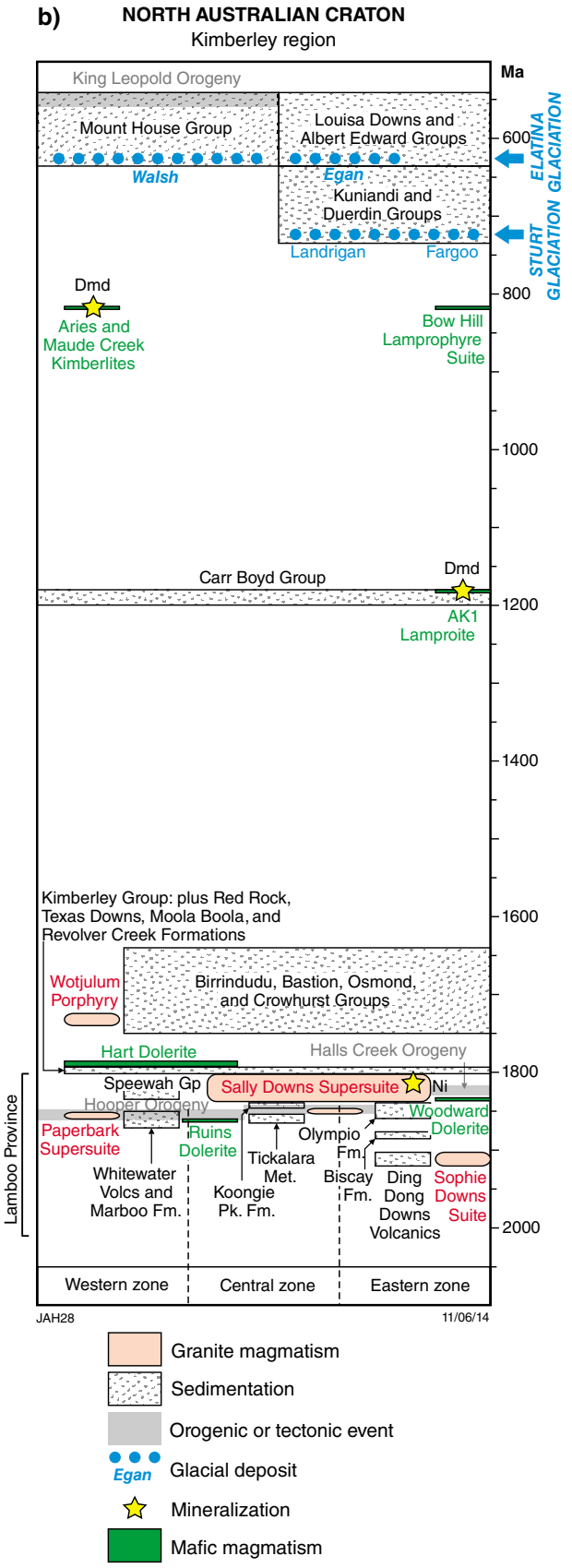

Paleoproterozoic orogenesis

The Paleoproterozoic tectonic evolution of the Kimberley Craton margin involved a series of collision and accretion events in the period 1870–1805 Ma. The 1870–1850 Ma Hooper Orogeny involved deformation associated with mafic and felsic magmatism, producing voluminous granites of the Paperbark Supersuite that intruded the c. 1870 Ma Marboo Formation in the western zone. The final stages of the Hooper Orogeny saw accretion of the c. 1865 Ma Tickalara Metamorphics oceanic-arc of the central zone, onto the Kimberley Craton margin (Tyler and Page, 1996; Sheppard et al., 1999). This was followed by the 1835–1810 Ma Halls Creek Orogeny, which marked the collision between the Kimberley Craton to the northwest and the North Australian Craton to the southeast (Tyler et al., 1995, 2012; Myers et al., 1996; Tyler and Page, 1996; Sheppard et al., 1999). The Halls Creek Orogen involved west-dipping subduction, collision and suturing of the two cratons by 1810 Ma (Tyler and Page, 1996; Sheppard et al., 1997, 2001).

Neoproterozoic orogenesis

The Speewah and Kimberley Basins were deformed along their margins during the c. 1000–800 Ma Yampi Orogeny, though the central parts of the basin remain undeformed. The Yampi Orogeny produced large-scale, north-directed thrusts and folds of the Kimberley Basin on the Yampi peninsula, with thrusts traceable into steeply dipping northwest-striking shear zones in the western zone of the Lamboo Province (Tyler and Griffin, 1990, 1993; Shaw et al., 1992; Griffin et al., 1993; Bodorkos and Reddy, 2004). The Yampi Orogeny also resulted in strike-slip faulting in the Halls Creek Orogen (White and Muir, 1989; Tyler et al., 1995; Thorne and Tyler, 1996).

The Neoproterozoic King Leopold Orogeny produced southwest-directed thrusts and folds in the King Leopold Ranges (Precipice Fold Belt), along the southwest margin of the Kimberley Basin. These folds and thrusts deformed sedimentary rocks of the Kimberley Basin and the overlying Mount House Group and persist up to 100 km into the basin. One of these thrusts, the Inglis Fault, marks the basal contact of the Speewah Basin with the underlying Lamboo Province and is a major west-northwest striking, steeply northeast-dipping structure (Griffin and Myers, 1988; Tyler and Griffin, 1990, 1993). The King Leopold Orogeny also resulted in reactivation of shear zones in the Lamboo Province of the King Leopold Orogen and sinistral strike-slip faulting in the Halls Creek Orogen (Tyler and Griffin, 1990, 1993; Shaw et al., 1992; Griffin et al., 1993; Thorne and Tyler, 1996).

Regional geophysical studies

Gravity and aeromagnetic data

Regional gravity and magnetic data (Fig. 3) provide some clues about the basement beneath the Speewah and Kimberley Basins (Gunn and Meixner, 1998). Inferring basement structure from the geophysical data is hindered by the presence of thick, and geographically extensive, mafic rocks in the basin sequences (Hart Dolerite, Carson Volcanics) which dominate the magnetic response, and complicate the interpretation of gravity data. Clear positive magnetic anomalies occur parallel and adjacent to the Halls Creek Orogen and as a subcircular feature near the centre of the exposed Kimberley Basin. Filtering these data to suppress short wavelength variations, mostly originating in the uppermost crust, produced an image with mostly northeast–southwest trends but with evidence of termination and offset of these trends by orthogonal structures (Fig. 3b). Gravity data from the area are of low resolution (typically 11 km station spacing) and hence, are likely to contain aliased signals. Again, positive anomalies are seen adjacent to the Halls Creek Orogen and there is a distinct zone of higher values, with a northeast-trending margin in the northwestern part of the Kimberley Basin. Gunn and Meixner (1998) present a map of interpreted basement features, recognizing five zones (A–E), which form northeast-trending corridors (Fig. 4a). 2.5D models of crustal density and magnetic susceptibility variations consistent with the observed anomalies are also presented (Fig. 4b). Zone A, adjacent to the Halls Creek Orogen, contains coincident gravity and magnetic highs which are modelled as 30° northwest-dipping sheets. The margin of the northwestern edge of the granites of the Halls Creek Orogen is also shown as dipping to the northwest. Gunn and Meixner (1998) speculate that the dense and magnetic sheets comprise an ophiolite complex. Zone B has both low gravity and low total magnetic intensity (TMI). Gunn and Meixner (1998) suggest it is an area of granitic basement. Zone C contains several coincident magnetic highs and gravity lows, and sources comprising magnetic granites are proposed. Magnetic data show anomalies consistent with mafic dykes extending across the whole Kimberley Basin. The lateral extent of these features suggests fractures penetrating very deep into the crust. Zone D comprises elongate anomalies with poor correspondence between gravity and magnetic responses. A granitic basement terrain is interpreted. Zone E is characterized by high gravity, which Gunn and Meixner (1998) associate with crustal thinning due to offshore basin formation. However, the zone has a sharp boundary with Zone D suggesting structural control, which is supported by several very long dyke-related magnetic responses indicative of deep-penetrating structures.

Seismic data

Fishwick et al. (2005) discuss results of surface wave tomographic models of lithospheric structure beneath the Australian continent. Similar to the Yilgarn Craton, the Kimberley Craton is characterized by fast S-wave velocities to about 250 km depth, consistent with a cold, thick lithospheric root. The region of fast velocities extends further to the south from where the Kimberley Craton has been mapped from the surface geology. Fishwick et al. (2005) interpret the fast velocities as Archean lithosphere, consistent with isotopic data from diamondiferous kimberlites that indicates an Archean source beneath the Kimberley Craton (Downes et al., 2007).

Clitheroe et al. (2000) determined crustal thicknesses of the Australian continent using passive seismic receiver functions. Crustal thicknesses beneath the Kimberley Craton range from about 38 km along the southwest margin to 45 km along its southeastern margin, with a 2–10 km wide Moho transition zone. These thicknesses are consistent with those observed throughout the North Australian Craton. However, there are no estimates beneath the central or northern region of the Kimberley Craton. A much shallower estimate of 29 km Moho depth was returned for station KA02, near MT station 120 (Fig. 3). This may indicate Bonaparte Gulf rifting processes in the Phanerozoic.

Magnetotellurics

Magnetotelluric (MT) theory

MT is a geophysical method that involves measuring and relating natural time-varying electric and magnetic fields, induced by the interaction between the Earth's geomagnetic field and solar winds, and by worldwide thunderstorms, in order to resolve the electrical conductivity structure of the subsurface of the Earth (Cagniard, 1953; Wait, 1962). The relationship between these horizontal and mutually perpendicular fields recorded at each station provides amplitude (apparent resistivity) and phase lags as a function of frequency (or period, the inverse of frequency), commonly referred to as MT response curves (Fig. 5). With increasing depth there is an exponential decrease in the amplitudes of the electromagnetic fields, the so-called skin-depth phenomenon. The depth of penetration (or skin depth) of these fields is directly related to frequency (the lower the frequency, the greater the depth) and the resistivity of the material (the greater the resistivity, the greater the depth). This means estimates of resistivity versus depth can be made beneath each site based on the MT response curves. For this reason, during the description of the processing and interpretation of the MT data, period can be thought of as a proxy for depth. However, since the conductivity of the Earth varies from location to location, so the conversion factor from period to depth will also vary. In order to image the deep mantle lithosphere, long periods must be sampled requiring recording times of tens of hours.

Prior to 2D modelling, MT data are typically analysed to determine the regional geoelectric strike direction as well as the degree of dimensionality in order to generate an accurate representation of a 2D Earth. Where the Earth is

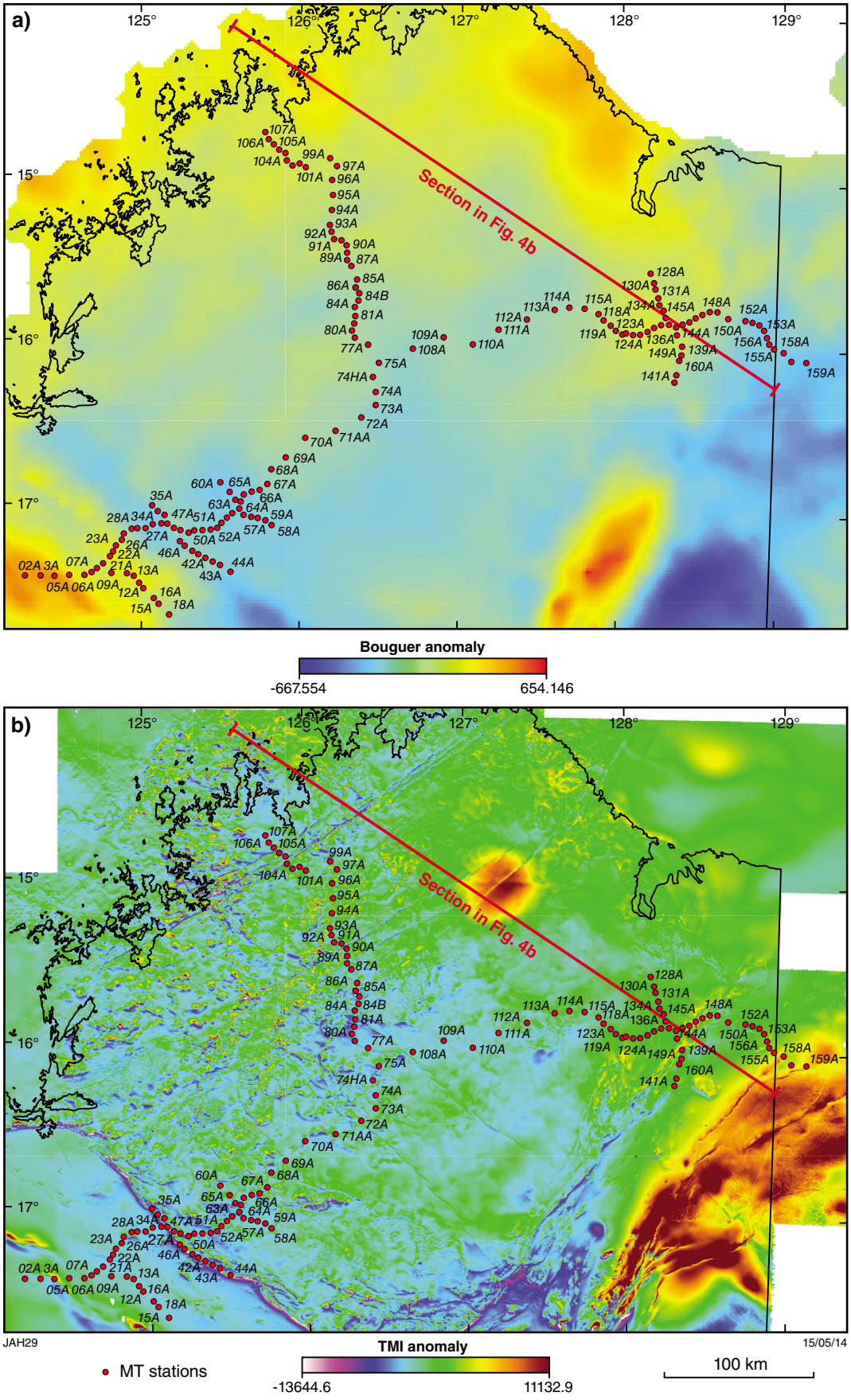

Figure 3. **a) Bouguer gravity data; b) magnetic (total intensity) data for the Kimberley region. The MT station locations are indicated by the red circles.**

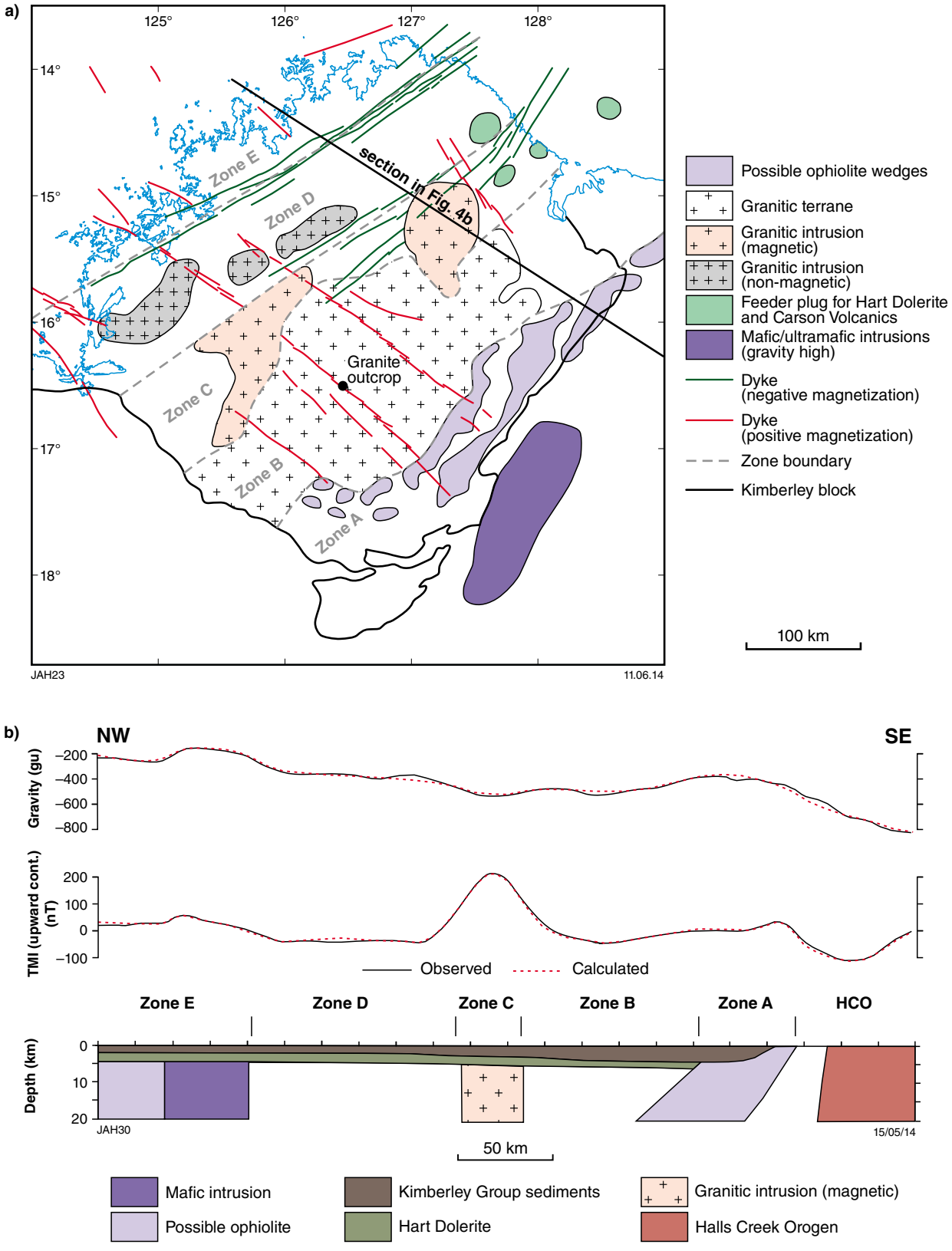

Figure 4. **a) Interpreted basement geology; b) 2.5D model of gravity and magnetic data, from the Kimberley Basin. Redrawn from Gunn and Meixner (1998)**

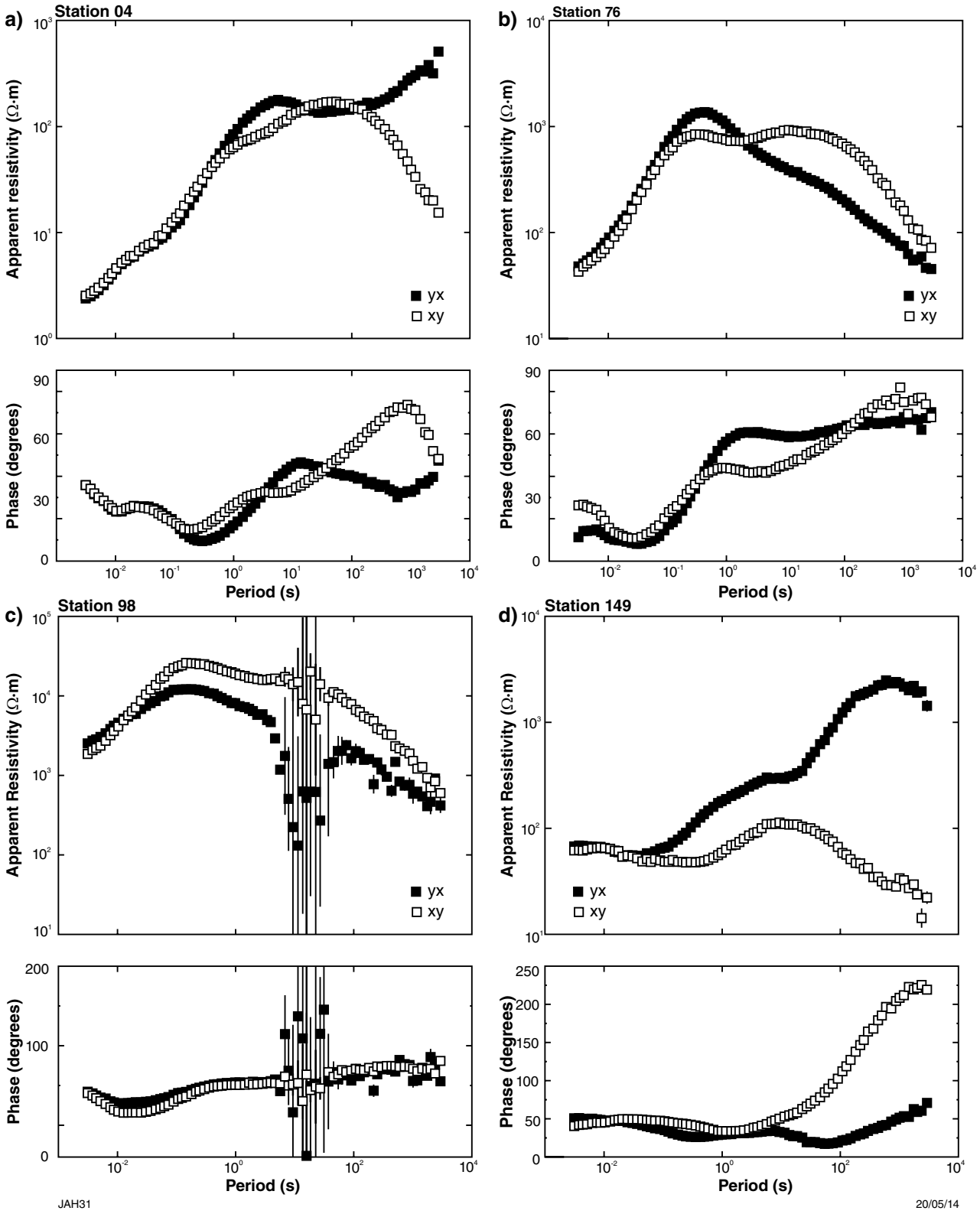

Figure 5. Examples of MT response curves. The open squares show data measured in the north–south direction (XY response) and the closed squares show data measured in the east–west direction (the YX response): a) an example of excellent data, station 04; b) a second example of excellent data, station 76; c) an example of poor-quality data in the MT dead band, station 98; d) an example of out-of-quadrant phases at long periods, station 149. See Figure 3 for station locations.

1D, the conductivity structure is layered and independent of the geoelectric strike direction. Within an electrically 2D Earth, conductivity varies laterally so that the apparent resistivity is different along and across the geological, or more correctly, geoelectrical strike. Apparent resistivities and phases need to be calculated in both directions (or modes). The transverse-electric (TE) mode describes current flowing parallel to geoelectric strike and is predominantly sensitive to current concentration and flow patterns. The transverse-magnetic (TM) mode describes current flow perpendicular to strike and is more sensitive to charges induced on lateral boundaries.

For a comprehensive description of the MT method, refer to Chave and Jones (2012), and Simpson and Bahr (2005).

Causes for electrical conductivity variation

The MT method is sensitive to contrasts in the resistivity of different materials and can therefore distinguish between some lithological units and can image structural and compositional features at depth. Typical Archean granulite facies rocks, for example, commonly have high electrical resistivity values >1000 Ω•m (Wu et al., 2002), whereas sedimentary rocks are less resistive, with values ranging between 10 and 1000 Ω•m. Figure 6 summarizes conductivity variations in major crustal layers as derived from MT surveys and laboratory measurements of various rock types and constituents. Note the general three-layer classification of very resistive upper crust, a less resistive lower crust and a resistive mantle.

At crustal depths, factors that can considerably reduce typical resistivity values include changes in mineralogy, or the presence of saline fluids (Haak and Hutton, 1986; Jones, 1992). Regardless of the type of conducting material, it is important to recognize that interconnectivity of the conducting elements is a key control on the bulk conductivity of a material. If this occurs, only small amounts of the conductive component of the material are required.

At mantle depths, the electrical characteristics reflect the electrical properties of olivine. Similar to crustal responses, a major problem in understanding electrical responses from the mantle is that laboratory measurements on olivine suggest the observed resistivity of the mantle should be much higher than is derived from MT measurements. The bulk conductivity of the mantle lithosphere is predominantly attributed to its temperature and composition. Typical values of 1000–10 000 Ω•m are observed in MT studies around the world (Eaton et al., 2009), with the resistivity of dry olivine decreasing with increasing temperature, approximately one order of magnitude for every 200–300°C (Constable, 2006). The most commonly proposed causes for anomalously enhanced conductivity in the subcontinental upper mantle include presence of interconnected conducting phases such as graphite, sulfides, or thin carbon films (Duba and Shankland, 1982; Ducea and Park, 2000; Poe et al., 2010), fluids (either brine or partial melt; Glover et al., 2000), a reduction in grain size (ten Grotenhius et al., 2004), ambient temperature variations (Ledo and Jones, 2005), oxygen fugacity (Constable, 2006), increased iron content (Jones et al., 2009a), and bonded water through hydration (Karato, 1990, 2006; Jones et al., 2012).

MT-derived resistivity models, by nature, are not unique; however, the highest resolution is observed when imaging the top of a low resistivity layer. One limitation of the method is that it is sensitive to the product of conductivity and thickness, i.e. conductance, but cannot resolve the two factors independently — apparent broad regions of enhanced conductivity may in fact be caused by quite thin zones of high conductivity. Also to be considered is that continuous networks of conductive material, of whatever type, over the very large areas where enhanced conductivity is observed, are hard to explain, as is maintaining their continuity over geological time scales.

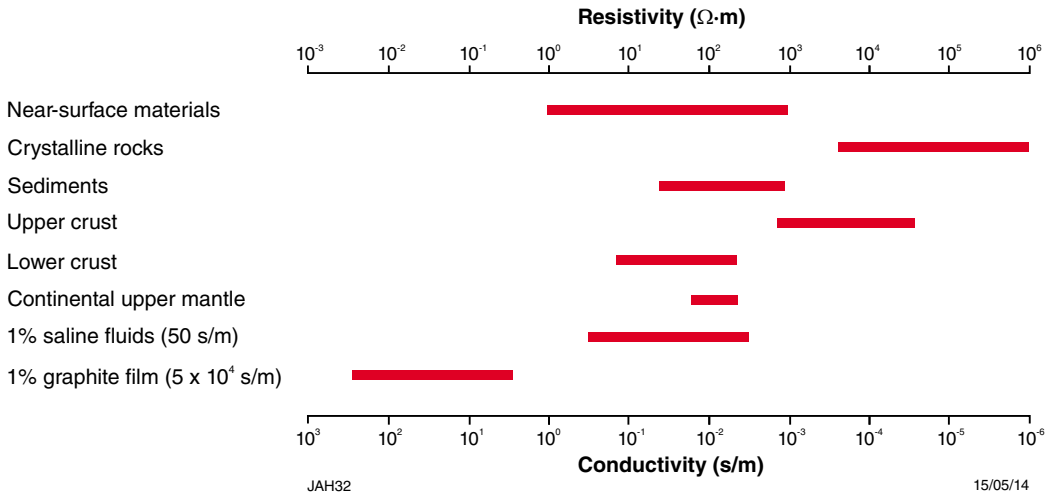

Figure 6. Resistivity ranges of selected geological entities and materials. Redrawn from Jones (1999) with additions

Magnetotelluric data acquisition and analysis

Data acquisition

The MT data were collected in a single campaign by personnel from Moombarriga Geoscience, the Centre for Exploration Targeting at the University of Western Australia, and GSWA. Data from 155 sites were collected between 18 May and 20 July 2012. Station spacing varied from 5 to 20 km, being smaller in areas where, based on analysis of gravity and magnetic data, major structures/boundaries were considered most likely. Time-domain electromagnetic soundings were made at each MT station comprising the traverses. Coordinates and acquisition times for all the MT stations are given in Table 1.

Figure 7 is a schematic illustration of the equipment layout at each MT station. Two horizontal components of the electric field, and three components of the magnetic field variation, were measured at each site for approximately 40 hours. In general, survey sites were relatively flat and most sites were remote from any sources of cultural electromagnetic noise. Due to disturbances from cattle and wild dogs, some sites recorded for less than 40 hours and some were repeated. Data were recorded using Phoenix Limited MTU-5A data recorders with MTC-50 or MTC-80 magnetic induction coils. The coils are sensitive to noise; this is reduced by burying them, a significant task especially for a vertical coil since it is approximately 2 m in length. Electric dipoles and horizontal coils were installed in magnetic north–south and east–west azimuths and the electric dipoles at all sites were approximately 100 m in length. The electric field was measured using non-polarizing ($Pb/PbCl_2$ solution) electrodes. These consist of a container with a porous base and filled with an electrolyte solution, which provides electrical contact with the ground.

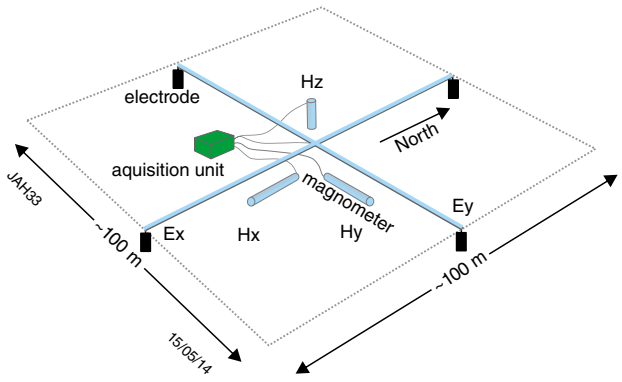

Figure 7. Schematic illustration of equipment layout at each MT station. E = electric field sensor; H = magnetic field sensor

Electromagnetic soundings were made using a TerraTEM transmitter and receiver. A 100 m-sided square transmitter loop (Tx area = 10 000 m^2) was used with sides oriented north–south/east–west. The receiver coil had an effective area of 1000 m^2. The TerraTEM 'intermediate' time series was used (135 channels between 0.0015 and 1900 ms). A minimum of four soundings were made at each site. Visual checks were made to ensure these data were self-consistent and not obviously noisy, with additional soundings made if necessary.

Data processing

Variations of the electric and magnetic field components are recorded as a function of time, i.e. these data comprise time series and are in the 'time domain'. The MT data are subsequently converted to the 'frequency domain'. This enables parameters of interest to be calculated as a function of frequency (or period) and subsequently used to model electrical property variations as a function of depth.

Examples of partial electric and magnetic field time series from station 135 are shown in Figure 8. These time series can be checked in the field to ensure that there has been adequate variation in the geomagnetic field for the data to be useful, and also to check that the equipment has been deployed correctly, as can be determined by the relationships between the different time series. Electric field measurements are designated E, and the north–south component is termed Ex, and the east–west component Ey. Magnetic field components are designated as H, with the same notation, and Hz defining the vertical component.

The time-series data were processed using robust remote-reference algorithms supplied by Phoenix Limited and based on the coherence-sorted cascade decimation method of Wight and Bostick (1981), and the heuristic robust approach of Jones and Jödicke (1984). Remote reference processing (Gamble et al., 1979) compares recordings from different locations to identify noise in the time series, while the coherence-based methods are based on statistical comparison of the various time series. In this case, the remote reference used was a simultaneously recording station within the traverse.

Magnetotelluric response curves

The data in the frequency domain are typically presented as MT response curves, plotting the apparent resistivity and phase as a function of period (Fig. 5). Note that electrical resistivity (ρ or rho) is the reciprocal of electrical conductivity (σ) and that period (s) is the reciprocal of frequency (Hz). In general, at 127 of the 155 sites acquired, the MT data quality from the Kimberley region is excellent with little scatter and small error bars over a broad period range of 0.004 to 1000 s (Fig. 5a,b). At some sites, particularly at the northernmost extent of the north–south profile, the data are poor in the MT dead band (typically between 0.5 and 5 s), in which the natural EM fluctuations have low intensity (example Fig. 5c). This is likely due to low signal at the time of data acquisition.

Table 1. Locations and recording times of MT stations.

Site	*Start time*	*End time*	*Duration*	*Longitude*	*Latitude*
2	20/05/2012 7:00	22/05/2012 0:04	41.1	124°17'58.98"E	17°26'27.72"S
3	20/05/2012 9:30	22/05/2012 0:36	39.1	124°23'49.08"E	17°26'26.76"S
4	21/05/2012 8:00	23/05/2012 0:09	40.2	124°29'7.62"E	17°26'31.98"S
5	21/05/2012 9:15	23/05/2012 0:41	39.4	124°34'41.1"E	17°26'10.74"S
6	21/05/2012 6:30	23/05/2012 1:14	42.7	124°40'34.14"E	17°26'2.58"S
7	24/05/2012 3:10	26/05/2012 0:55	45.8	124°43'13.56"E	17°25'0.3"S
8	23/05/2012 3:15	24/05/2012 21:03	41.8	124°45'16.62"E	17°23'34.26"S
9	23/05/2012 5:00	24/05/2012 23:35	42.6	124°50'46.74"E	17°25'14.1"S
10	23/05/2012 6:45	24/05/2012 23:11	40.4	124°56'38.82"E	17°25'21.54"S
11	22/05/2012 4:00	24/05/2012 0:50	44.8	124°59'18.78"E	17°26'11.34"S
12	22/05/2012 5:45	23/05/2012 21:28	39.7	125°01'20.46"E	17°28'44.7"S
13	22/05/2012 7:00	24/05/2012 0:06	41.1	125°02'56.34"E	17°30'41.1"S
15	18/05/2012 4:15	20/05/2012 0:51	44.6	125°07'0.9"E	17°34'19.38"S
16	18/05/2012 3:00	19/05/2012 23:59	45	125°08'54.66"E	17°36'21.18"S
18	19/05/2012 3:15	21/05/2012 0:45	45.5	125°12'52.08"E	17°40'13.74"S
20	24/05/2012 4:45	26/05/2012 1:40	44.9	124°47'38.88"E	17°21'45.54"S
21	25/05/2012 2:30	27/05/2012 1:31	47	124°50'12"E	17°19'13.26"S
22	25/05/2012 4:00	26/05/2012 19:40	39.7	124°51'22.32"E	17°17'22.98"S
23	24/05/2012 6:15	26/05/2012 2:37	44.4	124°52'19.74"E	17°15'11.7"S
24	25/05/2012 6:30	27/05/2012 2:30	44	124°54'39.24"E	17°13'11.4"S
25	26/05/2012 4:30	28/05/2012 0:18	43.8	124°55'18.3"E	17°10'53.7"S
26	26/05/2012 6:10	28/05/2012 0:41	42.5	124°58'19.08"E	17°09'4.2"S
27	26/05/2012 7:10	28/05/2012 1:05	41.9	125°00'26.58"E	17°08'50.16"S
28	02/06/2012 2:45	03/06/2012 17:45	39	125°03'20.04"E	17°08'30.66"S
29	02/06/2012 3:45	04/06/2012 6:16	50.5	125°06'15.24"E	17°07'23.34"S
30	02/06/2012 4:45	04/06/2012 6:51	50.1	125°09'33.84"E	17°06'58.86"S
31	04/06/2012 8:30	06/06/2012 0:35	40.1	125°11'50.04"E	17°07'3.12"S
32	04/06/2012 9:30	06/06/2012 1:05	39.6	125°14'17.46"E	17°08'38.1"S
33	31/05/2012 6:30	02/06/2012 0:11	41.7	125°05'58.5"E	17°00'26.16"S
34	31/05/2012 7:30	02/06/2012 0:34	41.1	125°08'11.64"E	17°02'33.3"S
35	31/05/2012 9:00	02/06/2012 0:54	39.9	125°10'46.98"E	17°03'56.1"S
36	03/06/2012 5:10	05/06/2012 2:05	44.9	125°15'21.42"E	17°11'11.76"S
37	03/06/2012 4:00	05/06/2012 2:36	46.6	125°16'39.42"E	17°13'28.14"S
38	03/06/2012 2:40	04/06/2012 22:45	44.1	125°18'31.44"E	17°15'3.6"S
39	27/05/2012 7:00	29/05/2012 0:12	41.2	125°21'27.66"E	17°16'52.62"S
40	27/05/2012 8:30	29/05/2012 0:36	40.1	125°23'45.12"E	17°18'8.82"S
41	27/05/2012 9:00	28/05/2012 15:56	30.9	125°26'27.36"E	17°19'25.74"S
42	29/05/2012 6:15	31/05/2012 2:21	44.1	125°29'13.38"E	17°20'40.26"S
43	29/05/2012 4:45	30/05/2012 12:47	32	125°32'1.62"E	17°21'53.64"S
44	29/05/2012 3:20	31/05/2012 1:30	46.2	125°36'4.92"E	17°24'23.94"S
45	05/06/2012 2:00	06/06/2012 1:39	23.7	125°16'49.92"E	17°09'24.96"S
46	01/06/2012 3:20	03/06/2012 0:46	45.4	125°19'59.16"E	17°10'16.08"S
47	01/06/2012 4:30	03/06/2012 0:23	43.9	125°22'4.92"E	17°09'25.68"S
48	01/06/2012 5:45	02/06/2012 19:15	37.5	125°25'13.56"E	17°09'16.2"S
49	28/05/2012 4:10	29/05/2012 23:41	43.5	125°28'21.24"E	17°09'1.44"S
50	28/05/2012 5:30	29/05/2012 3:14	21.7	125°30'45.78"E	17°08'22.2"S
51	28/05/2012 7:30	30/05/2012 0:53	41.4	125°32'24.06"E	17°06'33.24"S
52	30/05/2012 3:00	01/06/2012 1:02	46	125°34'24.78"E	17°04'36.18"S
53	30/05/2012 4:40	01/06/2012 0:36	43.9	125°36'21.48"E	17°03'0.3"S
54	30/05/2012 5:30	01/06/2012 0:11	42.7	125°39'1.86"E	17°01'17.1"S
55	08/06/2012 6:00	10/06/2012 0:41	42.7	125°40'38.58"E	17°03'31.44"S
56	08/06/2012 8:00	10/06/2012 1:15	41.3	125°43'37.26"E	17°04'10.02"S

Table 1. continued

Site	Start time	End time	Duration	Longitude	Latitude
57	07/06/2012 7:00	09/06/2012 1:54	42.9	125°46'1.8"E	17°04'34.56"S
58	07/06/2012 6:00	09/06/2012 2:18	44.3	125°48'59.88"E	17°05'25.5"S
59	07/06/2012 4:00	09/06/2012 2:44	46.7	125°51'22.8"E	17°07'5.22"S
60	06/06/2012 9:00	08/06/2012 1:28	40.5	125°31'45.96"E	16°51'44.76"S
62	06/06/2012 6:00	08/06/2012 0:32	42.5	125°35'21.84"E	16°55'12.78"S
63	08/06/2012 3:55	09/06/2012 19:45	39.8	125°37'33.12"E	16°58'4.32"S
64	05/06/2012 10:00	07/06/2012 0:21	38.4	125°39'32.4"E	16°58'43.56"S
65	05/06/2012 9:00	07/06/2012 0:27	39.5	125°40'41.7"E	16°56'7.62"S
66	05/06/2012 7:00	06/06/2012 22:52	39.9	125°43'40.92"E	16°54'58.86"S
67	09/06/2012 5:30	11/06/2012 1:17	43.8	125°46'38.76"E	16°54'19.08"S
68	09/06/2012 7:00	11/06/2012 0:36	41.6	125°49'32.04"E	16°52'10.56"S
69	09/06/2012 8:30	10/06/2012 23:55	39.4	125°50'56.88"E	16°46'46.08"S
70	10/06/2012 5:30	11/06/2012 18:43	37.2	125°56'20.04"E	16°42'20.76"S
71	28/06/2012 6:50	30/06/2012 0:52	42	126°03'39.72"E	16°35'7.5"S
72	28/06/2012 9:10	30/06/2012 6:00	44.8	126°15'0.12"E	16°32'23.52"S
73	12/06/2012 3:50	14/06/2012 0:13	44.4	126°24'39.24"E	16°27'22.02"S
73H	04/07/2012 5:15	06/07/2012 1:53	44.6	126°30'5.88"E	16°22'42.6"S
74	11/06/2012 5:30	13/06/2012 2:01	44.5	126°30'0.78"E	16°17'57.78"S
74H	04/07/2012 6:30	05/07/2012 23:52	41.4	126°28'46.74"E	16°12'35.88"S
75	12/06/2012 6:30	14/06/2012 3:11	44.7	126°30'55.92"E	16°07'22.98"S
76	11/06/2012 7:30	12/06/2012 14:51	31.4	126°26'49.08"E	16°00'48.9"S
77	11/06/2012 8:45	12/06/2012 4:08	19.4	126°21'43.8"E	15°58'17.16"S
78	13/06/2012 6:00	15/06/2012 0:15	42.2	126°20'34.92"E	15°55'46.2"S
79	14/06/2012 2:00	16/06/2012 0:03	46.1	126°21'24.78"E	15°53'11.1"S
80	14/06/2012 5:45	15/06/2012 20:38	38.9	126°21'49.5"E	15°50'27"S
81	14/06/2012 6:50	15/06/2012 14:32	31.7	126°21'33.78"E	15°47'11.94"S
82	17/06/2012 1:00	18/06/2012 23:49	46.8	126°22'52.98"E	15°44'45.54"S
83	15/06/2012 8:30	17/06/2012 0:36	40.1	126°23'12"E	15°42'2.4"S
84	15/06/2012 5:30	16/06/2012 3:44	22.2	126°21'47.7"E	15°40'0.72"S
85	16/06/2012 2:40	18/06/2012 0:16	45.6	126°22'11.4"E	15°37'12"S
86	16/06/2012 4:00	18/06/2012 0:54	44.9	126°19'59.4"E	15°32'16.32"S
87	13/06/2012 9:00	15/06/2012 5:37	44.6	126°18'26.46"E	15°30'7.32"S
88	16/06/2012 5:10	18/06/2012 1:25	44.3	126°18'24.12"E	15°27'25.02"S
89	17/06/2012 3:35	18/06/2012 16:28	36.9	126°18'3.78"E	15°24'44.76"S
90	17/06/2012 4:30	18/06/2012 13:41	33.2	126°16'10.68"E	15°22'51.18"S
91	18/06/2012 3:30	20/06/2012 1:47	46.3	126°13'24.66"E	15°22'34.02"S
92	19/06/2012 7:40	21/06/2012 0:46	41.1	126°12'21.72"E	15°19'50.64"S
93	18/06/2012 4:15	20/06/2012 2:31	46.3	126°11'44.1"E	15°17'20.46"S
94	19/06/2012 6:15	21/06/2012 1:33	43.3	126°12'20.22"E	15°11'53.58"S
95	19/06/2012 5:00	21/06/2012 2:09	45.2	126°12'42.54"E	15°06'24.3"S
96	20/06/2012 4:15	22/06/2012 1:15	45	126°12'20.52"E	15°00'58.5"S
97	18/06/2012 6:40	20/06/2012 4:17	45.6	126°14'1.02"E	14°55'50.28"S
98	20/06/2012 8:30	22/06/2012 0:55	40.4	126°11'26.28"E	14°53'3.6"S
99	21/06/2012 2:50	23/06/2012 2:49	48	126°02'25.26"E	14°56'24.42"S
100	21/06/2012 5:45	23/06/2012 3:26	45.7	126°00'1.62"E	14°55'9.12"S
101	21/06/2012 7:10	22/06/2012 18:04	34.9	125°57'22.68"E	14°55'53.34"S
102	21/06/2012 9:00	23/06/2012 1:26	40.4	125°55'15.72"E	14°54'0.9"S
103	23/06/2012 3:00	25/06/2012 0:20	45.3	125°54'39.9"E	14°51'20.4"S
104	23/06/2012 4:00	24/06/2012 23:49	43.8	125°52'21.18"E	14°50'8.7"S
105	23/06/2012 5:50	24/06/2012 23:36	41.8	125°50'16.92"E	14°48'13.98"S
106	22/06/2012 7:20	24/06/2012 1:20	42	125°48'20.52"E	14°46'25.2"S
107	22/06/2012 6:30	24/06/2012 0:46	42.3	125°47'1.92"E	14°43'52.38"S

Table 1. continued

Site	*Start time*	*End time*	*Duration*	*Longitude*	*Latitude*
108	30/06/2012 8:50	02/07/2012 2:50	42	126°43'39.12"E	16°02'1.74"S
109	01/07/2012 2:45	03/07/2012 3:13	48.5	126°55'13.98"E	15°57'35.82"S
110	26/06/2012 8:45	28/06/2012 7:12	46.5	127°06'13.38"E	16°00'0.36"S
111	26/06/2012 7:10	28/06/2012 21:59	62.8	127°15'51.6"E	15°54'24.96"S
112	26/06/2012 5:40	28/06/2012 21:59	64.3	127°26'22.14"E	15°50'34.62"S
113	02/07/2012 8:45	03/07/2012 9:39	24.9	127°36'42.54"E	15°46'51"S
114	01/07/2012 5:45	03/07/2012 0:53	43.1	127°42'16.26"E	15°45'52.26"S
115	03/07/2012 3:05	05/07/2012 0:30	45.4	127°48'3.84"E	15°46'10.02"S
116	01/07/2012 8:45	03/07/2012 3:20	42.6	127°53'13.56"E	15°48'1.62"S
117	03/07/2012 5:30	04/07/2012 21:02	39.5	127°55'14.22"E	15°50'14.7"S
118	03/07/2012 7:15	03/07/2012 22:11	14.9	127°57'59.1"E	15°52'9.6"S
119	06/07/2012 2:15	08/07/2012 0:35	46.3	127°59'52.98"E	15°53'55.2"S
120	03/07/2012 8:40	05/07/2012 0:27	39.8	128°02'22.26"E	15°55'11.16"S
121	06/07/2012 7:25	06/07/2012 22:21	14.9	128°03'46.08"E	15°54'47.04"S
122	06/07/2012 8:00	06/07/2012 20:36	12.6	128°06'24.12"E	15°55'17.46"S
123	05/07/2012 4:00	07/07/2012 1:15	45.3	128°09'4.2"E	15°55'8.88"S
124	05/07/2012 5:55	07/07/2012 1:33	43.6	128°11'50.58"E	15°54'2.7"S
125	05/07/2012 7:00	07/07/2012 2:02	43	128°14'14.28"E	15°52'34.86"S
126	08/07/2012 3:30	10/07/2012 0:25	44.9	128°16'53.94"E	15°51'29.64"S
127	08/07/2012 6:15	10/07/2012 1:35	43.3	128°19'48.54"E	15°51'17.4"S
128	15/07/2012 6:20	16/07/2012 21:48	39.5	128°12'25.8"E	15°32'47.46"S
129	15/07/2012 4:40	17/07/2012 0:28	43.8	128°13'52.68"E	15°36'15.84"S
130	13/07/2012 1:40	13/07/2012 22:52	21.2	128°14'25.8"E	15°38'35.76"S
131	13/07/2012 2:30	15/07/2012 1:53	47.4	128°15'32.46"E	15°41'40.98"S
132	15/07/2012 2:00	17/07/2012 1:03	47.1	128°16'2.88"E	15°44'16.32"S
133	17/07/2012 3:00	19/07/2012 2:54	47.9	128°17'39.66"E	15°46'11.46"S
134	08/07/2012 5:00	10/07/2012 1:03	44.1	128°18'28.74"E	15°48'48.78"S
135	07/07/2012 4:05	09/07/2012 0:35	44.5	128°22'31.26"E	15°52'10.62"S
136	17/07/2012 5:30	18/07/2012 18:31	37	128°22'54.48"E	15°55'3.42"S
138	17/07/2012 4:10	19/07/2012 0:23	44.2	128°24'58.14"E	15°59'6.3"S
139	16/07/2012 3:15	17/07/2012 23:45	44.5	128°24'49.44"E	16°02'20.1"S
141	16/07/2012 4:40	17/07/2012 19:45	39.1	128°22'24.12"E	16°12'14.76"S
142	18/07/2012 3:10	19/07/2012 21:23	42.2	128°24'56.52"E	15°51'3.24"S
143	11/07/2012 1:30	13/07/2012 2:51	49.4	128°27'27.96"E	15°50'8.34"S
144	09/07/2012 5:00	10/07/2012 3:43	22.7	128°29'46.8"E	15°48'40.44"S
145	09/07/2012 5:15	09/07/2012 23:40	18.4	128°32'17.58"E	15°47'23.34"S
146	18/07/2012 5:00	20/07/2012 1:52	44.9	128°34'59.7"E	15°46'18.18"S
147	11/07/2012 4:40	12/07/2012 23:19	42.7	128°37'53.58"E	15°46'15.78"S
148	11/07/2012 7:55	12/07/2012 11:23	27.5	128°41'58.44"E	15°48'42.78"S
149	13/07/2012 7:00	14/07/2012 23:33	40.6	128°24'3.84"E	16°04'14.04"S
150	07/07/2012 8:00	09/07/2012 2:45	42.8	128°48'29.82"E	15°49'14.4"S
151	14/07/2012 5:50	16/07/2012 0:18	42.5	128°51'13.44"E	15°49'45.12"S
152	14/07/2012 4:30	15/07/2012 23:22	42.9	128°53'46.44"E	15°50'37.08"S
153	14/07/2012 3:20	15/07/2012 23:23	44.1	128°55'39.54"E	15°52'30.48"S
154	10/07/2012 5:20	11/07/2012 17:05	35.8	128°56'44.58"E	15°55'10.98"S
155	10/07/2012 6:45	11/07/2012 23:49	41.1	128°57'41.64"E	15°57'28.08"S
156	10/07/2012 8:20	12/07/2012 0:13	39.9	128°59'31.2"E	15°59'9.24"S
157	12/07/2012 1:55	14/07/2012 1:25	47.5	129°03'13.02"E	16°00'26.16"S
158	12/07/2012 3:15	14/07/2012 0:45	45.5	129°06'6.96"E	16°03'32.4"S
159	12/07/2012 5:20	14/07/2012 0:13	42.9	129°11'51"E	16°03'49.62"S
160	16/07/2012 6:10	18/07/2012 0:46	42.6	128°23'7.92"E	16°09'30.78"S

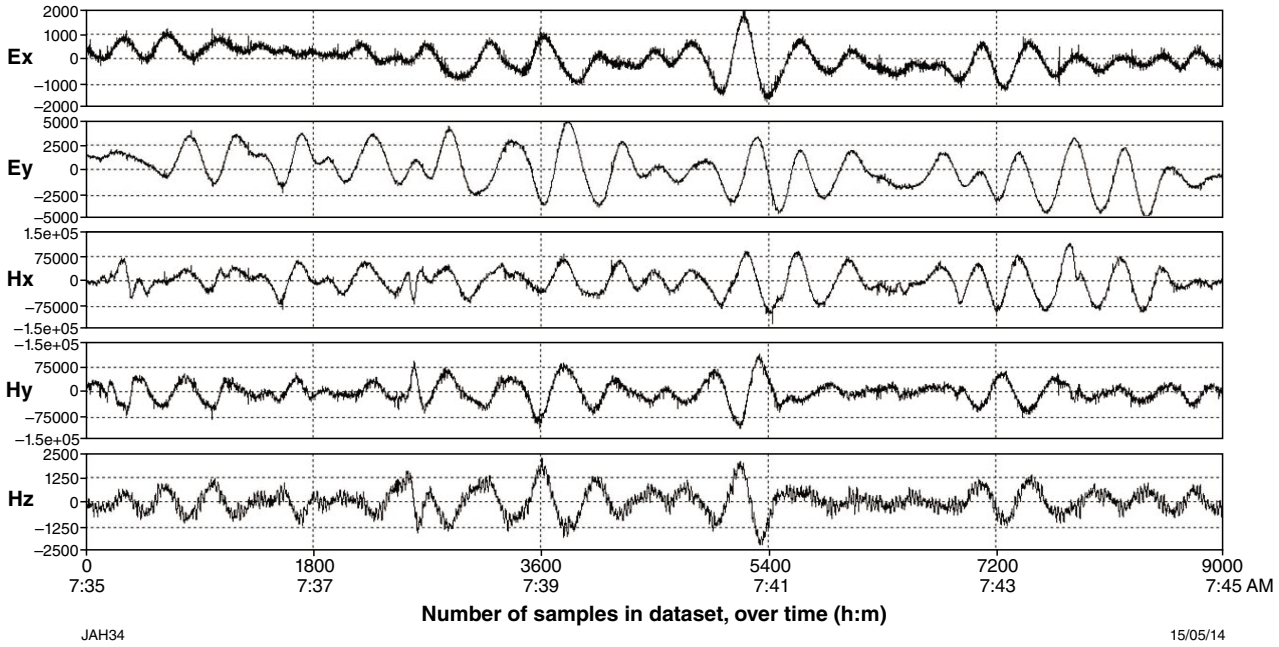

Figure 8. Example of the two electric (Ex and Ey) and three magnetic (Hx, Hy, and Hz) fields measured as a function of time at station 135

In some cases, primarily observed in the easternmost sites, the data recorded in the YX direction are out of phase (greater than 90°) at periods greater than 100 s, an indication of current channelling or distortion at depth (example Fig. 5d). The Appendix shows the response curves for each site acquired. In all cases, where the data show a high degree of scatter with large error bars or where the phases are out of quadrant (either below 0° or above 90°), these data have been removed prior to initiated 2D model inversion.

Static corrections

MT data are prone to static shifts due to heterogeneous electrical properties in the near surface at a scale smaller than the resolving capability of the MT data. The result is a frequency-independent shift of the apparent resistivity data parallel to the apparent resistivity axis, i.e. the entire curve is involved. The amount of shift is called the static shift factor(s). Static shift effects typically result in lowering the apparent resistivity curve of one or both modes. Failure to account for this will lead to incorrect estimation of resistivities and the depths at which they occur during data modelling.

Where the apparent resistivity curve of one mode was much higher than another, the lower curve was raised to match that of the other curve at the highest frequency. This helps to reduce the effect of anisotropic shift, but does not account for the static shift cases where both curves are affected.

Time-domain electromagnetic (TEM) soundings have been collected at each MT site and are not affected by these small-scale heterogeneities. The aim of this procedure is to model the near-surface electrical resistivity assuming a 1D Earth. Forward MT data is then calculated from the resulting model. The real MT data can then be matched to the forward data where the two curves overlap and further correct for the static shift effect. In theory, this is a simple procedure but in electrically resistive areas, it is often quite difficult to collect high-quality data. Unfortunately, approximately 85% of the TEM collected in this survey was not useable due to the high electrical resistivity of the near surface and the resulting low-quality data that was collected. Figure 9 shows examples of TEM curves, 1D models and curve matching from sites KIM02 and KIM90. Site KIM02 is located in a basin setting with relatively conductive rocks and shows a good-quality TEM decay and curve that overlaps well with the MT sounding. Site KIM90, on the other hand, is located on more resistive rock and the resulting TEM decays and curves do not overlap so well. In most cases, it was not possible to produce forward MT from the TEM data that would overlap sufficiently to contribute to correction of static shift.

Penetration estimates

The depth of penetration, or skin depth, is defined by the solution to the wave equation for a plane wave propagating through a homogeneous half-space and is the point at which the amplitude of the fields reduces to a factor of 1/e of that at the surface (Cagniard, 1953). Over a large region, where the 2D conductivity structure is variable, electromagnetic fields at any particular period often have vastly different penetration depths from one site to the next. Additionally, it is possible for 2D structures to exist where the depth of penetration is different for the

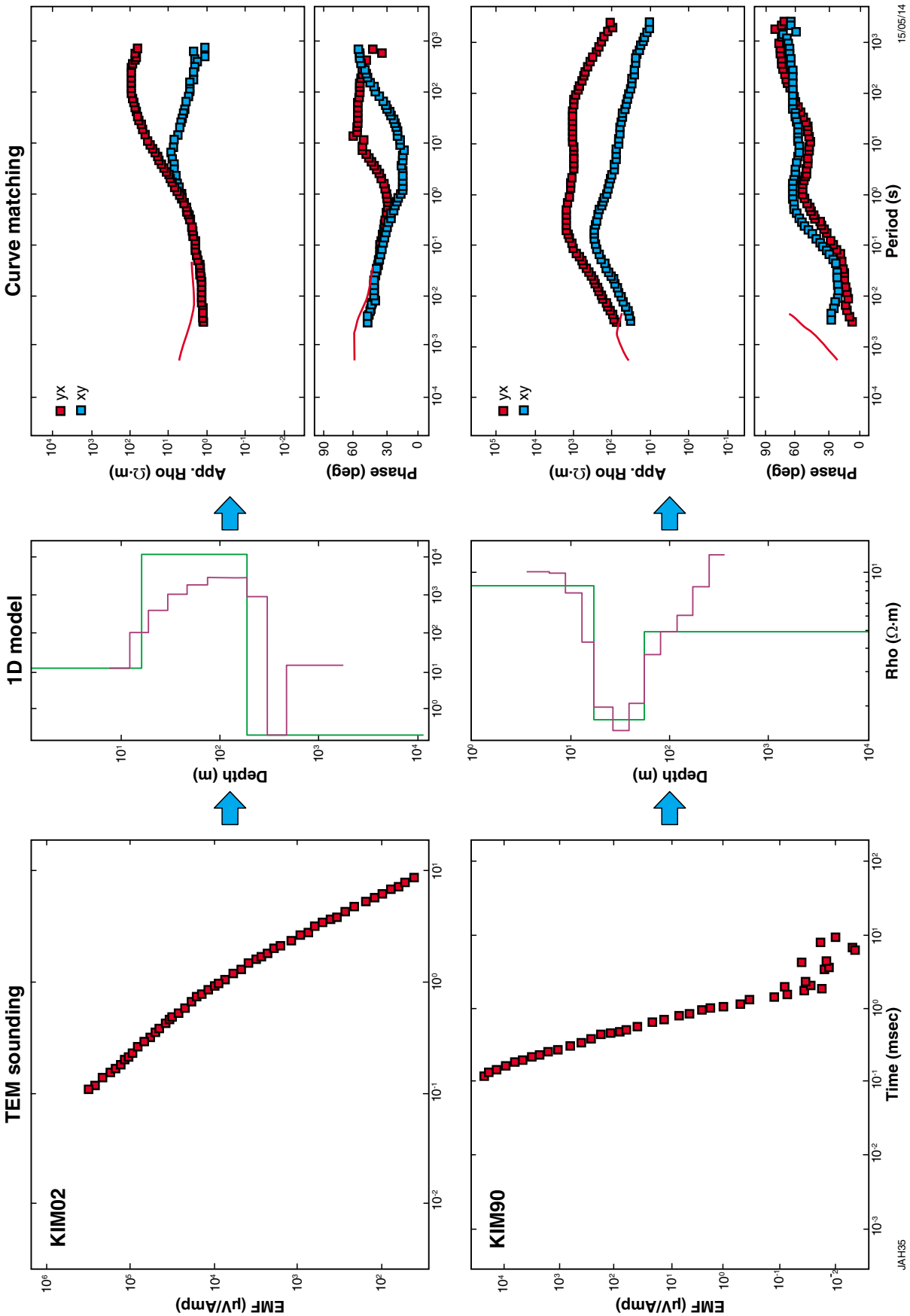

Figure 9. Examples of time-domain electromagnetic soundings, 1D models, and curve matching from sites KIM02 and KIM90

two modes of propagation (TE and TM; Jones, 2006). Penetration depths at 1000 s beneath each site have been estimated using the C-function conversion of Schmucker (1970) and the depth approximation of Niblett and Sayn-Wittgenstein (1960) and Bostick (1977) (Fig. 10). At most sites, these estimates infer sufficient penetration (>250 km) in at least one direction along each of the three profiles to model lithospheric mantle features. The southwesternmost sites show limited penetration depths (<150 km), which is an indication of shallow conductivity. The easternmost sites show significant differences in the estimated penetration depths in the XY and YX directions, suggesting strong 2/3D contrast in the conductivity structure. This is consistent with sites in the area that have phases out of quadrant at longer periods (Fig. 5d).

Dimensionality and strike analysis

Most MT modelling algorithms assume that the area of interest is geoelectrically 1D or 2D. A 3D, i.e. varying in three directions, electrical structure requires greater computational power to model the data and the earth models must be comparatively simple. In a 2D modelling scenario, the direction of geoelectric strike is assumed to be consistent, i.e. there must not be any localized or off-profile geoelectrical property variations, and the strike direction must be known. Frequency dependent pseudosections, induction vectors and phase tensors have been analysed to determine the dimensionality and geoelectric strike direction of the data. Sections of the data that are 1D, independent of strike, are identified as well as sections that are influenced by 3D. The latter cannot be represented with a 2D model. Ideally, where structure is truly 2D, a model is generated along a profile at one strike angle for all periods; however, where the subsurface structure is complex and this angle varies along the profile or with depth, the data may need to be subdivided into sections and modelled separately at different strike angles. As the primary focus of this work is to study the deeper structure, where necessary, models are generated at a strike angle that corresponds to longer periods. As shown in Figure 1, the data have been divided into four main profiles (North, Central, East, and West), as well as the four shorter profiles (Cross 1, 2, 3, and 4) for strike analysis and 2D modelling, and the preferred geoelectric strike direction has been determined for each of the profiles.

Pseudosections of the phase and apparent resistivity responses for each of the sites along the four main profiles were generated for both the TE- and TM-modes for all data points not deemed to be overly noisy or where phases are out of quadrant. As apparent resistivities may be affected by static shift, the phase pseudosections are typically observed to determine areas that are 1D. The Earth can be regarded as 1D at periods where the phases in the TE- and TM-modes are similar and the 2D models will be independent of the geoelectric strike angle.

Where lateral conductivity gradients exist within the Earth, vertical magnetic fields are created (in a 1D Earth, vertical magnetic fields are minimal). Induction arrows are the vector representations of the complex ratios of the vertical to horizontal magnetic fields. Both real and imaginary induction arrows can be produced because the ratio is complex. Here the Parkinson convention has been used, where real arrows point towards regions of low resistivity, or away from regions of high resistivity. The length of an arrow indicates the magnitude of the difference in resistivity. Where the electrical structure is 2D, the real arrows will be parallel and oriented perpendicular to the geoelectric strike. Induction vectors have been plotted both in pseudosection format for each site at each period along each of the profiles and in map view for all sites at specific periods.

The dimensionality of the MT data was further assessed using the phase-tensor method of Caldwell et al. (2004). Unlike many other dimensionality estimation methods, this method analyses only the phase variations because these are unaffected by galvanic distortion associated with near-surface changes in electrical conductivity and the method does not rely upon assumptions that the regional electrical structure is 1D or 2D. Three parameters are used to characterize the phase tensor: the maximum (Φmax) and minimum (Φmin) phase values, and the skew angle (β). The angle (α) is a measure of the tensor's orientation relative to the coordinate system and the ellipticity is a measure of the ratio of the maximum and minimum phase values. The phase tensor is commonly represented as an ellipse (Fig. 11), with the long and short axes of the ellipse representing the maximum and minimum phase values respectively (the TE- and TM-modes) and the orientation (α–β) of the major axis representing the direction of maximum current flow, or geoelectric strike angle. At periods where the phase difference between the TE- and TM-modes is minimal (<10°) the data are deemed 1D, i.e. independent of geoelectric strike angle and the phase ellipse is a pseudocircle. With the influence of two-dimensionality, the ellipticity increases. Phase tensor ellipses have been plotted in pseudosections for each station along each profile, where red represents phase minimums above 45°, generally indicating a change from resistive to more conductive rocks, and blue represents phase minimums below 45°, a change from conductive to resistive units with depth.

A 3D subsurface results in a skewed ellipse with the main axis deflected by an angle β from the symmetry axis (dashed line in Fig. 11). The skew values for each site along each profile are plotted with phase tensor ellipses in pseudosection with the colour representing the skew value (β). Bright blue indicates a skew angle of below –5° and red indicates above +5°. Empirically, $-5° < \beta < 5°$ means the data should be predominantly 2D. A skew outside this range is likely affected by 3D characteristics and these data have been removed prior to generating rose plots of the 2D geoelectric strike angle.

Note there is a 90° ambiguity inherent in phase-tensor analysis. Induction vectors can be helpful in resolving this ambiguity. Alternatively, geological and geophysical information can be used to properly assign the TE- and TM-modes as current flow (TE-mode) typically runs parallel to geological features.

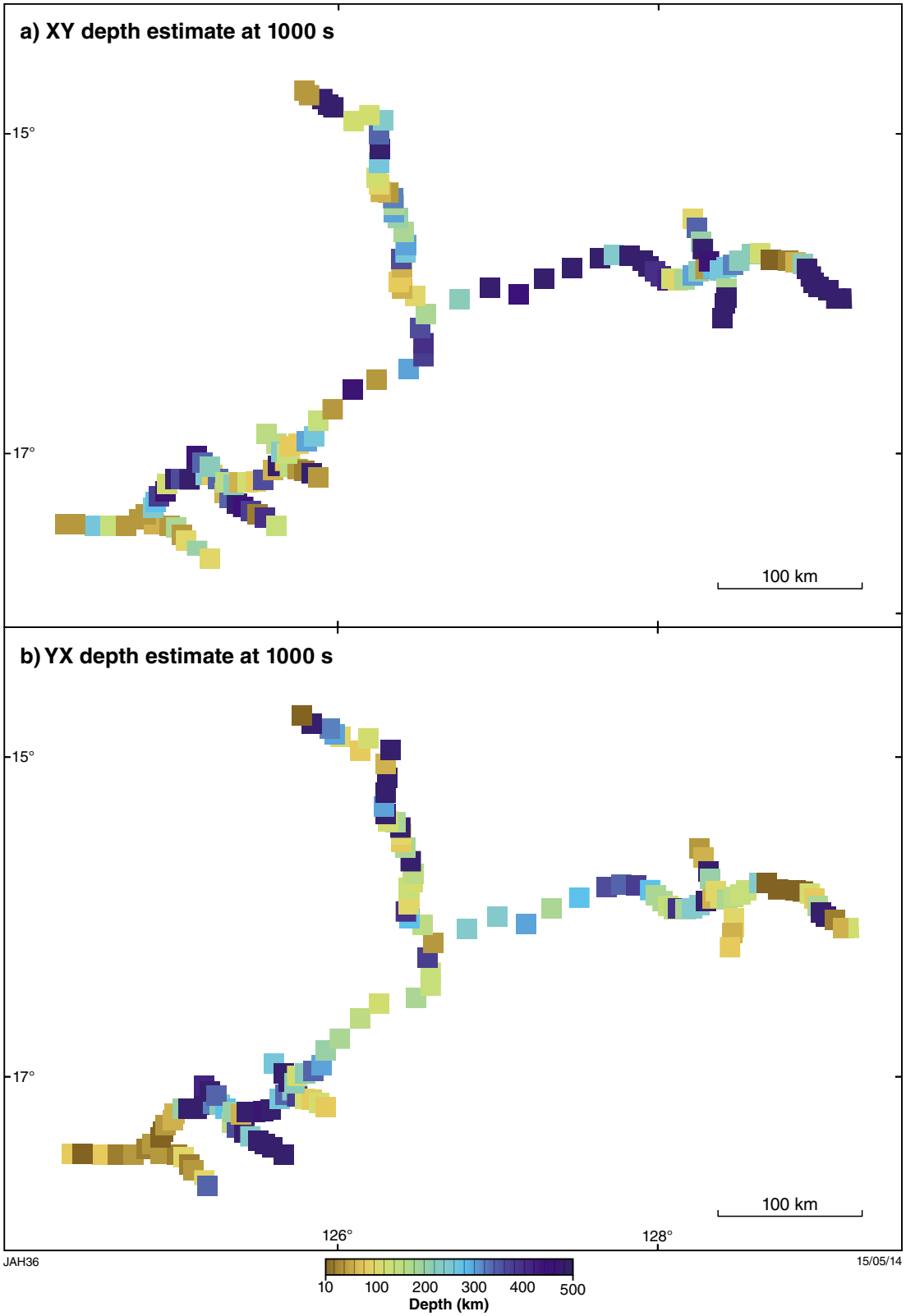

Figure 10. Estimates for maximum penetration depths at each site: a) north–south; b) east–west

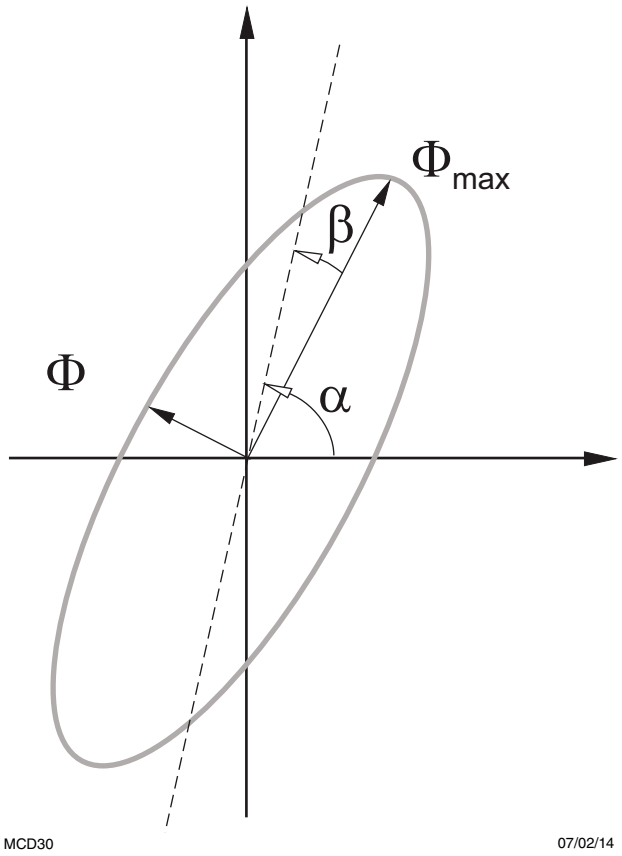

Figure 11. Graphical representation of the MT phase tensor illustrating parameters used to define the ellipse (from Caldwell et al., 2004)

Profile North

Pseudosections of the apparent resistivities and phases have been plotted along Profile North for each period of acquisition (Fig. 12). The apparent resistivity sections display prominent vertical variations or streaks. This suggests that significant static shift effects remain in the data, and 2D modelling parameters need to be set to account for these effects. The phase pseudosections reveal a layered subsurface with minimal along-profile variation, particularly at periods greater than 0.1 s. The phases of the TM- and TE-modes are similar between periods of 0.5 and 100 s, which is an indication that the data are largely 1D in this range and independent of the strike angle.

The real induction vectors along Profile North have the highest magnitude at periods below 1 s (Fig. 13). However, the directions of the induction vectors are highly variable (Fig. 14), possibly an indication of complex structures resulting from varying sedimentary layers within the Kimberley Basin or faulting within the upper crust. With the exception of the northernmost sites, short induction vectors at periods greater than 1 s are observed, consistent with the phase pseudosections that indicate a layered or 1D (or weakly 2D) Earth at depth. Although the magnitudes are small, the induction vector directions are more consistent and indicate a roughly northeast to southwest strike direction. At periods greater than about 20 s, the northernmost sites have large induction vectors pointing towards the northwest. These are likely being influenced by seawater effects, with the coastline less than 25 km from the profile.

The phase tensor ellipses along Profile North show that at periods less than about 5 s, the ellipse orientations change more rapidly and are more elongate, indicating a heterogeneous electrical structure (Fig. 15). This is consistent with varying induction vectors. At these short periods, minimum phases are below 45°, probably due to the effects of electrically conductive sedimentary units overlying a more resistive crust (Fig. 15). This suggests that the varying ellipse orientations and induction vectors may be a result of structure within the upper crust. At longer periods (>1 s; <1 Hz) responses become more consistent across the traverse, and the ellipses are more open indicating that a preferred direction of current flow is not as strong, but have a general northeast trend. This may represent data from a relatively homogeneous crystalline basement or upper mantle. At periods longer than 20 s, phase minima are above 45°, possibly a result of a change from resistive upper mantle to lower resistivities with depth.

Plots of skew along Profile North show that with the exception of short periods at isolated sites, and between periods of 10 and 80 s at the northernmost sites, the data are relatively unaffected by 3D distortion to periods to at least 70 s (Fig. 16). Pseudosections along Profile North have been generated for apparent resistivity and phases with the data estimated to have 3D effects removed (Fig. 17).

Figure 18 comprises rose diagrams plotting the strike direction calculated from the Z-strike and from the phase tensor ellipses along Profile North at six-period decade bands and showing the average value for each band. In addition to observing changes with period (depth), the profile has been divided into three sections to identify changes in the strike along the profile. There is a large degree of scatter in each of the rose plots at periods less than 1 s for each of the profile sections. This, along with the large variations in induction vectors and phase ellipses, is consistent with localized 2D or 3D structure. At periods 1 to 100 s, the average strikes show a fair degree of variability from one section to the next. As a layered, weakly 2D or 1D Earth has been predicted for these periods, a 2D model would be largely independent of the strike angle. A strike angle of 55–62° appears to satisfy most of the data at periods between 0.1 and 10 s, and 20–33° for periods greater than 100 s, however a roughly north–south (or east–west) strike is observed for the whole profile at 10 to 100 s.

2D models were generated with a strike of 57, 99 (9), and –65° (25°) to observe how variations in the preferred geoelectric strike direction influence the inversion and to determine the most accurate 2D representation of the subsurface beneath the profile. A strike direction of 57° is roughly consistent with the northeast trending structures within the crystalline basement, identified by

Gunn and Meixner (1998), and suggests that this direction corresponds to the TE-mode. Although deformation is not expected to occur as far east as Profile North, a strike of –65° is consistent with the trend of the King Leopold Orogen. As for a strike of 99 or 9°, there is no obvious geological or geophysical information at depth beneath the profile to help resolve the 90° ambiguity. Models have been generated for both scenarios, with TE running parallel and perpendicular to 99° (equivalent to a strike of 9°). It should be noted that a strike of 9° runs approximately along profile and 2D models would not resolve the subsurface structure.

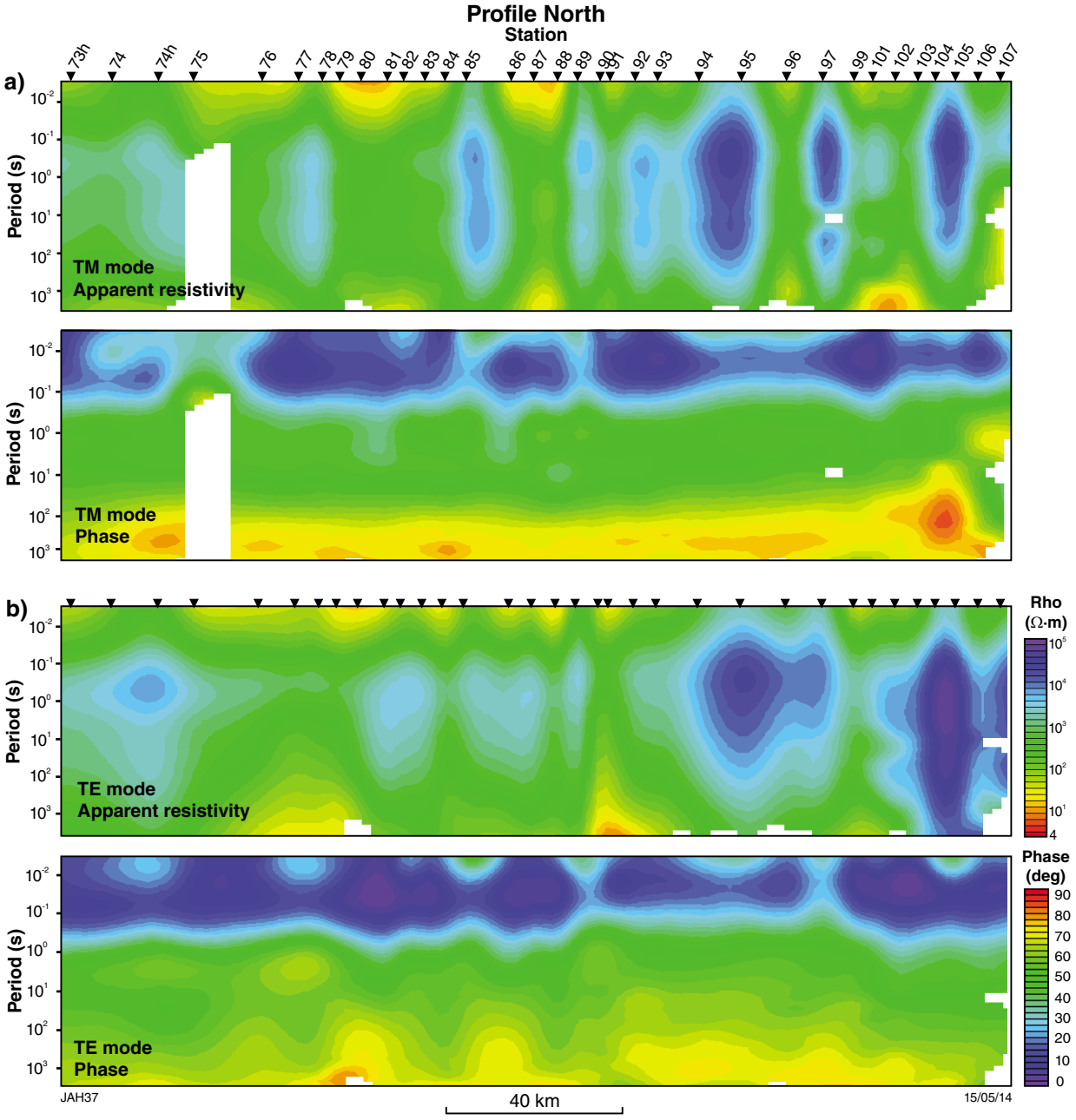

Figure 12. Pseudosections of apparent resistivity and phase along Profile North comprising data considered to have an acceptable signal to noise level for data in: a) TM-mode; b) TE-mode

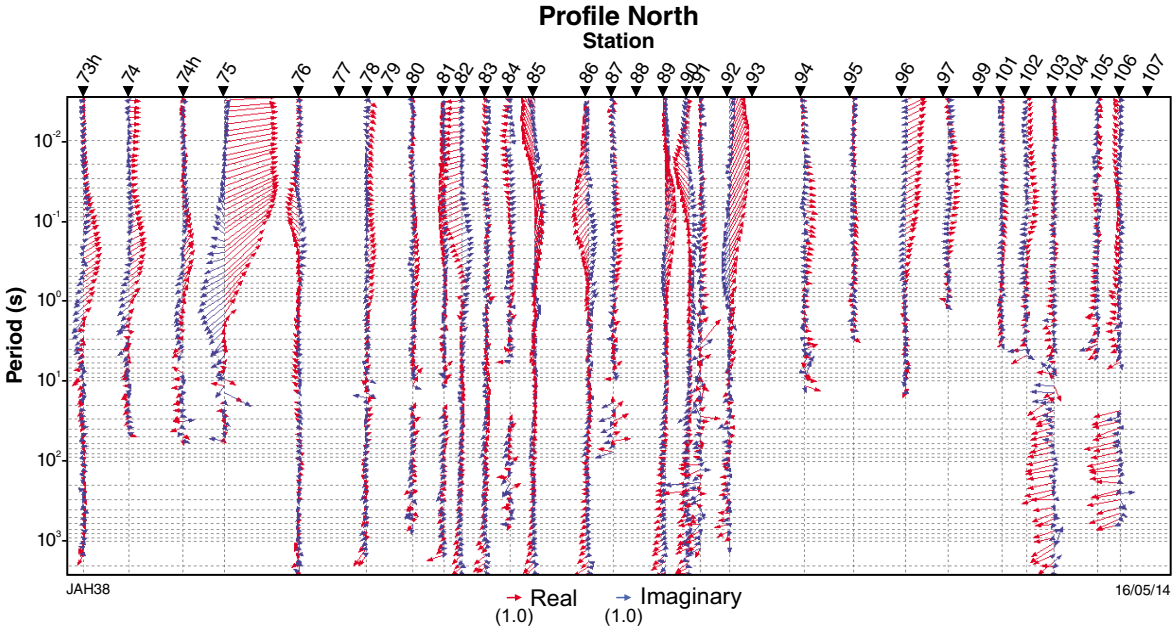

Figure 13. Pseudosection display of induction arrows at each period along Profile North

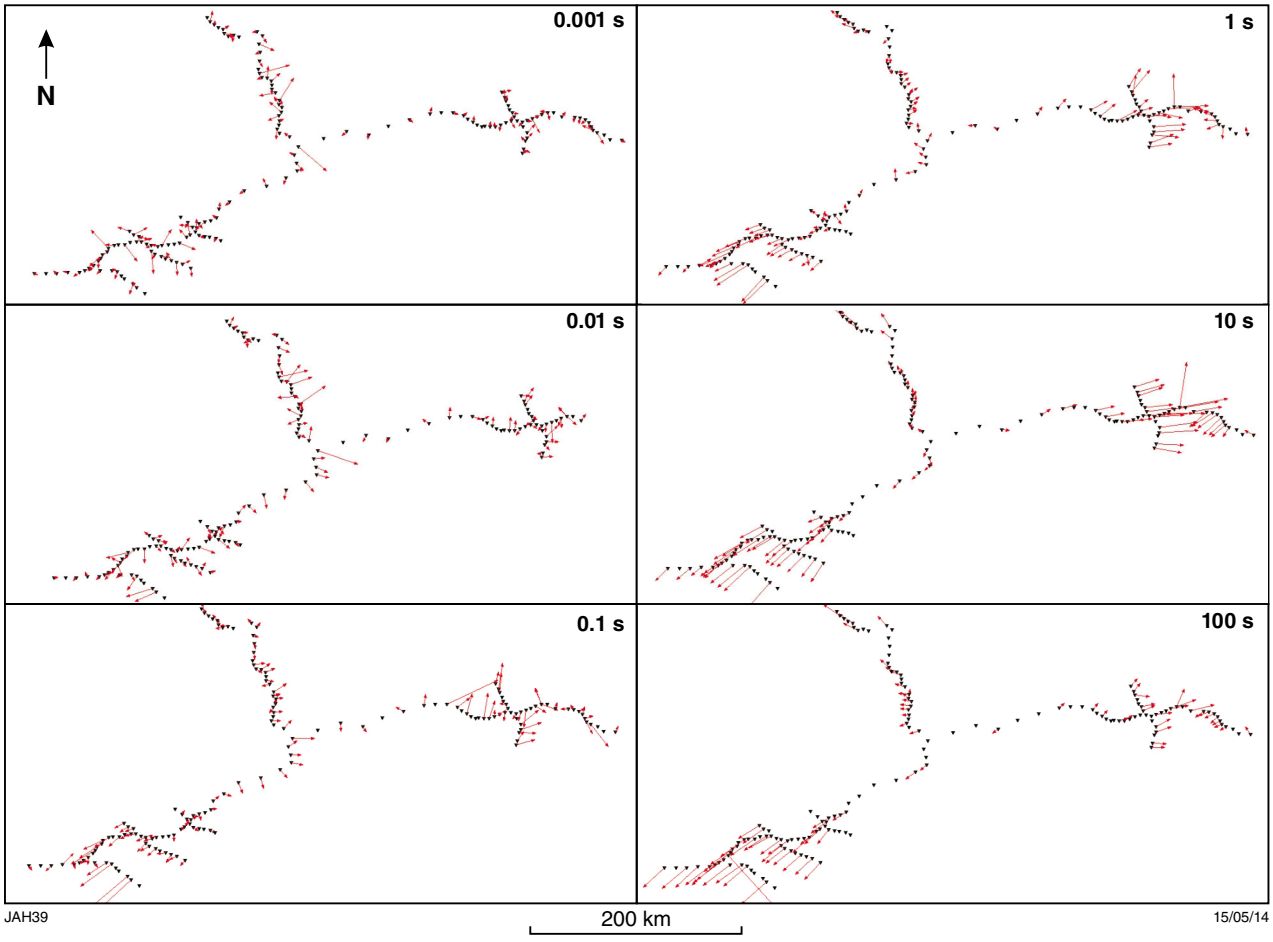

Figure 14. Map view of induction arrows at six different periods for all MT sites

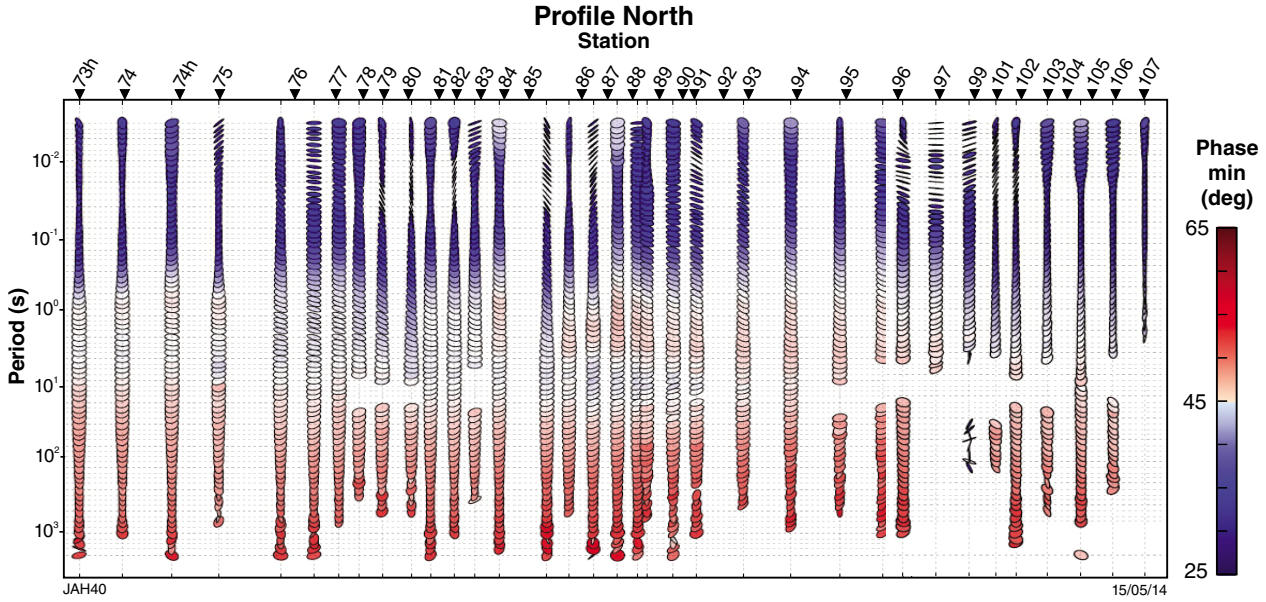

Figure 15. Pseudosection display of MT phase ellipses and phase minimums along Profile North. Blue represents phase minima below 45° and red represents phase minima above 45°.

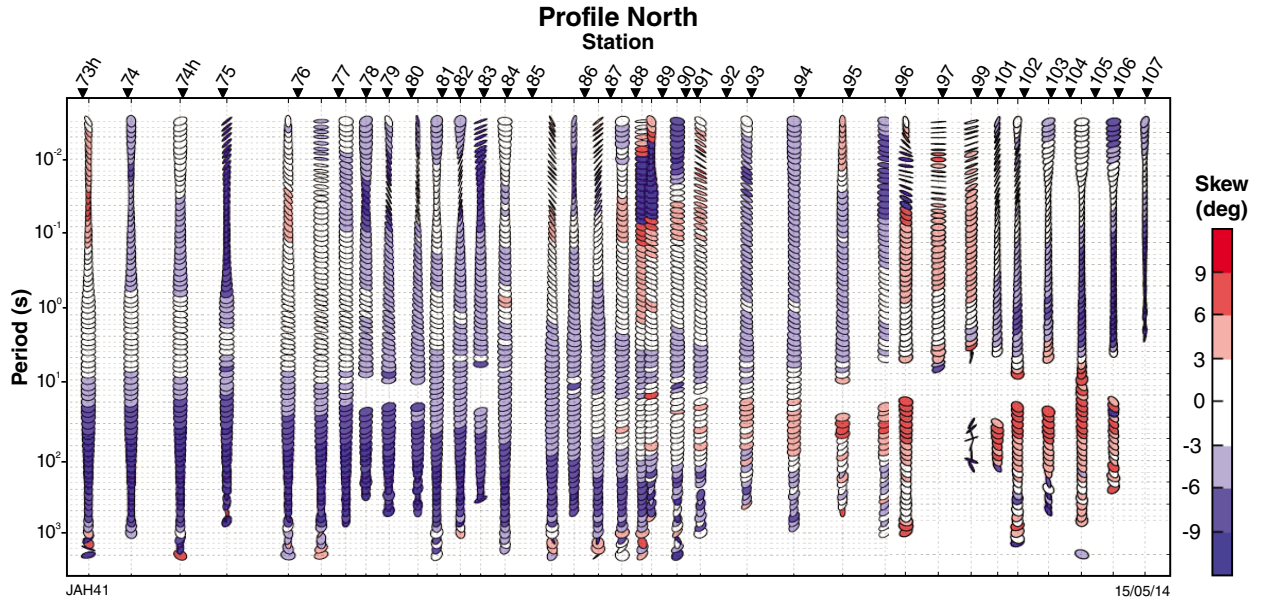

Figure 16. Pseudosection display of MT phase ellipses and skew (β) along Profile North. Dark blue represents a skew value below –5° and dark red represents skew value above +5°.

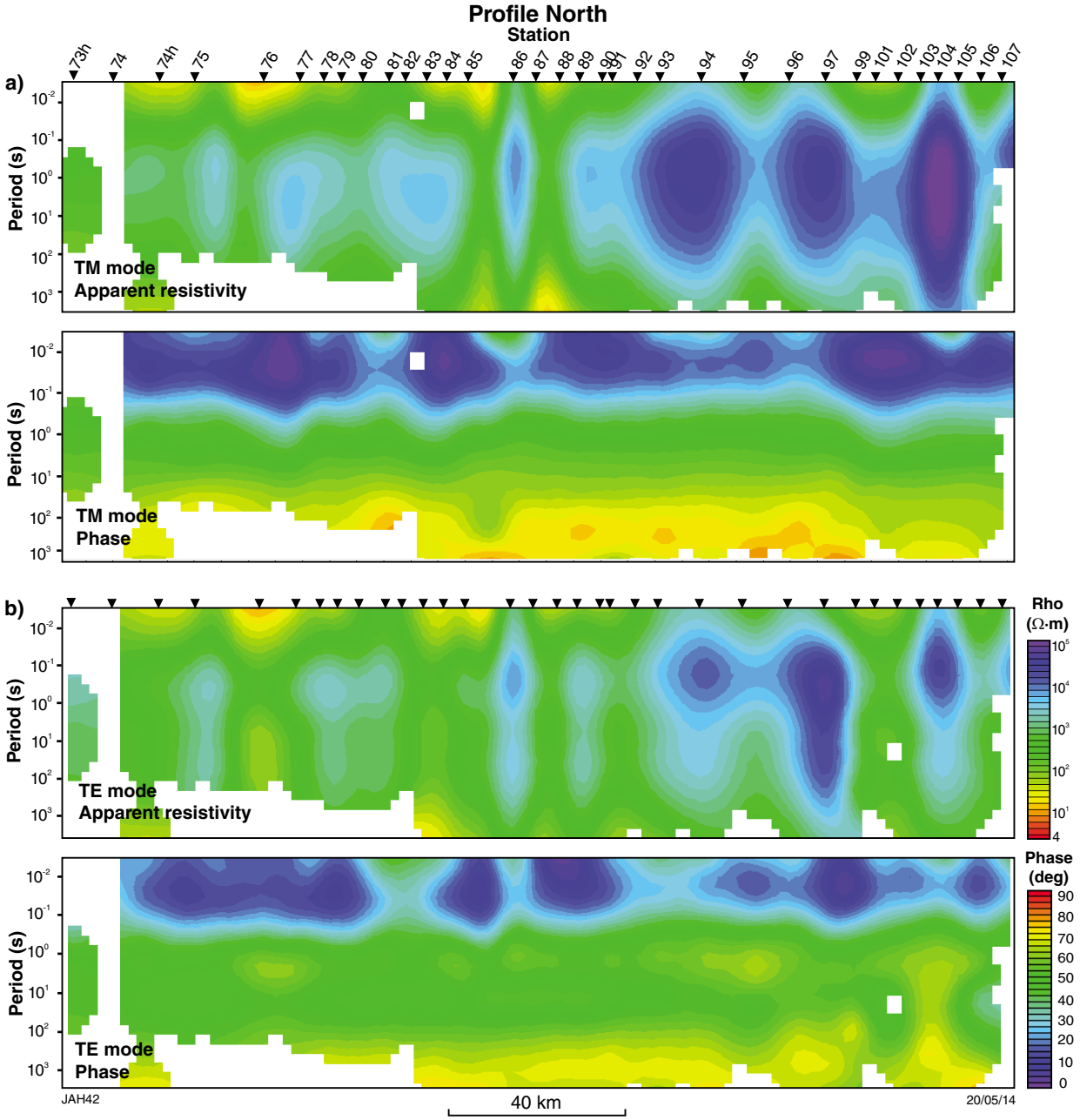

Figure 17. Pseudosections in the: a) TM-mode; b) TE-mode of apparent resistivity and phase along Profile North comprising data considered to have an acceptable signal to noise level and no significant 3D influence as defined by the skew (β); –5°<β<5°

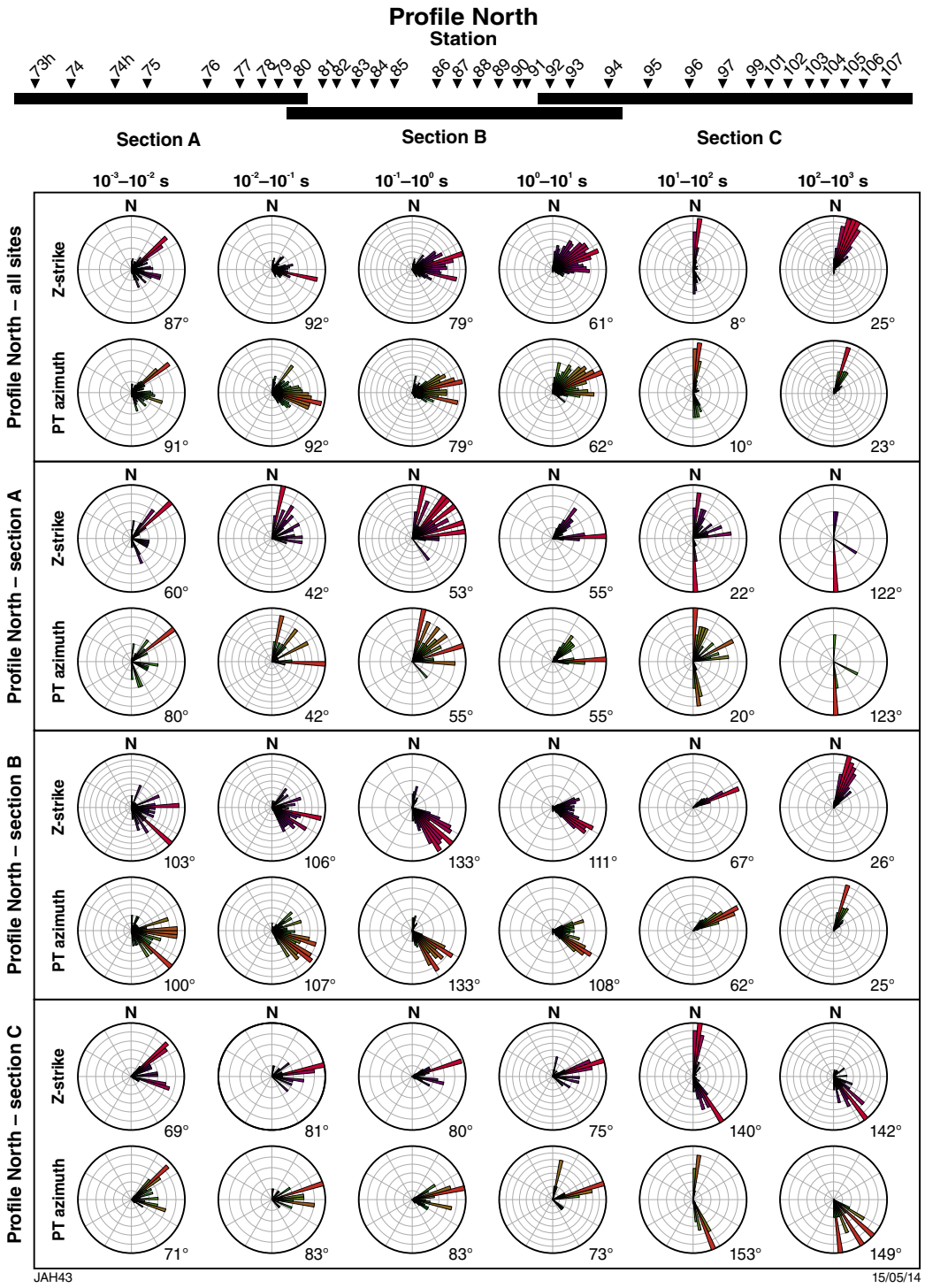

Figure 18. Rose diagrams of phase tensor ellipses and Z-strike orientations at six-decade period bands along Profile North

Profile Central

Pseudosections of phase and apparent resistivity along Profile Central are shown in Figure 19. The apparent resistivities show minor vertical streaking indicating the static shift effects are minor. The phases show a layered subsurface and the TE- and TM-modes are similar at periods up to 100 s for the eastern half of the profile, suggestive of a 1D earth. To the west, the phases show slightly more lateral variation; however, the phases between the two modes are similar to about 10 s. The largest differences in the phases are observed in the central part of the profile, beneath sites 73–108, which is an indication of two- or three-dimensionality.

Consistent with the observations of phase pseudosections, with the exception of a few sites in the central part of the profile, the real induction vectors are small at periods up to at least 10 s (Fig. 20). Induction vectors at the central sites, at periods between 0.01 and 1 s, point roughly westward, suggestive of a north–south geoelectric strike direction (Fig. 14). At periods greater than 10 s, the sites farthest to the west show westward-pointing induction vectors, and the sites to the east, eastward-pointing vectors, again suggestive of a north–south geoelectric strike direction.

Pseudosections of the phase ellipses for each site at each period along Profile Central are shown in Figure 21. The westernmost section of the profile shows open ellipses

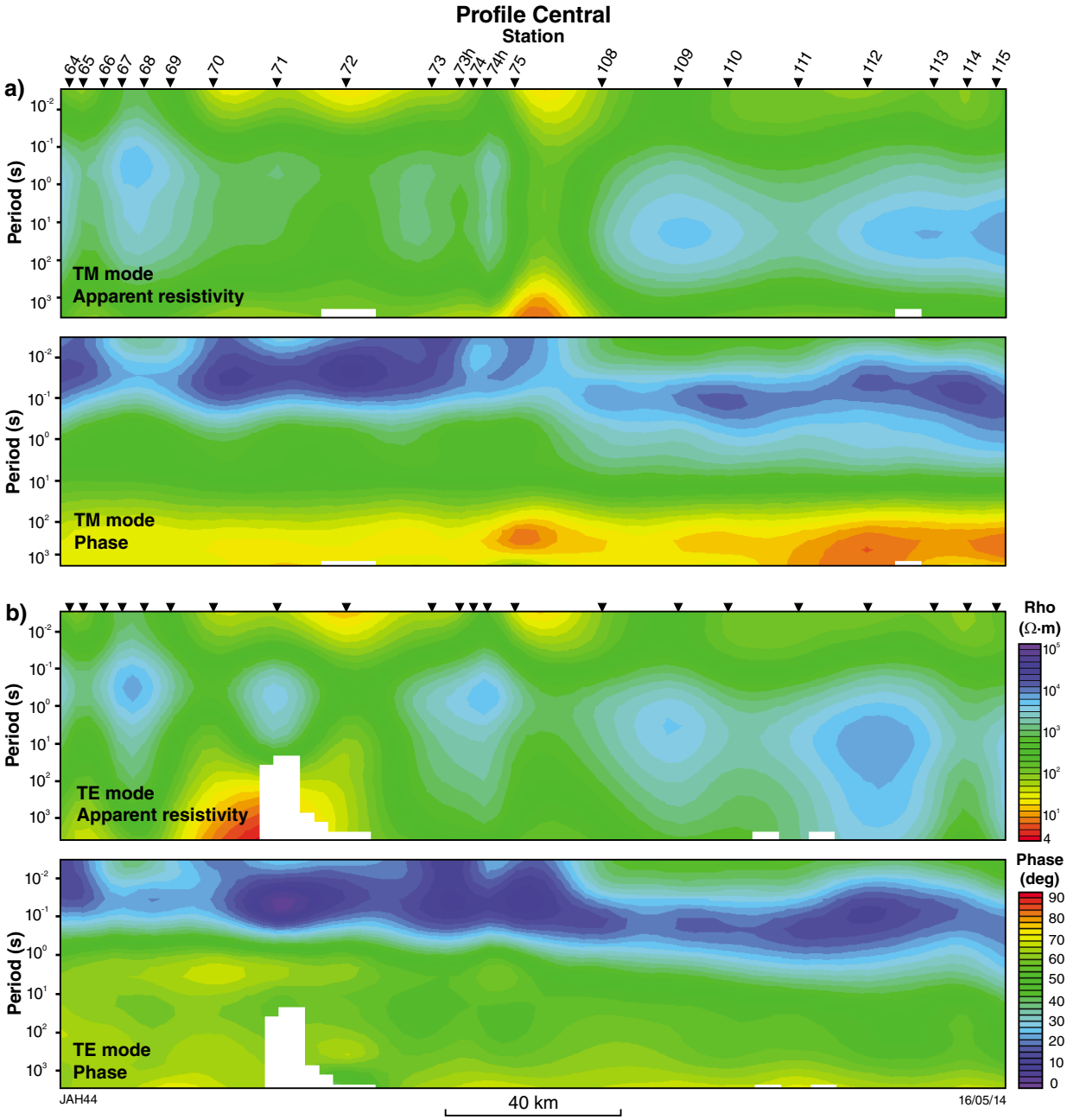

Figure 19. Pseudosections of apparent resistivity and phase along Profile Central comprising data considered to have an acceptable signal to noise level for data in: a) TM-mode; b) TE-mode

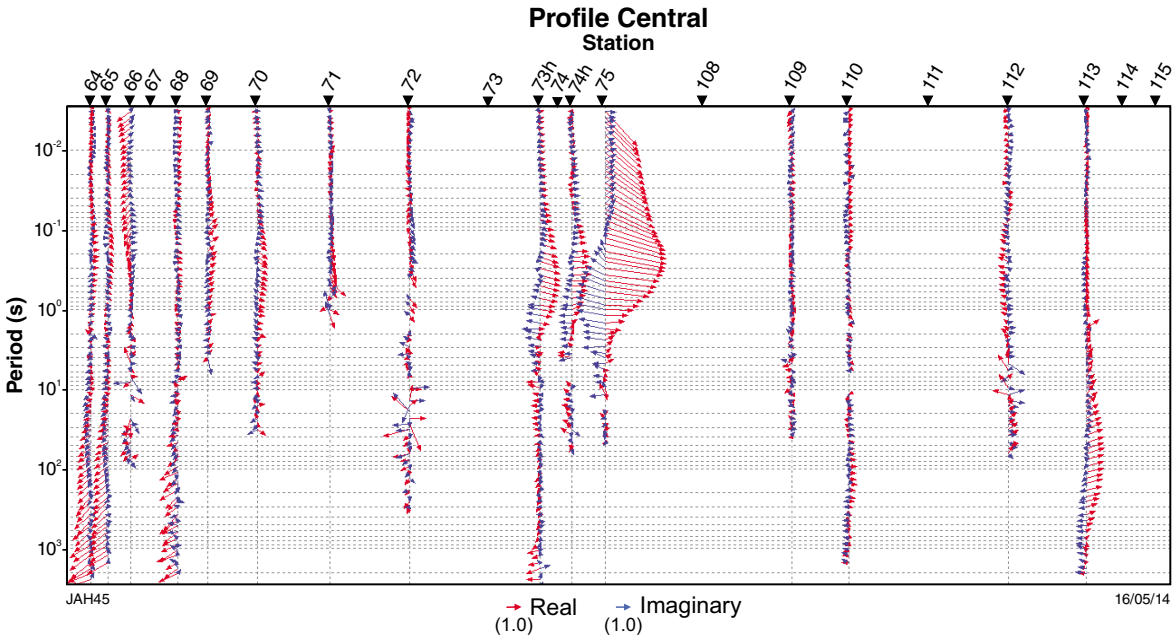

Figure 20. Pseudosection display of induction arrows at each period along Profile Central

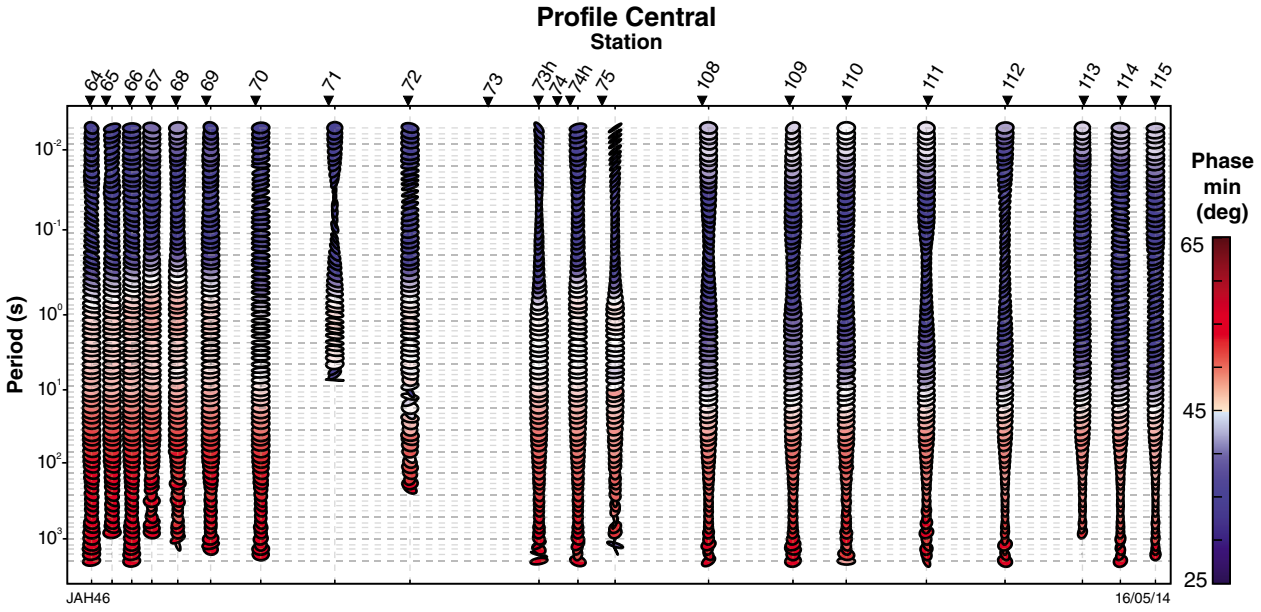

Figure 21. Pseudosection display of MT phase ellipses and phase minimums along Profile Central. Blue represents phase minimums below 45° and red represents phase minimums above 45°.

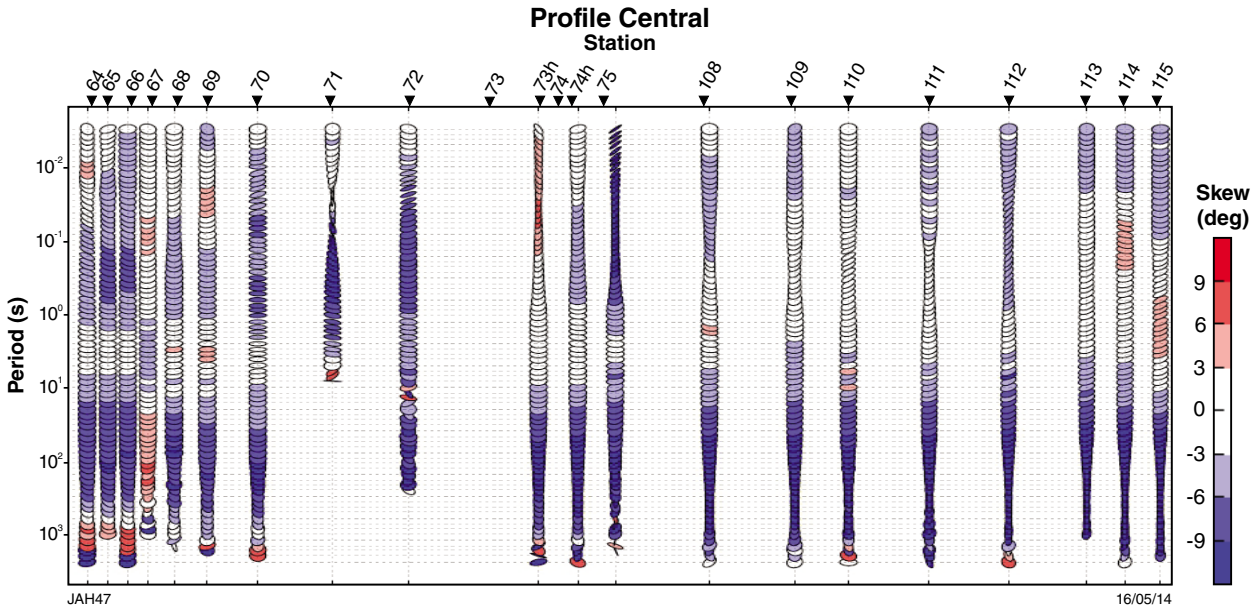

Figure 22. Pseudosection display of MT phase ellipses and skew (β) along Profile Central. Dark blue represents skew values below –5° and dark red represents skew values above +5°.

at most sites over the whole period range. The central section of the profile shows elongate ellipses with variable trends at periods <0.5 s, and the phase ellipses for the westernmost sites are predominantly open over most of the period range with slightly more elongate ellipses, trending northeast at periods between 0.1 and 0.7 s and trending north–south at periods >250 s. Phases are low at periods below about 0.5 s for the western half of the profile, but to about 10 s for the eastern half (Fig. 21). The low phases at higher periods to the east may represent a thicker resistive crust; however, as minimum phases are about 45° to 0.01 s in the west, it is more likely a result of thicker conductive sedimentary rocks near the surface.

Plots of skew values along Central Profile show that the data are relatively unaffected by 3D distortions at periods below 80 s (Fig. 22). Pseudosections along Profile Central have been generated for apparent resistive and phases with the data estimated to have 3D effects removed (Fig. 23).

Results of rose diagrams generated along Profile Central for data in six-period bands along the whole profile and for three separate sections of the line (Fig. 24) show a large spread in strike angles at periods above 0.1 s. Where there is little scatter, an indication of a strong preference for a particular angle, a strike angle between 85 and 91° is apparent at periods between 0.1 and 100 s for the whole profile and section A and at periods of 1 to 100 s for section B. For section B, at shorter periods where the phase ellipses have been shown to be most elongate, average strike values range between 39 and 47°. Section C shows a preference of 53–65° over most of the period range, consistent with results observed along the East profile (described below). At periods above 100 s, there is little data due to the removal of points affected by 3D distortions; however, the strike consistently shows averages of 8–13° with the exception of section A, satisfied with a strike of about 51°.

Modelling has been undertaken along the whole length of Profile Central with data rotated to a strike angle of 0, 45, and –45°. For a strike of 0°, the TE-mode was assigned north–south based on induction vectors. As there is little information available to resolve the inherent 90° strike ambiguity at 45°, models were generated with TE-mode assigned to both 45 and –45°. Note that a strike angle of 45° is roughly parallel to the profile direction and 2D structure may not be accurately resolved. The easternmost segment of the profile (section C) has been modelled independently at a strike angle of 62°. This modelling also uses data assigned to Profile East and is referred to here as Profile C-E.

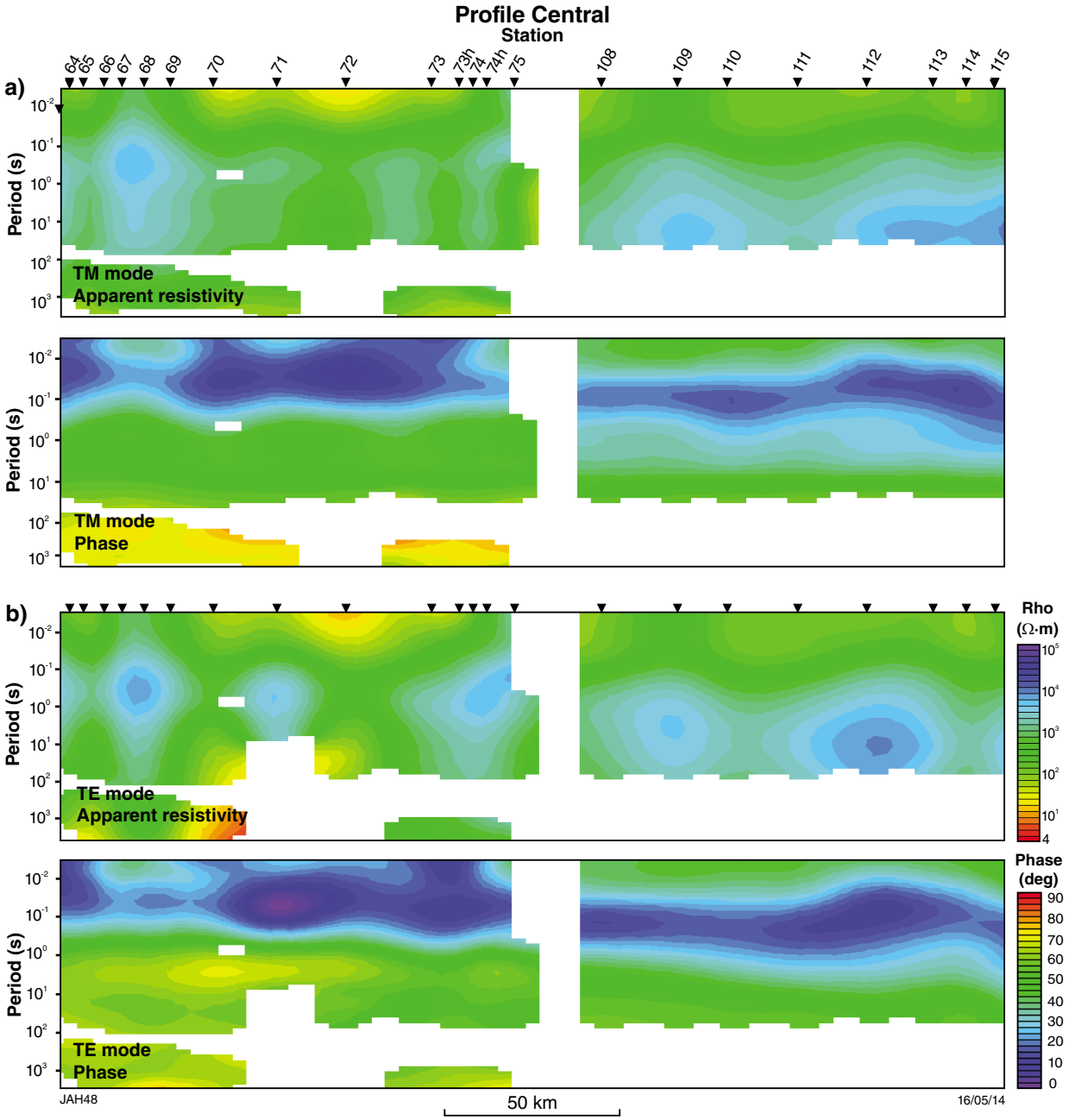

Figure 23. Pseudosections of apparent resistivity and phase in: a) TM-mode; b) TE-mode, along Profile Central comprising data considered to have an acceptable signal to noise level and no significant 3D influence as defined by the skew (β); –5°<β<5°

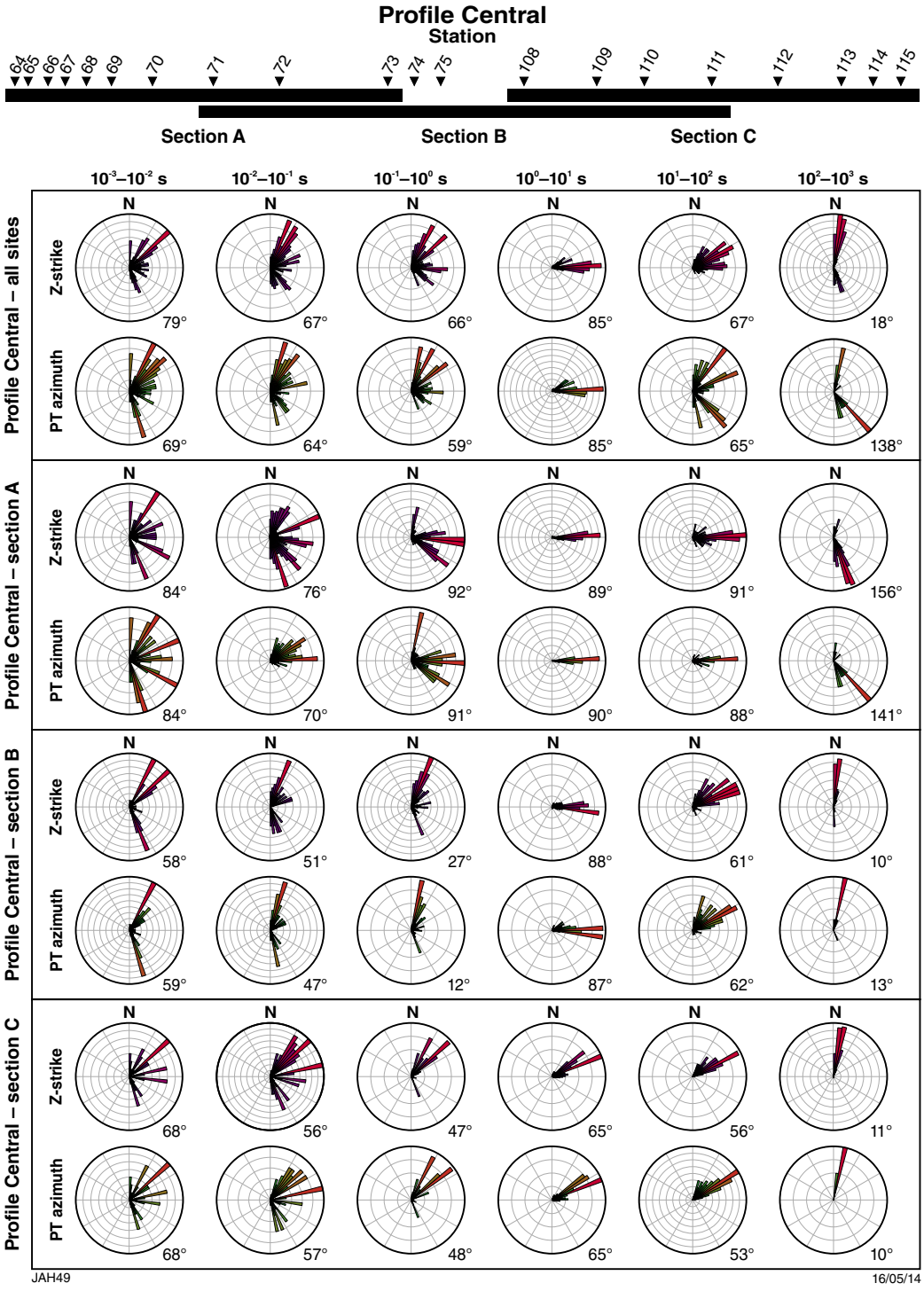

Figure 24. Rose diagrams of phase tensor ellipses and Z-strike orientations at six-decade period bands for sites along Profile Central

Profile East

Phase pseudosections along Profile East are shown in Figure 25. With the exception of the westernmost few sites that indicate a layered 1D Earth to about 100 s, the data in both the apparent resistivities and phases show strong lateral variation and significant differences between the TE- and TM-modes, which is an indication of 2D or 3D structure over most of the period range.

At most sites east of site 116, the data have large induction vectors at periods >0.5 s (Fig. 26). In general, particularly at periods above 10 s, the real component of the induction vectors point east–west, suggestive of a north–south strike direction (Fig. 14).

Phase ellipses along Profile East are elongate with varying trends at periods between 0.1 and 1 s, particularly between sites 115 and 144 (Fig. 27). The ellipses become open from 1 to 100 s; however, at the longest periods (>100 s), the phases ellipses again become elongate with a relatively uniform north–south trend. Phase minimums in the western two-thirds of the profile are <45° to periods of about 10 s, much longer periods than observed in other profiles, suggesting that a resistive unit extends to greater depths. The eastern third of the profile shows phase minimums >45° at short periods, indicating the presence of a conductive unit within the upper crust.

Plots of skew value along Profile East are shown in Figure 28. These show that large portions of the data

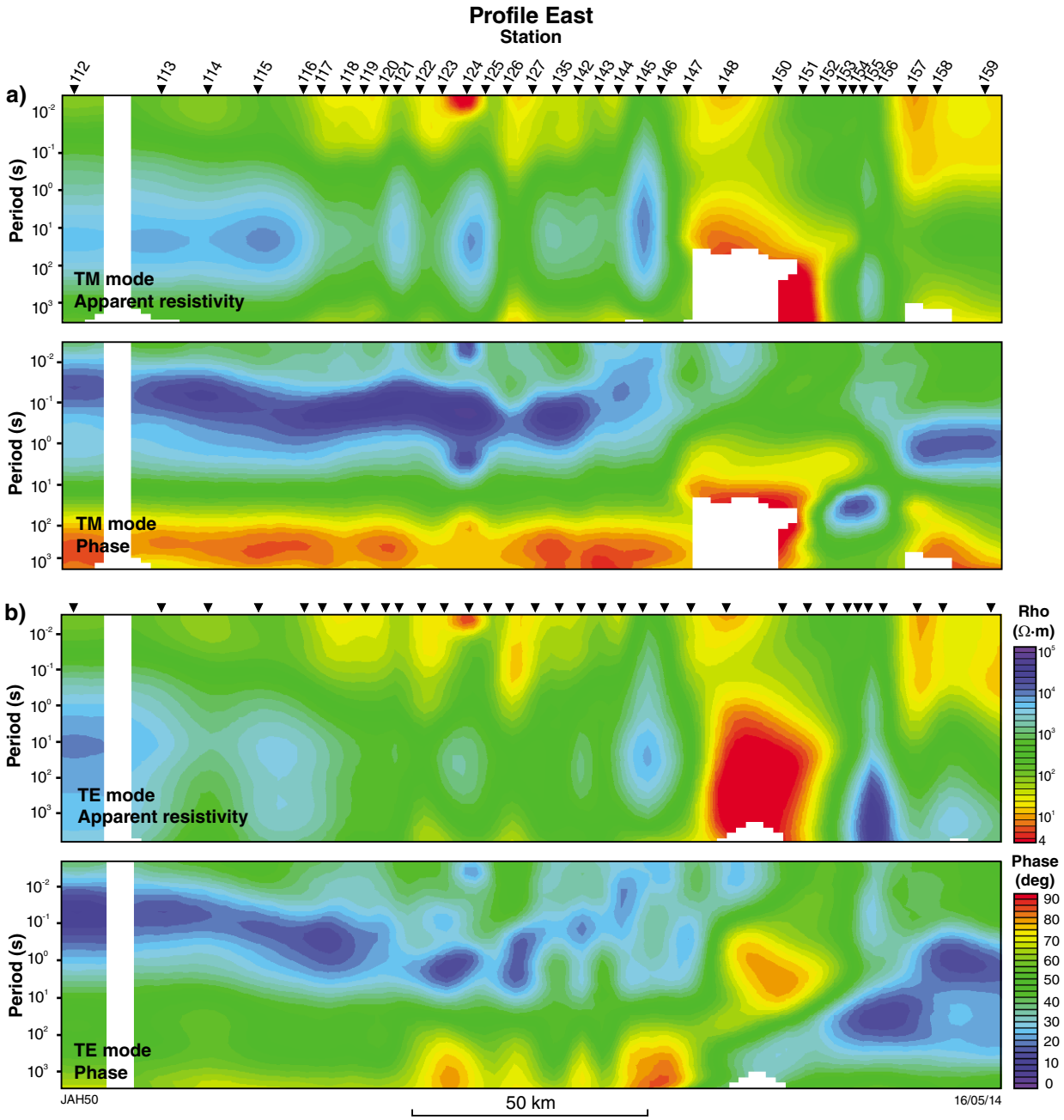

Figure 25. Pseudosections of apparent resistivity and phase along Profile East comprising data considered to have an acceptable signal to noise level for data in: a)TM-mode; b) TE-mode

are estimated to be affected by 3D electrical variations. In addition to periods greater than about 40 s along the entire profile, skew values greater than 5° (or less than –5°) are noted at periods between 0.8 and 8 s in the central part of the profile and at short periods at isolated sites. Pseudosections along Profile East have been generated for apparent resistive and phases with the data estimated to have 3D effects removed (Fig. 29).

Rose diagrams of the strike angle have been generated along Profile East for five-period bands, as data above 100 s has been deemed 3D (Fig. 30). Additionally, Profile East has been divided into four sections to assess variations in strike along the profile. Similar to Profile North and Profile Central, the rose diagrams show a large range in values at periods shorter than 0.1 s, with the exception of section D that has a fairly uniform strike at 0.01 to 0.1s with an average value of 38°. At periods where phase ellipses are elongate (0.1 to 1 s) average strikes are consistent between sections B, C and D with values of 32–38°. Section A has an average value of 61°, consistent with results for the easternmost section along Profile Central (section C). At longer periods, average strike values for all sections are slightly higher ranging from 44–63°.

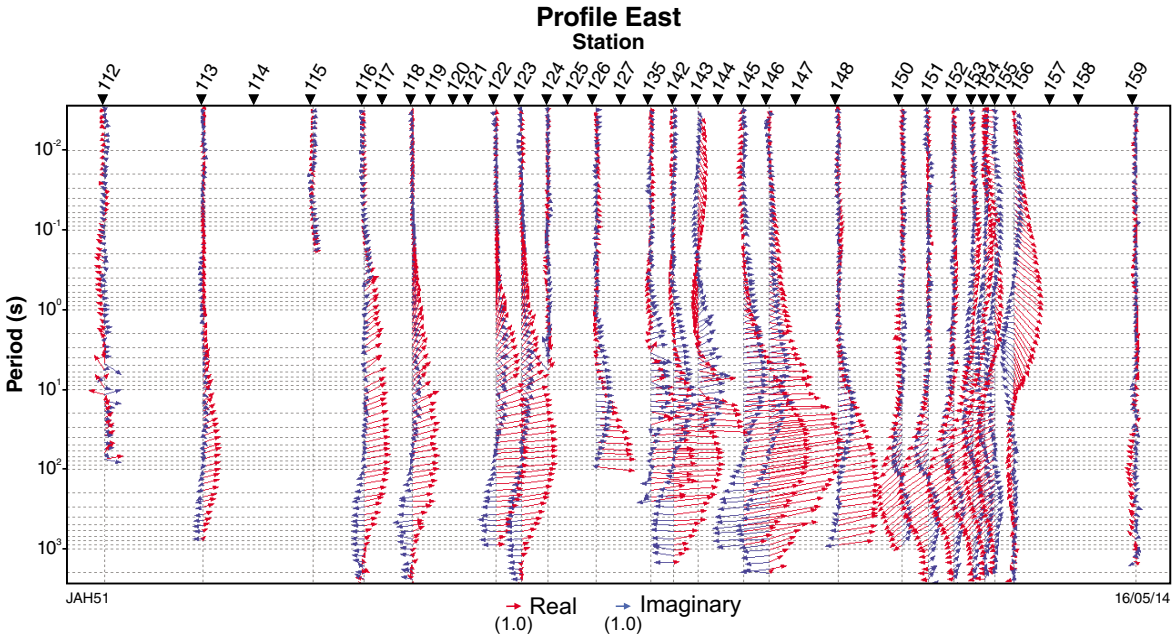

Figure 26. Pseudosection display of induction arrows at each period along Profile East

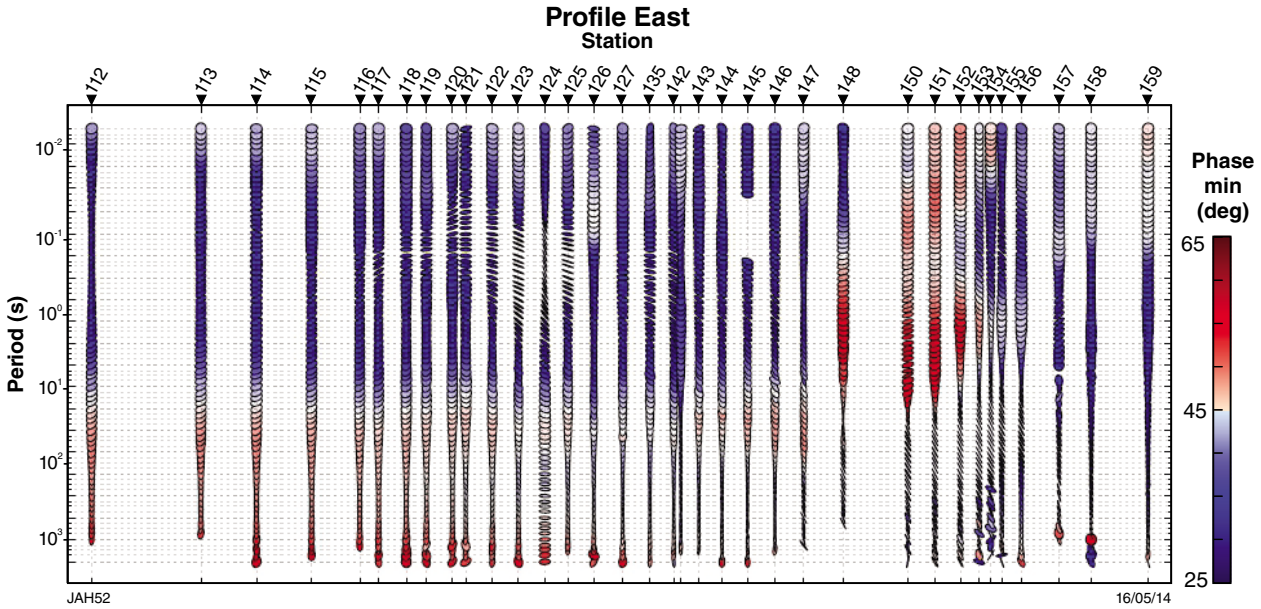

Figure 27. Pseudosection display of MT phase ellipses and phase minimums along Profile East. Blue represents phase minimums below 45° and red represents phase minimums above 45°.

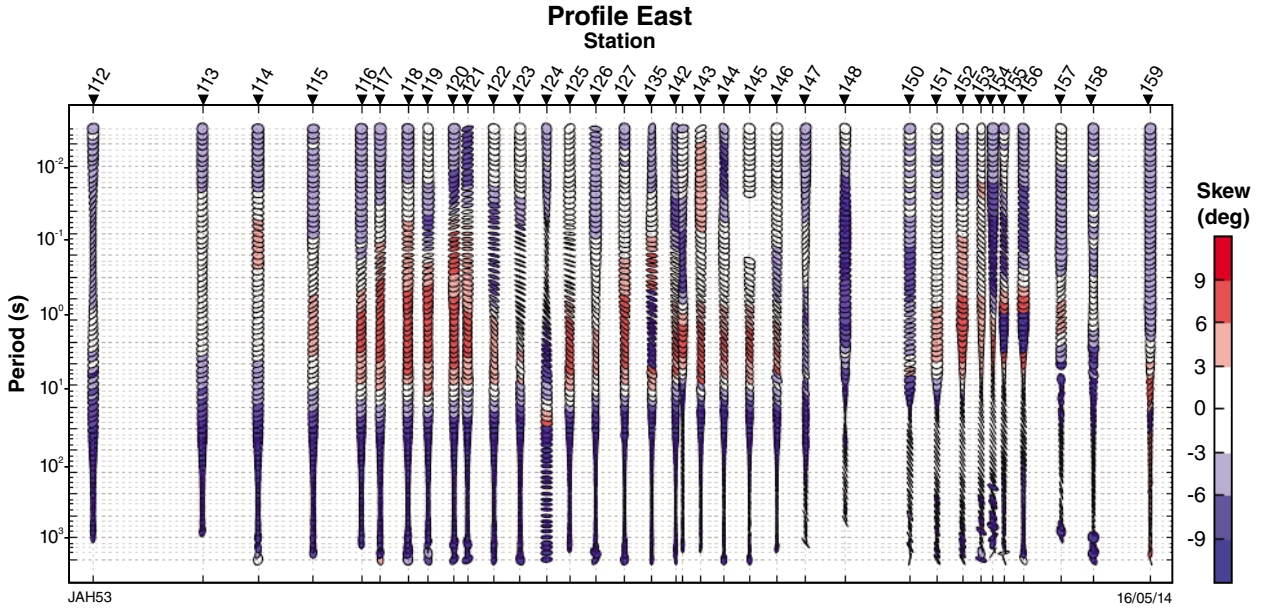

Figure 28. Pseudosection display of MT phase ellipses and skew (β) along Profile East. Dark blue represents skew values below –5° and dark red represents skew value above +5°.

Models have been generated for the whole profile at strike angles of 38 and 62°, with the TE-mode running parallel to the regional geological trend. The westernmost section of the profile (section A) has been modelled along with the sites in section C of Profile Central at a strike angle of 62° (Profile C-E).

Profile West

Pseudosections of the apparent resistivity and phases along Profile West are shown in Figure 31. The apparent resistivity pseudosections show some vertical streaking, possibly due to static shift effects. The apparent resistivities also reveal a dramatic change from highly conductive material west of site 20 to values consistent with the other profiles through the Kimberley Craton. The low resistivities observed to the west are likely responsible for the minimal penetration depths observed (Fig. 10). The phase pseudosections show significant lateral variations, which is an indication of along-profile structure, particularly at the western end of the profile. The TE- and TM-modes are similar to periods of about 1 s.

Induction vector magnitudes are small for most sites east of site 52 to periods of at least 100 s, suggestive of a layered subsurface (Fig. 32). Between sites 23 and 51, induction vectors show moderate to large magnitudes over the whole frequency range and many sites show a change in direction with depth, indicating a conductive unit that dips towards the southwest. The easternmost sites have small vectors to periods of 1 s. At periods greater than 0.01 s, induction vectors, in general, point northeast and southwest, suggestive of a northwest–southeast geoelectric strike angle consistent with the regional geologic trend (Fig. 14). At periods greater than about 1 s, induction vectors uniformly point toward the southwest, which is an indication of the presence of a large conductive unit off-profile to the west.

Phase ellipses along Profile West are shown in Figure 33. Elongated phase ellipses are observed at periods up to about 1s for sites 20–25 and 31–54 with varying long axis trends. The westernmost sites, have highly elongated ellipses at periods greater than 1 s, and have a general northwest–southeast trend. The westernmost sites predominantly show phase minimums that are >45° to periods up to 1 s. This may result from effects of electrically conductive sedimentary rocks of the Canning Basin that underlie a more resistive surface cover. At longer periods, the phase minima are all <45° suggesting that the data do not penetrate to depths below the resistive crust. The easternmost sites show phase minima <45° up to periods that vary between 0.1 and 1 s. These variations may be due to changes in the thickness of near-surface conductive layers or in the depth of the resistive crust.

Plots of skew along Profile West are shown in Figure 34. Effects of 3D distortion are estimated to be most severe at the west end of the profile at periods greater than about 80 s. Pseudosections of apparent resistivity and phase along Profile West have been generated with the data estimated to have 3D effects removed (Fig. 35).

Where induction vector magnitudes are large, the rose diagrams for the westernmost sites indicate an average strike angle of 129° at periods of 1 to 10 s, and 142–149° at periods >10 s (where the data show 3D distortion), a strike of 83–90° for the central sites at periods between 1 and 10 s and 128° for 10 to 100 s, and 87–92° for the eastern sites at periods of 1 to 100 s (Fig. 36).

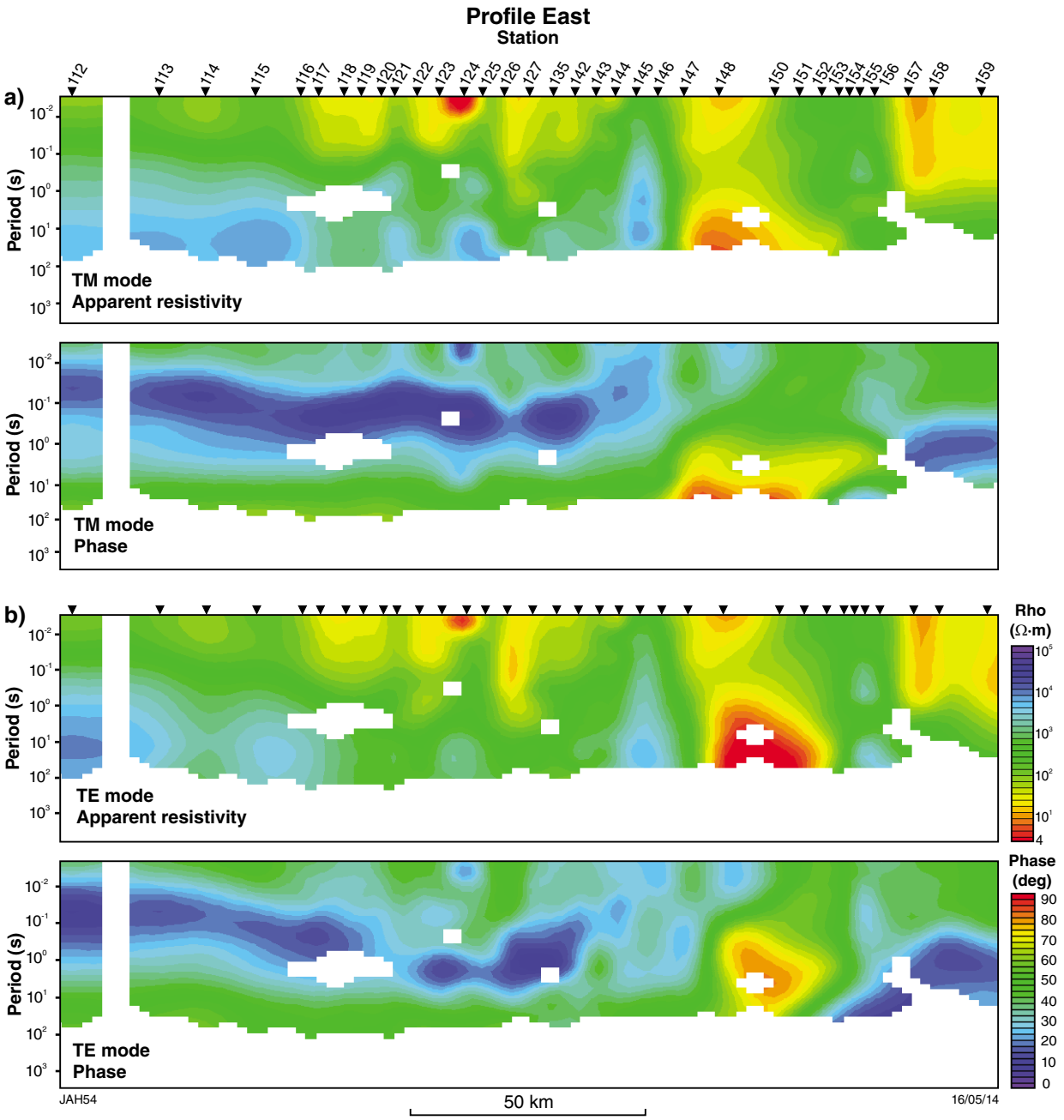

Figure 29. Pseudosections of apparent resistivity and phase in: a) TM-mode; b) TE-mode, along Profile East comprising data considered to have an acceptable signal to noise level and no significant 3D influence as defined by the skew (β); –5°<β<5°

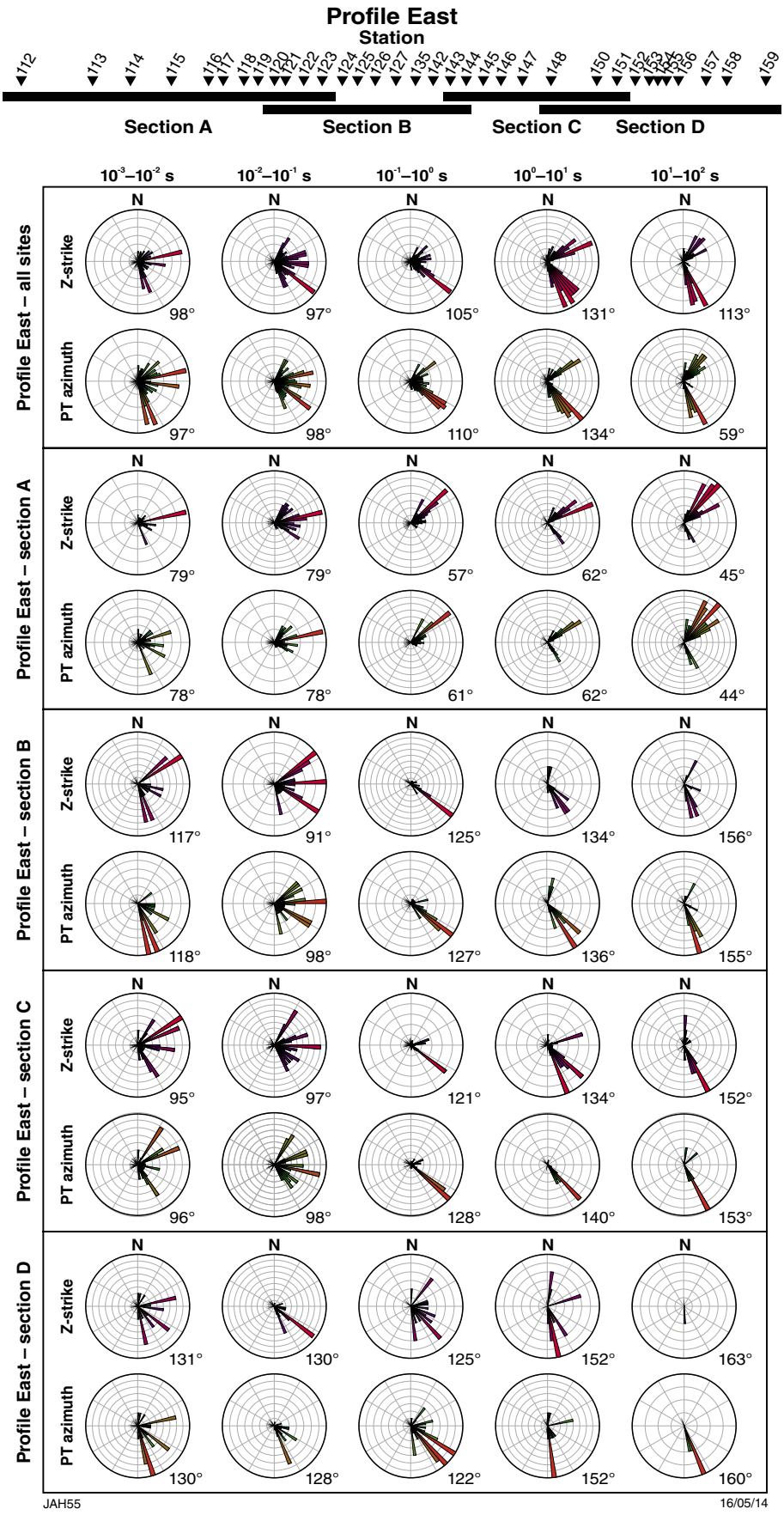

Figure 30. Rose diagrams of phase tensor ellipses and Z-strike orientations at six-decade period bands for sites along Profile East

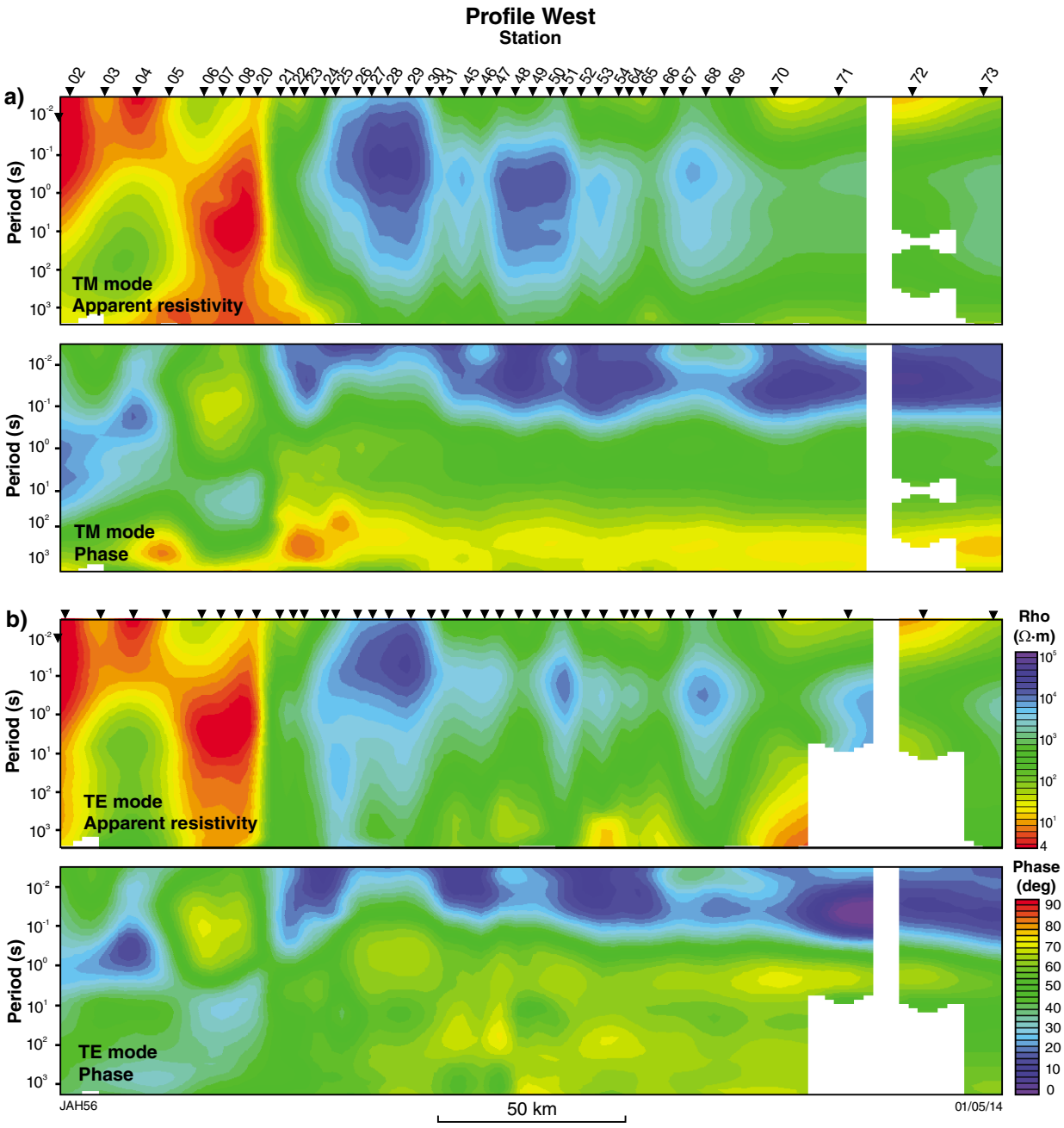

Figure 31. Pseudosections of apparent resistivity and phase along Profile West comprising data considered to have an acceptable signal to noise level for data in: a) TM-mode; b) TE-mode

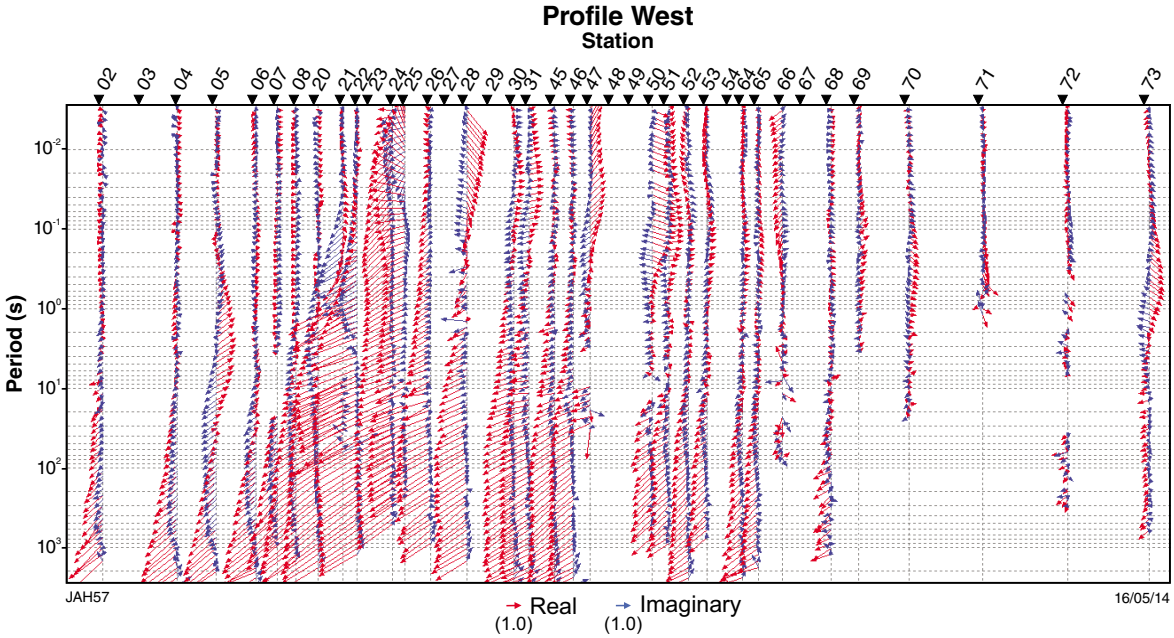

Figure 32. Pseudosection display of induction arrows at each period along Profile West

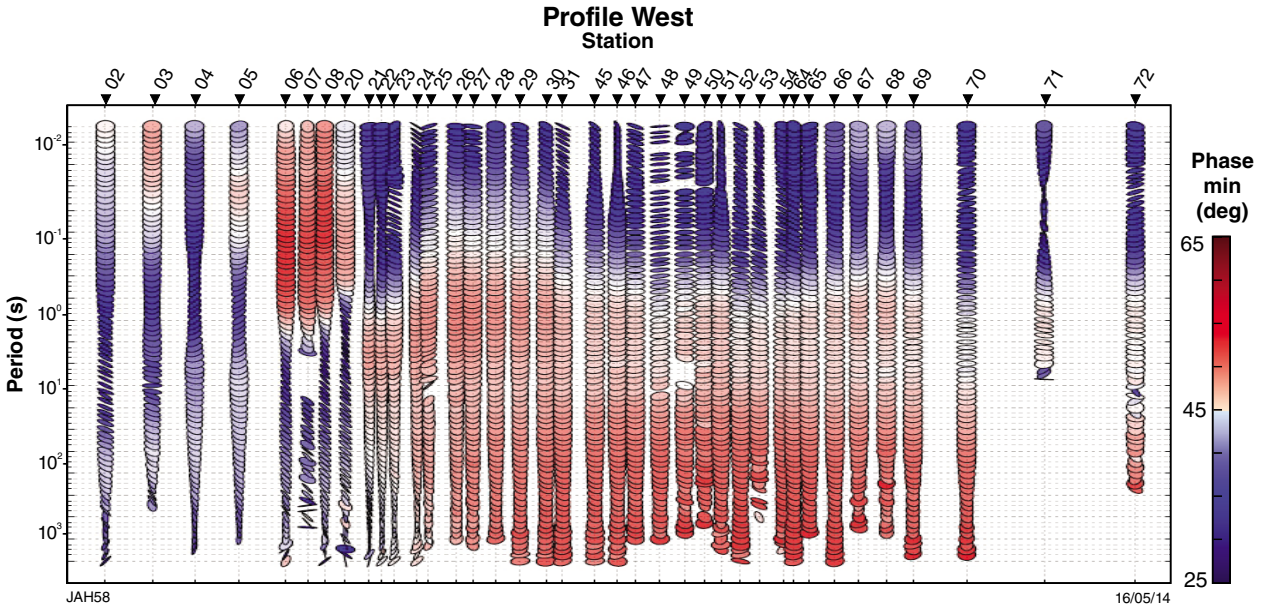

Figure 33. Pseudosection display of MT phase ellipses and phase minimums along Profile West. Blue represent phase minimums below 45° and red represents phase minimums above 45°.

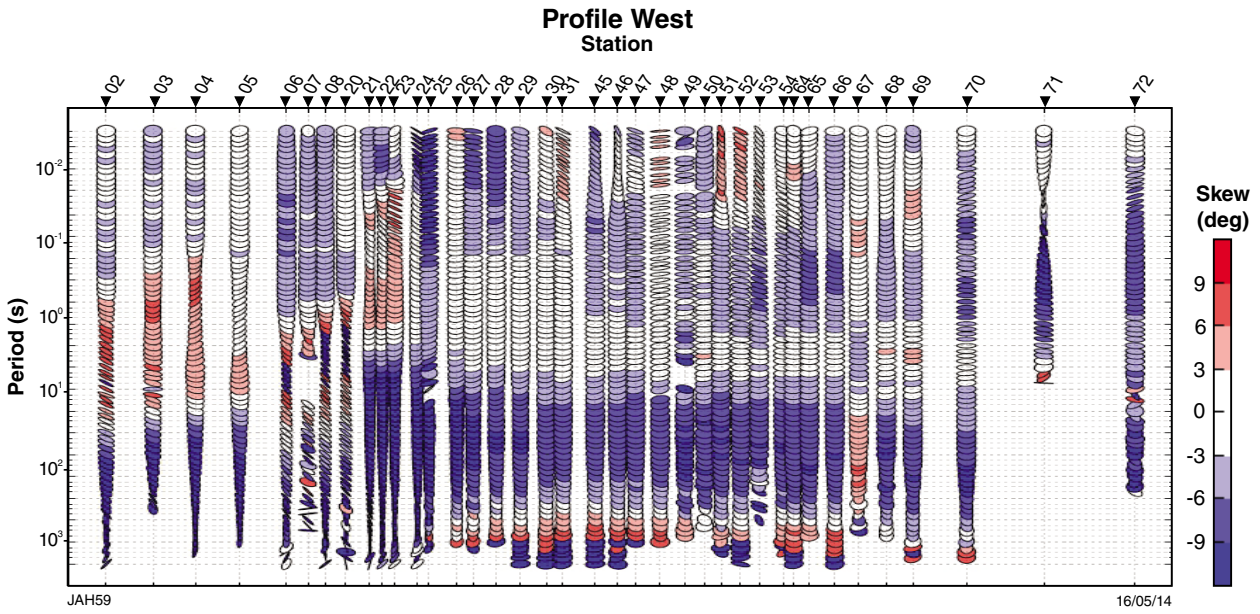

Figure 34. Pseudosection display of MT phase ellipses and skew (β) along Profile West. Dark blue represents skew values below –5° and the dark red color represents skew value above +5°.

At periods of 0.1 to 1 s, there is a consistent strike average of 91–92° for the whole profile and each of the sections except section A. Note that due to the high conductivities observed in the pseudosections, the data for the sites in section A do not penetrate to the same depths as those in sections B and C.

Models have been generated using strikes of 0 and –52°. The strike of 0° is inconsistent with regional geological trends at the surface, and with induction vectors, making it difficult to resolve the 90° ambiguity in strike analysis. TE-mode (parallel to geoelectric strike direction) is assumed to be north–south, simply because the profile runs south-southwest to north-northeast. A geoelectric strike of –52° is roughly consistent with the regional geological trend and with induction vectors.

Cross profiles

Pseudosections of the apparent resistivity and phases along each of the cross profiles are shown in Figure 37. Profile Cross 1 has along-profile variations in both apparent resistivity and phase with some difference between the phases of the TM- and TE-modes, suggestive of two/three dimensionality in the data. Along Profile Cross 2, pseudosections of apparent resistivities show high conductivities at the northeastern end of the profile, possibly limiting penetration depths. The phases show little lateral structure and the data in the TM- and TE-modes are similar, indicative of a layered subsurface. Similar to Profile Cross 2, Profile Cross 3 has high conductivities at the southwestern end and the phases show little lateral structure at periods greater than 0.001 s, indicative of a layered subsurface. Along Profile Cross 4, lateral variations in both apparent resistivity and phase are observed with significant difference between the phases of the TM- and TE-modes, suggestive of strong two/three dimensionality in the data.

Induction vectors are plotted for each of the Cross Profiles in Figure 38. Along Profile Cross 1, at periods greater than 0.1 s, induction vectors are large and uniformly point towards to the southwest indicating the presence of a large conductive unit to the southwest of the profile, but do not provide information on the geoelectric strike angle crossing Profile Cross 1. Profile Cross 2 has short induction vectors at periods up to 10 s, suggestive of homogeneous layered structure at shallow depths. At greater periods, similar to Profile Cross 1, induction vectors uniformly point towards the southwest; however, vector lengths are shorter consistent with interpretation of a conductive unit to the southwest of Profile Cross 1. Short induction vectors are observed over the entire period range along Profile Cross 3, consistent with a layered subsurface. Along Profile Cross 4, induction vectors are shorter periods of about 5 s. Larger vector magnitudes at longer periods point towards the east. East of Profile Cross 4, along Profile East, induction vectors point westward indicating a north–south trending conductor to the east and parallel to the trend of Profile Cross 4.

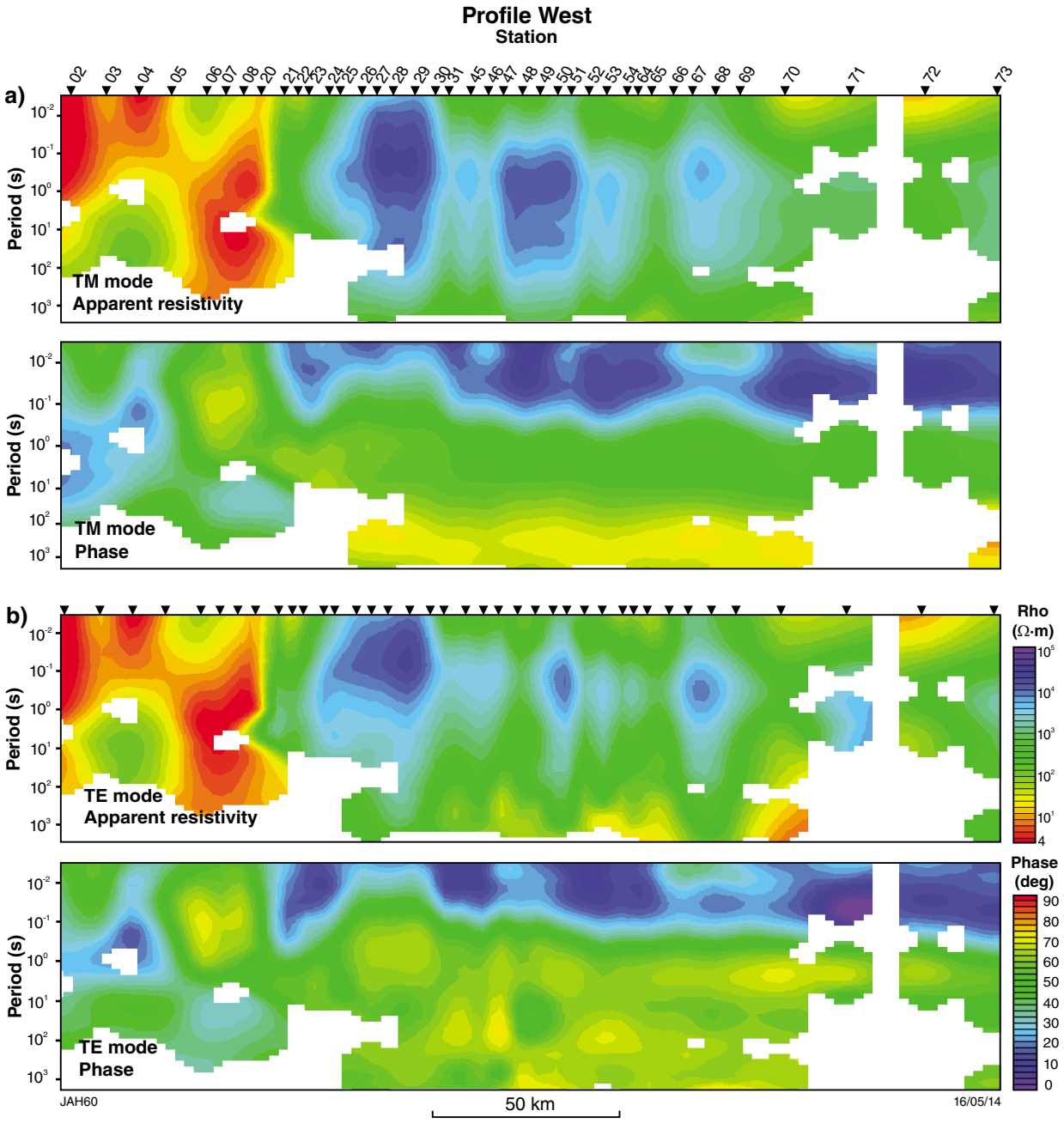

Figure 35. Pseudosections of apparent resistivity and phase in: a) TM-mode; b) TE-mode, along Profile West comprising data considered to have an acceptable signal to noise level and no significant 3D influence as defined by the skew (β); –5°<β<5°

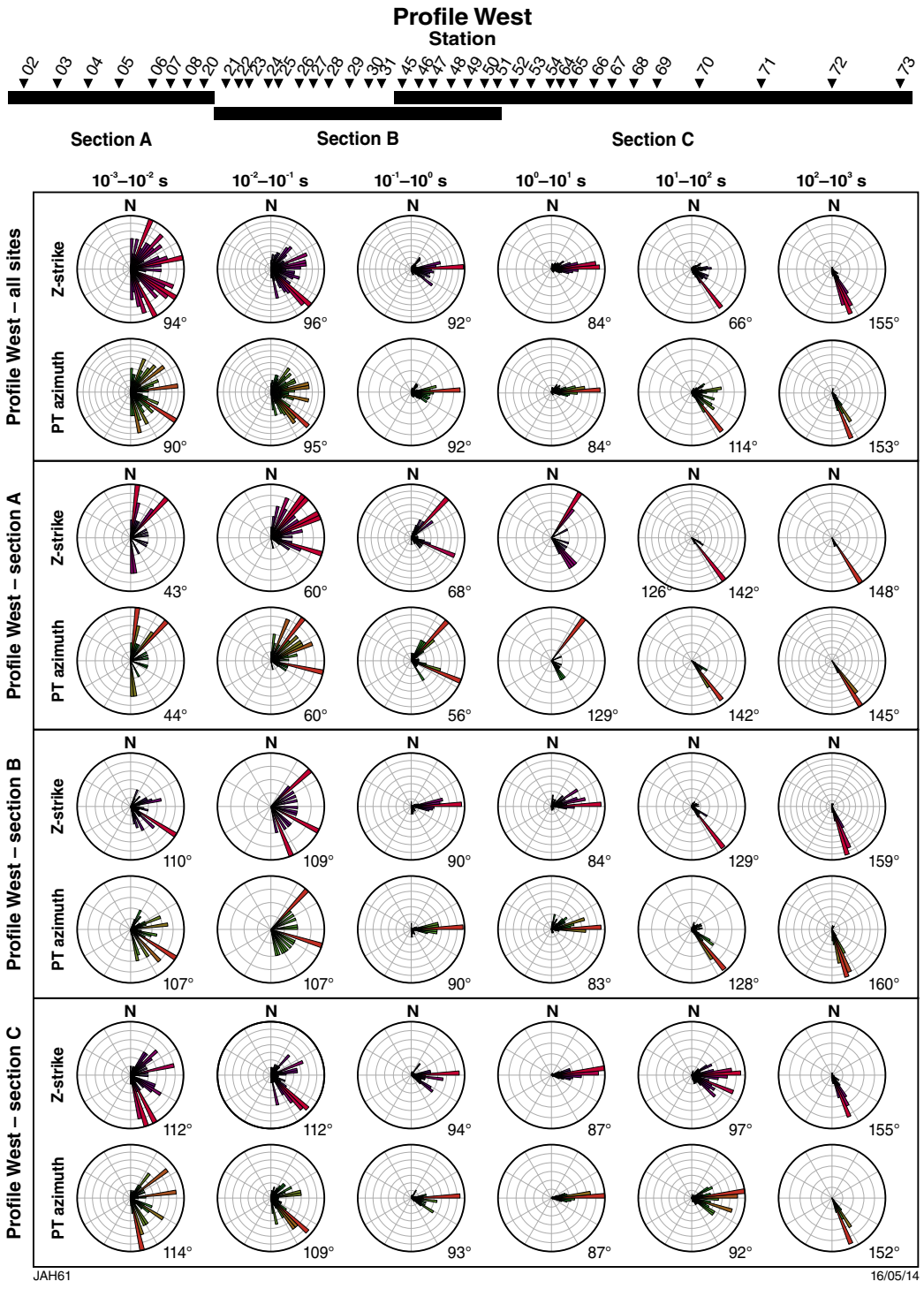

Figure 36. Rose diagrams of phase tensor ellipse and Z-strike orientations at six-decade period bands for sites along Profile West

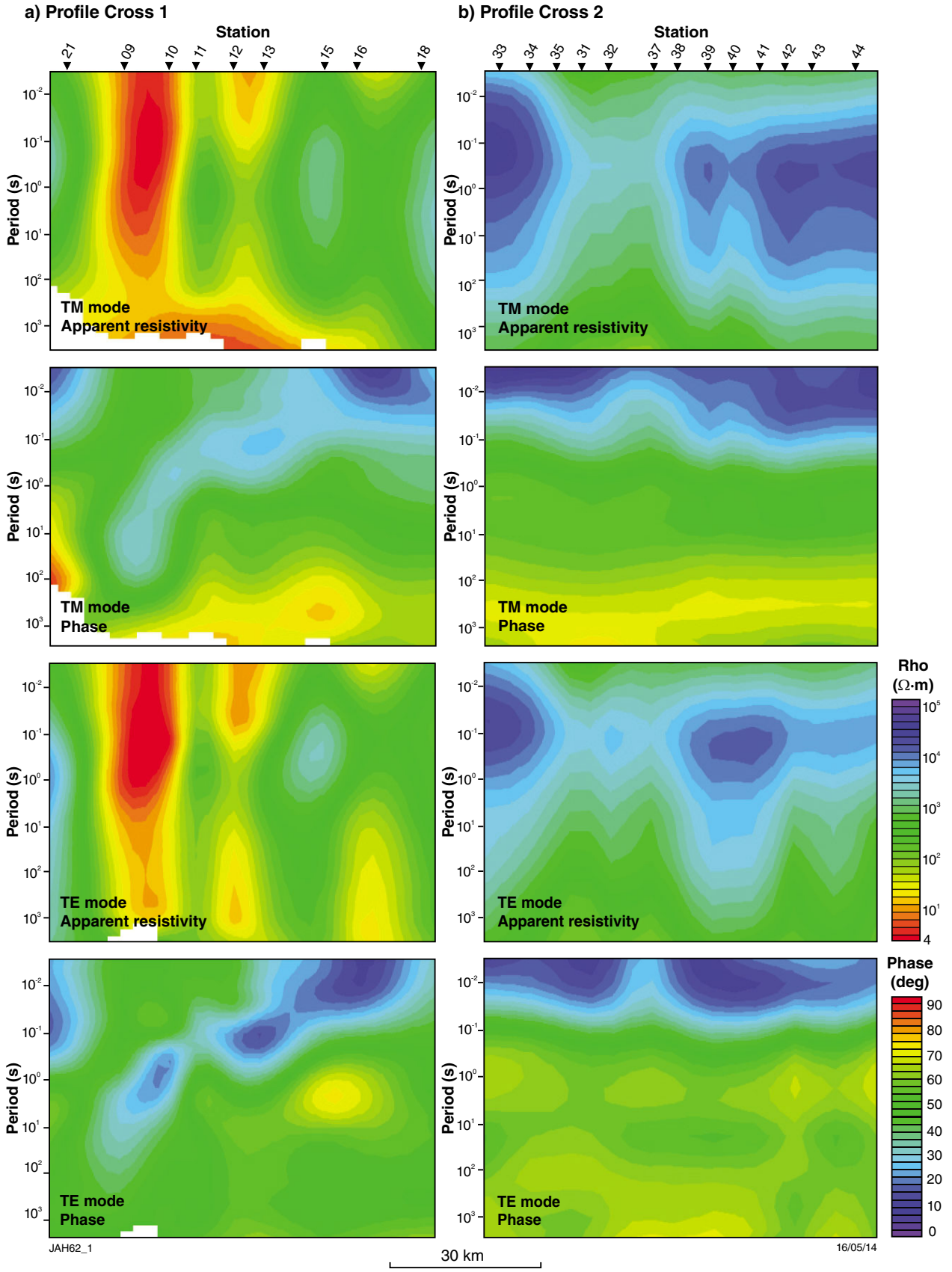

Figure 37. Pseudosections of apparent resistivity and phase in data considered to have an acceptable signal to noise level in both the TM- and TE-modes along: a) Profile Cross 1; b) Profile Cross 2; c) Profile Cross 3; d) Profile Cross 4

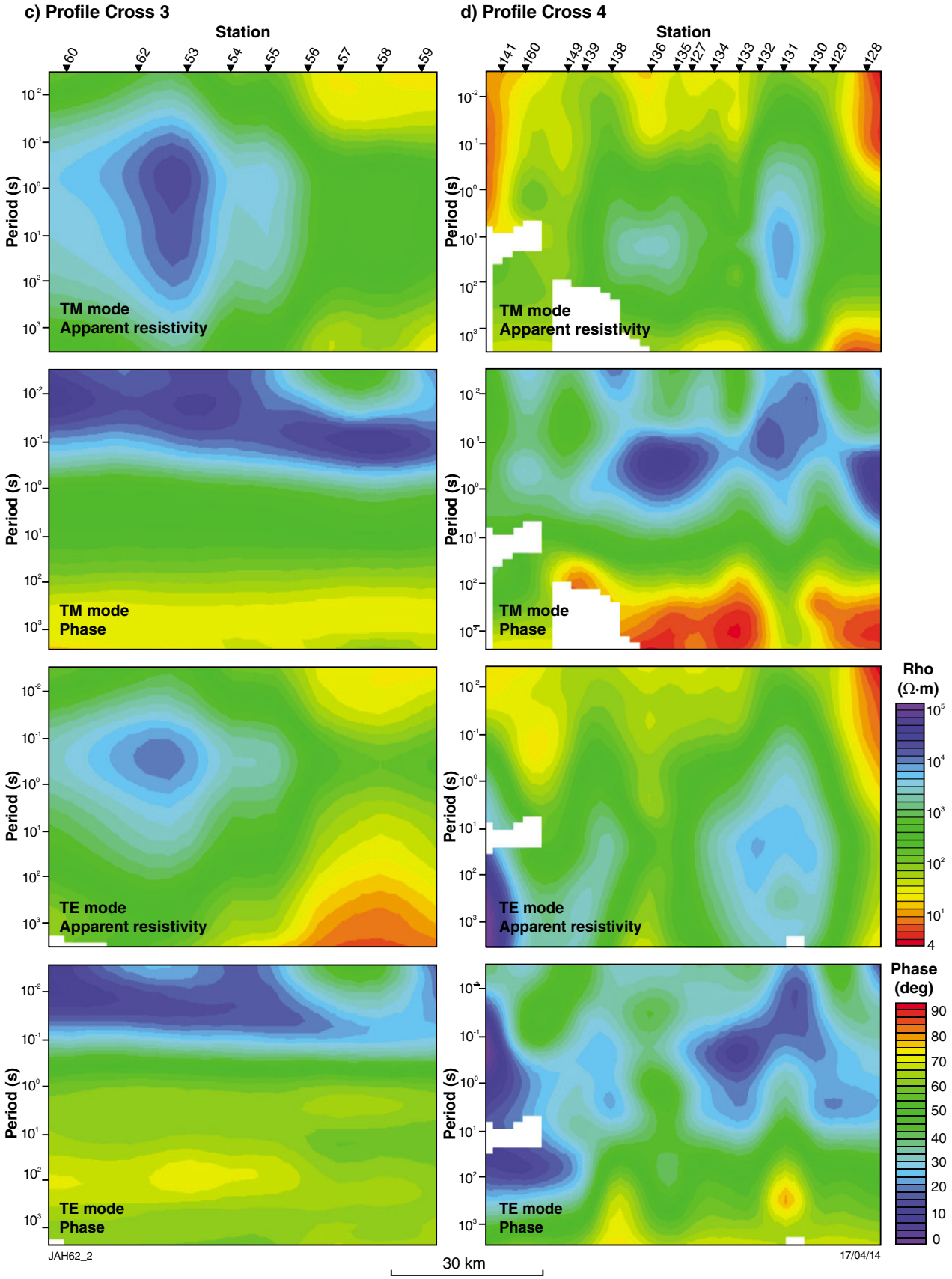

Figure 37. continued

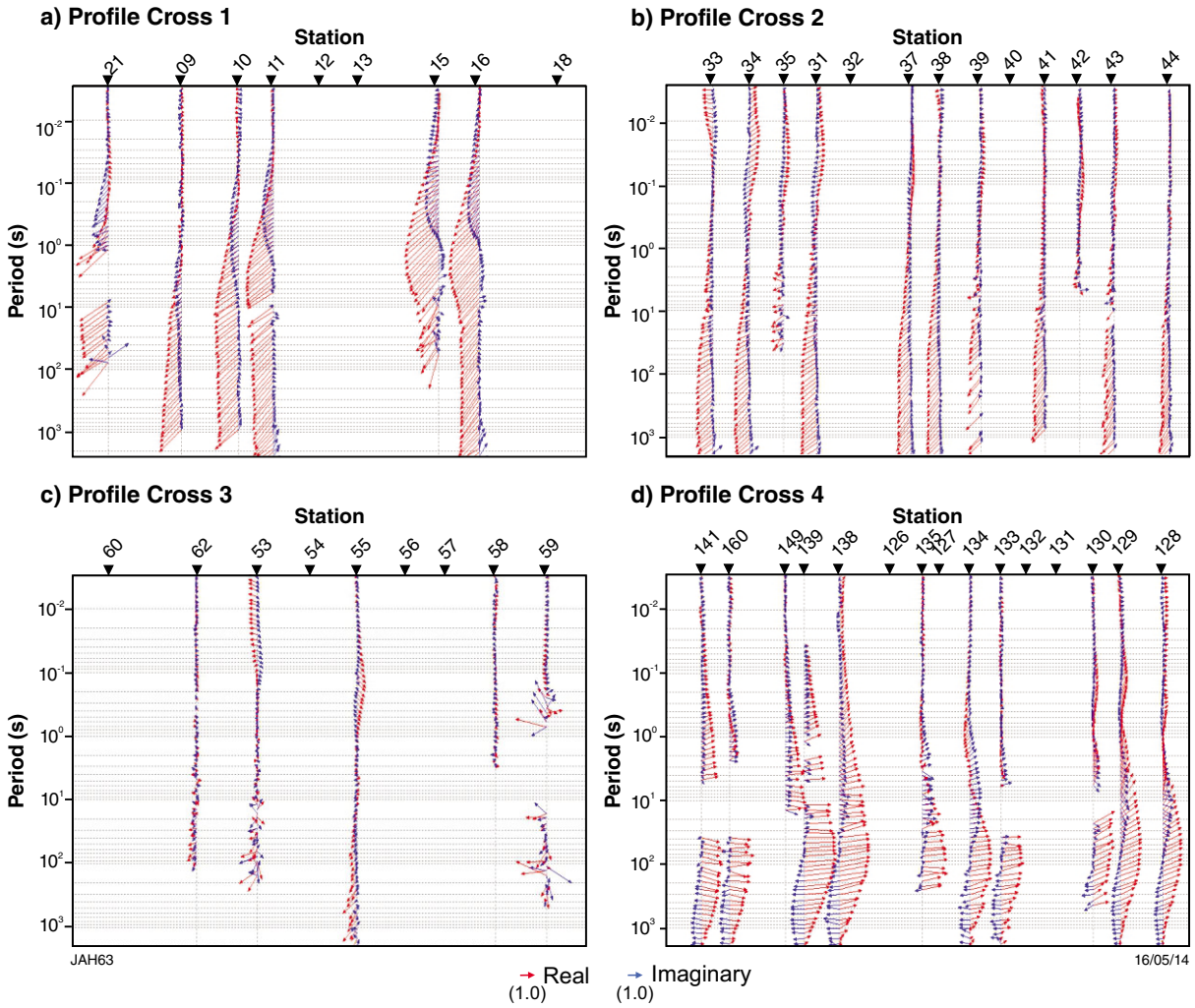

Figure 38. Pseudosection of induction arrows at each periods along: a) Profile Cross 1; b) Profile Cross 2; c) Profile Cross 3; d) Profile Cross 4

Phase tensor ellipses and phase minimums are plotted in pseudosection format along each of the cross profiles (Fig. 39). Profile Cross 1 shows northwest–southeast trending elongate phase ellipses at periods of 0.05 to 10 s and again at periods >100 s for most of the sites, and at periods of 0.1 to 1000 s for sites 09 and 10. Low-phase minimums are observed to about 1 s at most sites and increase to above 45° at periods greater than about 7 s, with the exception of sites 09 and 10 that show high-phase minimums at short periods only. The high-phase minima at shorter periods indicate a thick near-surface conductive unit beneath these sites, likely limiting penetration depths. Along Profile Cross 2, elongate phase tensor ellipses are shown at periods between 0.01 and 0.1 s with a trend that changes from northeasterly to northwesterly along the profile. Phase minima are below 45° to about 0.5 s and above 45° at longer periods, possibly indicating a change from resistive crust to less resistive lower crust or upper mantle. Profile Cross 3 shows slightly elongate phase ellipses between periods of 0.02 and 0.2 s, with open ellipses at longer periods. In general, phase minima are low (possibly resistive crust) to about 1 s and high at periods above 10 s. Along Profile Cross 4, in contrast to the other cross profiles, phase tensor ellipses are most elongate at periods longer than 10 s with a roughly north–south trend. At shorter periods, phase ellipses varying significantly in ellipticity and trend from one site to the next, is an indication of complex structure at shallow depths. Phase minima are below 45° over most of the period range. Lack of evidence for a shallow conductive layer (high-phase minimums at short periods) suggests that a resistive unit extends to great depths beneath the profile.

Pseudosections of skew values at each period interval along each of the Cross profiles are shown in Figure 40. Profile Cross 1 has skew values <–5° at periods greater than about 10 s at nearly all sites, an indication of 3D distortion at depth beneath the profile. Both Profiles Cross 2 and Cross 3 show skew values within the range of –5° to +5° at most sites to periods of 1000 s, indicating

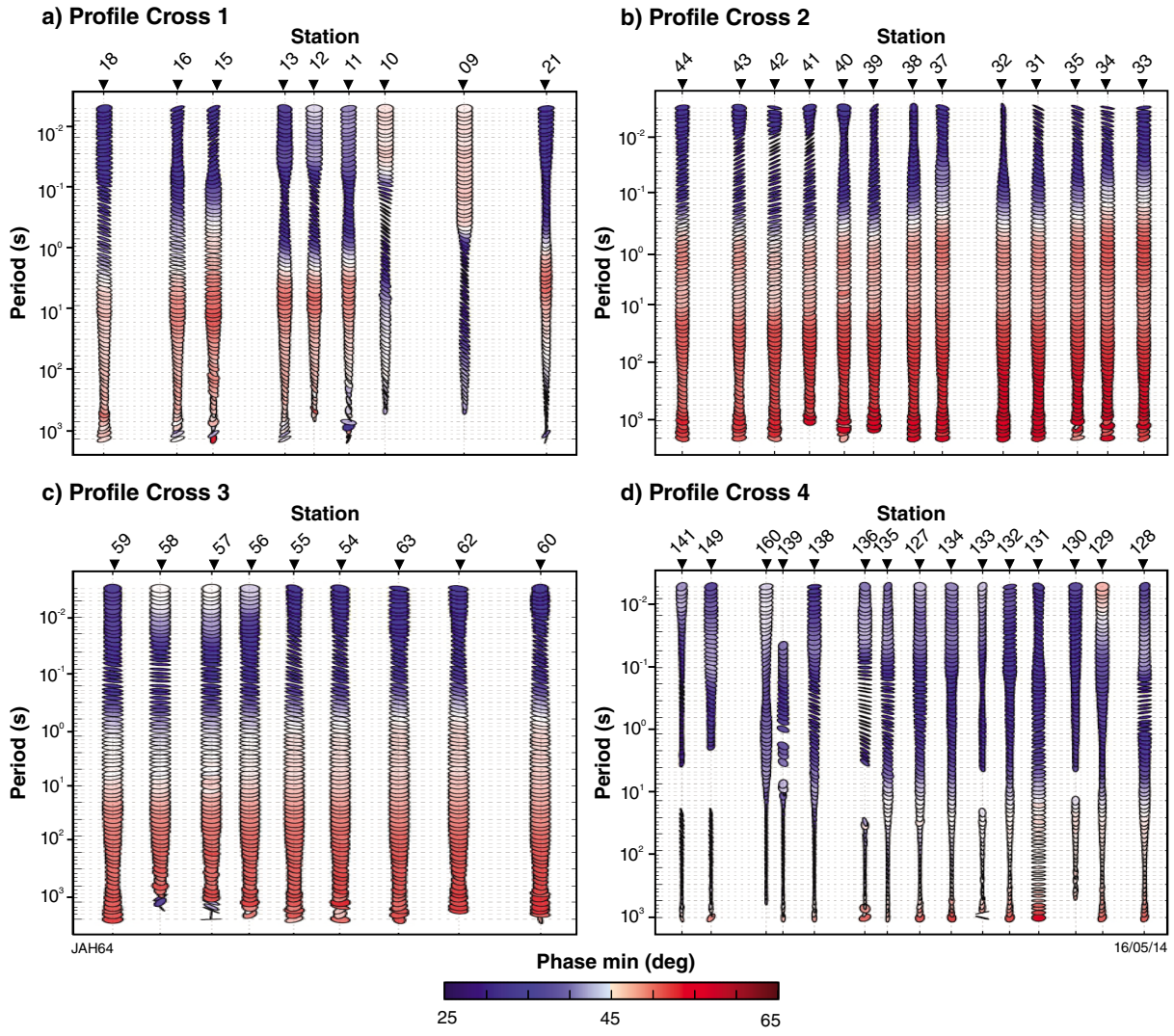

Figure 39. Pseudosection display of MT phase ellipses and phase minimums along: a) Profile Cross 1; b) Profile Cross 2; c) Profile Cross 3; d) Profile Cross 4. Blue represents phase minimums below 45° and red represents phase minimums above 45°.

that 3D distortion effects are minimal. Profile Cross 4 has high absolute skew values at long periods, longer than 30 s at all sites and at periods longer than 0.2 s at some sites, suggesting that a large portion of the data is influenced by 3D distortion effects (Fig. 40). Apparent resistivity and phase values with data presumed to be unaffected by 3D distortion for the TM- and TE-modes along Profiles Cross 1, Cross 2, Cross 3, and Cross 4 are shown in Figure 41.

Rose plots showing the phase tensor and z azimuths for each site along the cross profiles reveal scattered strike directions with no preferred direction at periods above 0.1 s (Fig. 42). Profile Cross 1 has average preferred strike directions ranging from 137– 140° between 0.1 and 10 s and 154 and 159° between 10 and 1000 s. Models have been generated along Profile Cross 1 at –47° and –26°; however, –47° roughly corresponds to the trend of the profile and may not accurately represent the 2D subsurface. Data along Profile Cross 2 has a preferred strike direction of 59– 72° for periods between 0.1 and 1000 s. Models have been generated along Profile Cross 2 at 70° and –20° as it is difficult to ascertain the TE-mode. Rose diagrams along Profile Cross 3 reveal a preferred geoelectric strike direction of 112–129° at periods of 0.01 to 1 s, a strike of 94° at periods between 1 and 100 s, and a strike of 151° at periods greater than 100 s. Models have been generated at –55° (along strike), 94°, and 4° to observe differences in model features and root mean square (RMS) value, as it is difficult to ascertain the TE-mode direction. The strike directions for Profile Cross 4 are highly variable with a large degree of scatter at most periods with a slight preference of approximately 0° at periods above 10 s, data that has been deemed 3D. Models have been generated at a strike angle of 60° (estimated for Profile East) and 0°, along Profile Cross 4.

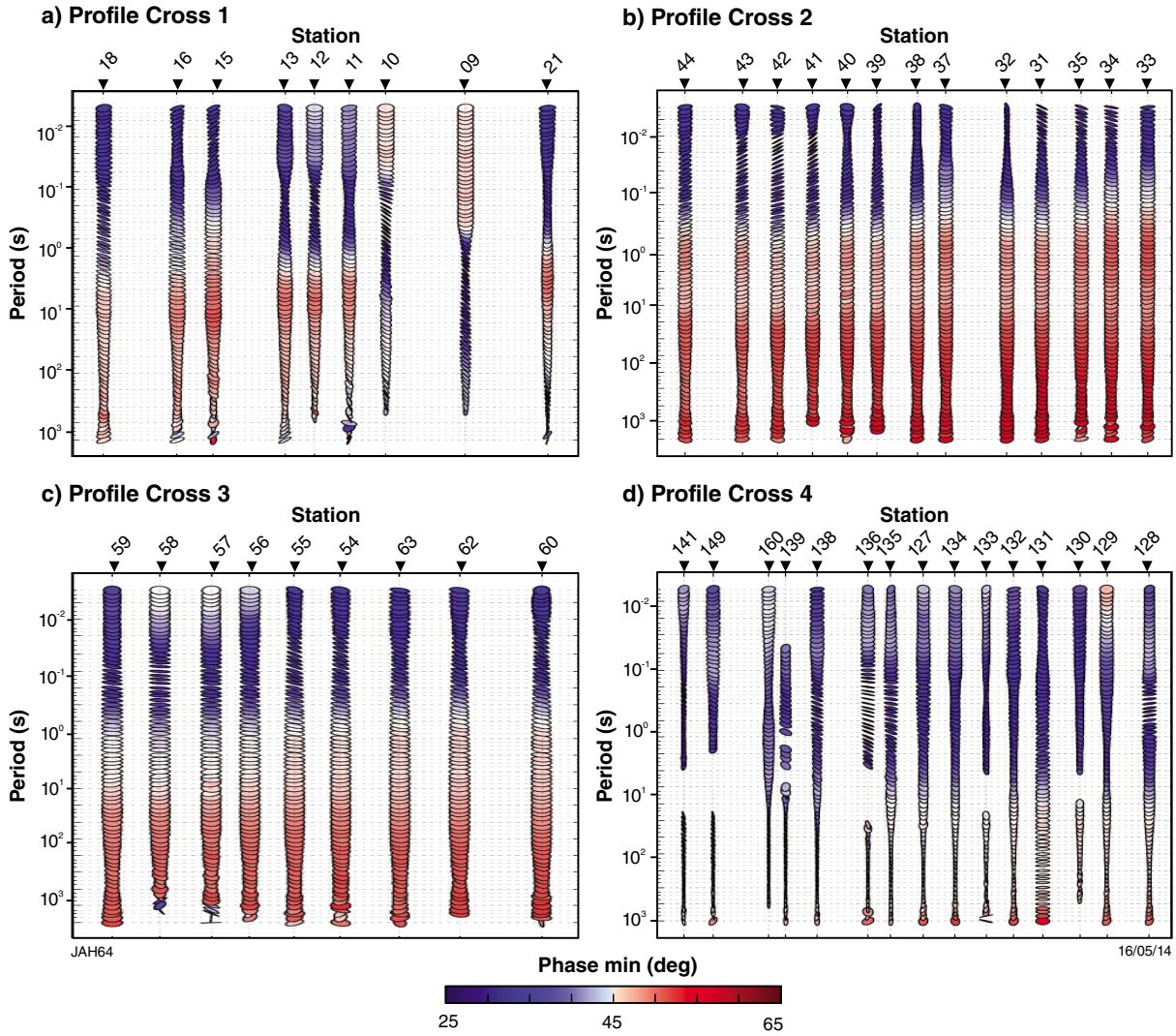

Figure 40. Pseudosection display of MT phase ellipses and skew (β) along: a) Profile Cross 1; b) Profile Cross 2; c) Profile Cross 3; d) Profile Cross 4. Dark blue represents skew values below –5° and dark red represents skew value above +5°.

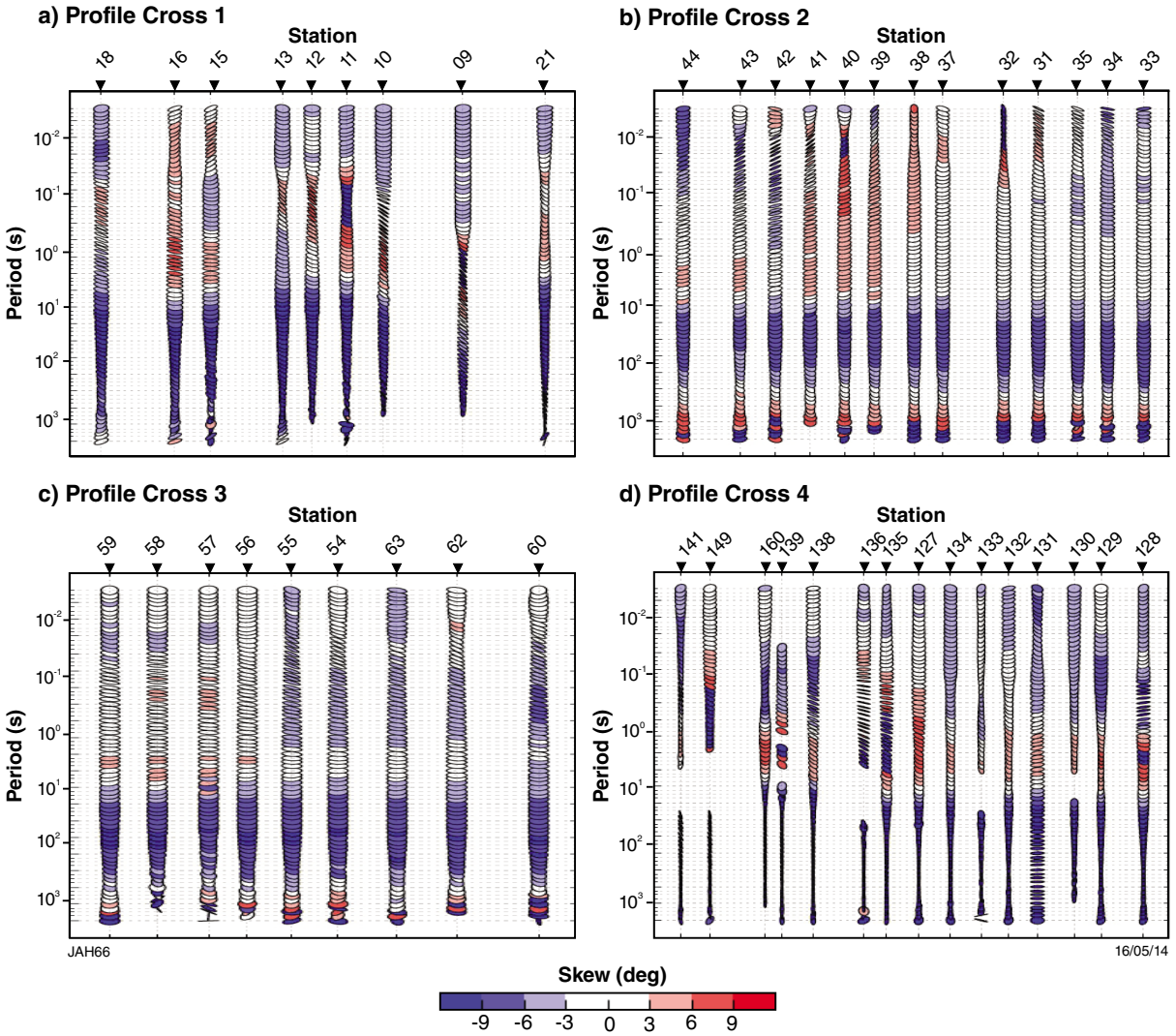

Figure 41. Pseudosections of apparent resistivity and phase in both comprising data considered to have an acceptable signal to noise level and no significant 3D influence as defined by the skew (β); –5°<β<5° along: a) Profile Cross 1; b) Profile Cross 2; c) Profile Cross 3; d) Profile Cross 4

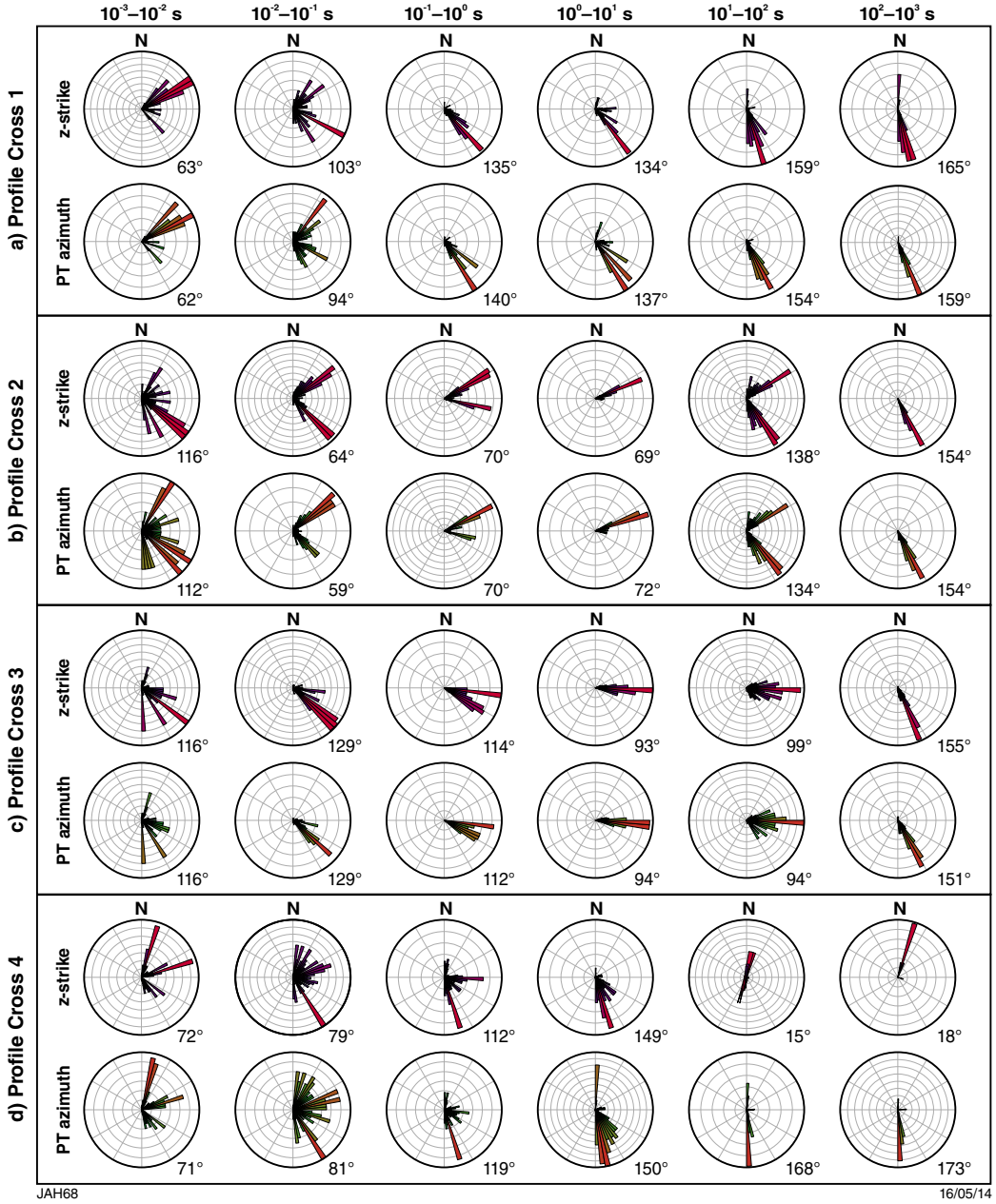

Figure 42. Rose diagrams of phase tensor ellipses and Z-strike orientations at six-decade period bands for sites along: a) Profile Cross 1; b) Profile Cross 2; c) Profile Cross 3; d) Profile Cross 4

Data modelling

The WinGLink interpretation software package, that implements the Rodi and Mackie (2001) inversion algorithm, was used to generate 2D models along the three main profiles and the four smaller cross profiles. Inversions were executed from the MT responses recalculated at the appropriate geoelectric strike direction(s). The inversion program searches for the smoothest, best-fit model with the least deviation from the starting model (Mackie and Madden, 1993). The models derived, therefore, represent the minimum structure required to fit the data with an acceptable misfit.

Models were generated along each profile using different components of the data, with and without the inclusion of data deemed 3D, and at differing strike angles in order to assess the change in the observed conductivity structure and resolve features that are robust in the data. Each inversion included data in the period range of 0.004 to 1000 s, was initiated with a homogeneous half-space of 500 Ω•m, and ran for a minimum of 200 iterations. The phases were set with a 5% error floor, and where applicable, the Tipper error was set to an absolute value of 0.02. Initially the apparent resistivities were set with an error floor of 20%, and subsequently reduced to 10% to assess and account for static shift effects. A uniform grid Laplacian operator and tau value of three were applied. The selected preferred model for each profile was generated with data presumed to be affected by 3D distortion removed, structure that appears to be robust between inversions using different data components and modelling parameters, and with the lowest overall RMS value.

To test the reliability of the preferred resistivity model produced by the inversion, feature testing was undertaken on various distinct conductive and resistive zones in each cross section. This method involves removing and replacing conductivity values of a group of cells within the model with the conductivity of the adjacent area. For example, in the case of discrete conductive zone these are replaced with resistive values similar to those outside the feature being tested. A forward calculation is first performed on the data to assess the change in RMS value and then the resistivity in the area is 'frozen' and the inversion process restarted. This means the inversion algorithm is forced to try and match the observations using conductivity variations outside this area. This form of test is designed to see whether conductivity variations in another part of the model can be used to fit the data, i.e. does there need to be a zone of anomalous conductivity in the area being tested? The second type of feature test allowed the modelling algorithm to modify values within the test zone ('unfrozen') to see if the anomalous zone reappears and, if so, how its geometry is affected. This test is less rigorous than the first in terms of the presence or absence of a feature, but allows the reliability of the feature's geometry to be assessed, i.e. does it reappear in the same form as in the original model?

Profile North

Results of 2D modelling along Profile North are shown in Figure 43. Consistent with variable induction vectors and phase-tensor ellipses at short periods, the structure imaged at depths less than about 30 km is highly dependent on the assumed geoelectric strike angle. A reasonable model along the entire profile cannot be attained at a single strike angle for upper- to mid-crustal depths. Although the conductivity values are inconsistent, at lower crust and upper mantle depths there is consistent lateral structure, suggesting that these variations are relatively robust. Plots of the RMS values at each site for each strike direction show that the model for the southern half of the profile best fits the data at a strike angle of –65°, and the northern half of the model fits the data at a strike angle of 57°. This change in strike angle may be a result of crosscutting conjugate dyke-filled fractures that trend roughly northwesterly across the southern half of the profile and northeasterly across the northern half.

Our preferred model along Profile North was generated by stitching together the models inverted using data edited for 3D effects at a strike angle of –65° for the southern half of the profile and 57° for the northern half of the profile (Fig. 44). The model identifies a thin near-surface conductive layer (about 200 Ω•m to <3 km), likely sedimentary or volcanic rocks within the Kimberley Basin. A very resistive (>20 000 Ω•m) crust is imaged to depths ranging between about 20–30 km, and is generally underlain by a lower crustal conductive layer (about 200 Ω•m) with crustal depth estimates ranging 35–42 km (red dashed line in Fig. 44). The resistive crust is cross cut by moderately resistive features that extend from the surface down to the lower crustal conductive layer. In some places these features line up with surface traces of fractures or faults (white dashed lines in Fig. 44). The lower crustal conductive layer appears to be absent beneath sites 93 and 94, and north of site 102, and is located slightly deeper beneath sites 81–84 (black ellipses in Fig. 44). At upper mantle depths, the southern extent of the profile has resistivity values of about 3000 Ω•m to at least 120 km. The values decrease towards the north to about 600 Ω•m and may mark a change in mantle properties from north to south (black dashed line in Fig. 44). The models that included data with high skew values show this decrease in mantle resistivity as a zone beneath sites 76–86 and show mantle resistivities increasing to values >2000 Ω•m north of site 86 (Fig. 43). The preferred model (high skew data removed) does not show this increase in mantle resistivity to the north and sensitivity testing needs to be undertaken to ascertain the penetration depths of these data.

Feature testing has been undertaken to ascertain the robustness of several features along Profile North (Fig. 45). These include the absence of a lower crustal conductor beneath sites 93 and 94 (feature A), the depth extent of the resistive upper mantle at the south end of the profile (feature B), the change in upper mantle resistivity

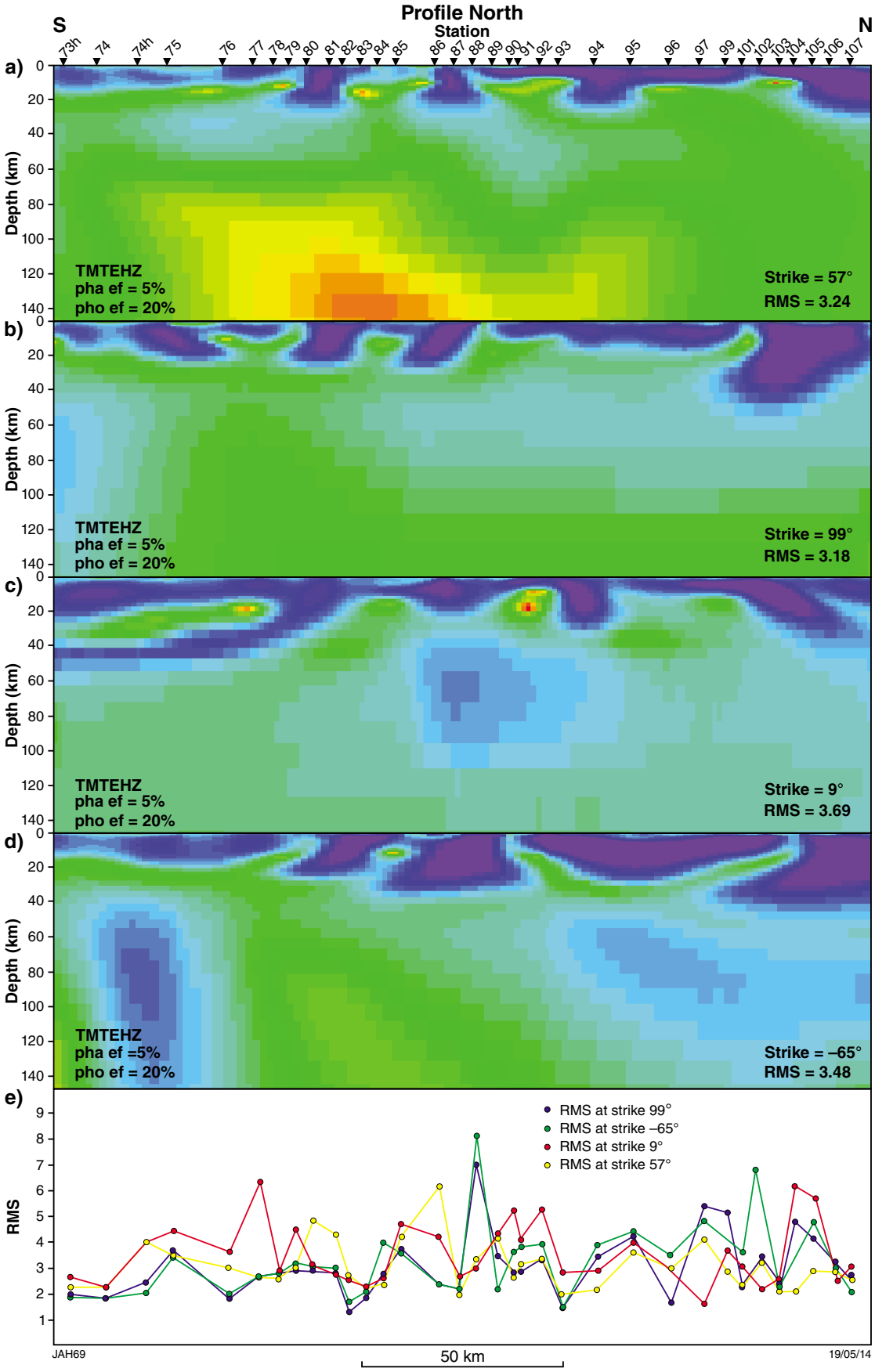

Figure 43. Results of 2D modelling along Profile North using all data not deemed exceptionally noisy with the data rotated to a geoelectric strike angle of: a) 57°; b) 99°; c) 9°; d) –65°; e) RMS misfit value for each site along the profile for each model. See Figure 1 for the locations of the profiles.

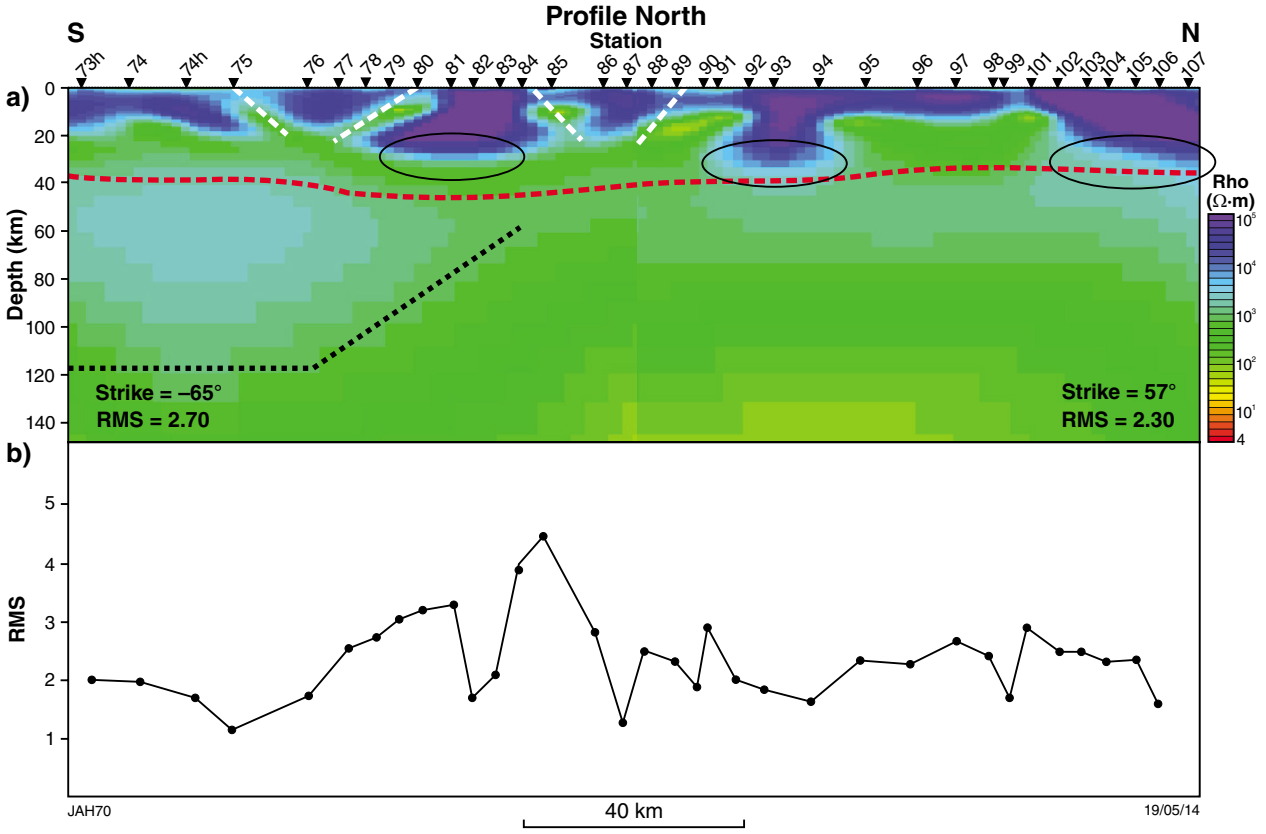

Figure 44. The preferred 2D model along Profile North and the RMS values for each site. The warm colours represent areas that are conductive and blue represents resistive. The dashed white lines mark steeply dipping features observed in the upper crust; the black ellipses highlight areas with a resistive lower crust; the red dashed line marks the approximate crust–mantle boundary; and the black dashed lines mark possible variations in the upper mantle. See Figure 1 for the locations of the profiles.

from south to north (feature C) and the sensitivity of upper mantle structure beneath the north end of the profile (feature D). For each feature, the preferred model was altered and a forward model was run, then subsequent iterations were executed with the altered model, both frozen and unfrozen, to observe how the model adapts to the change.

Adding a lower crustal conductor beneath site 93 and 94 (feature A) resulted in an increase in the overall RMS value from 2.29 to 2.79 (Fig. 45a). With the altered feature frozen, the model was not able to obtain an RMS value as low as the preferred model (Fig. 45d). Unfrozen, after 100 iterations, a resistive lower crust returned and the RMS value was lowered to 2.30 suggesting that this feature is required by the data (Fig. 45e). Altering the depth of resistive mantle beneath the southern extent of the profile (feature B) resulted in a very slight increase in RMS from 2.69 to 2.71 (Fig. 45a). Subsequent iterations, for both a frozen and unfrozen feature, showed little change to the altered model and saw the RMS value reduced to 2.69 indicating that the model may not be sensitive to this structure (Fig. 45b,c). Features C and D — alterations to the uppermost mantle beneath the central and eastern part of the profile — showed little to no change to the overall RMS value after forward modelling, which is an indication that the data may not be sensitive to structure at depths greater than about 60 km (Fig. 45a,f– i).

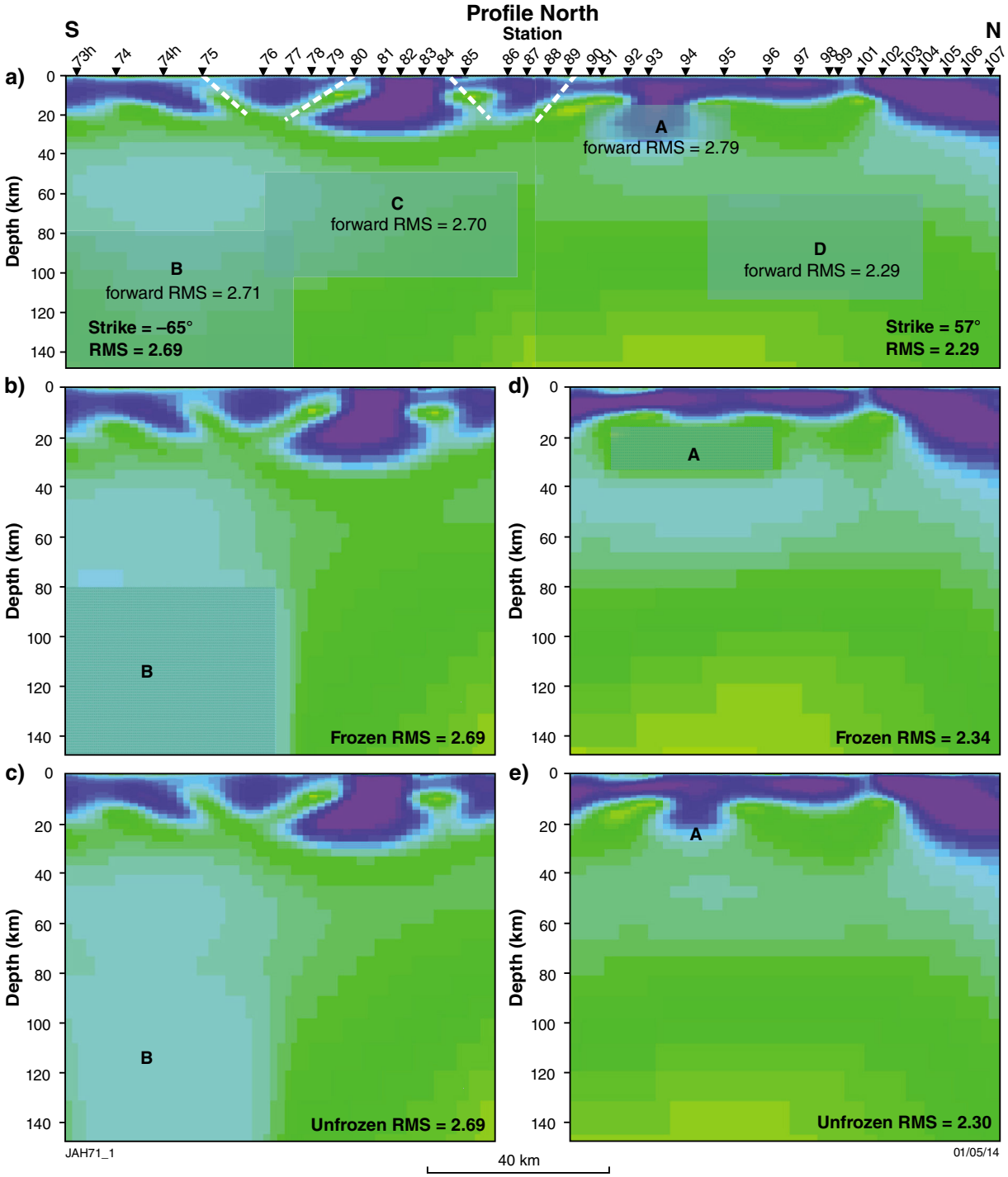

Figure 45. **Assessment of the reliability of features with anomalous electrical properties in the preferred resistivity cross-section along Profile North: a) shows the lettered features that are altered and the resulting RMS values after forward modelling; b) new model with feature B frozen; c) new model with feature B unfrozen; d) new model with feature A frozen; e) new model with feature A unfrozen; f) new model with feature C frozen; g) new model with feature C unfrozen; h) new model with feature D frozen; i) new model with feature D unfrozen**

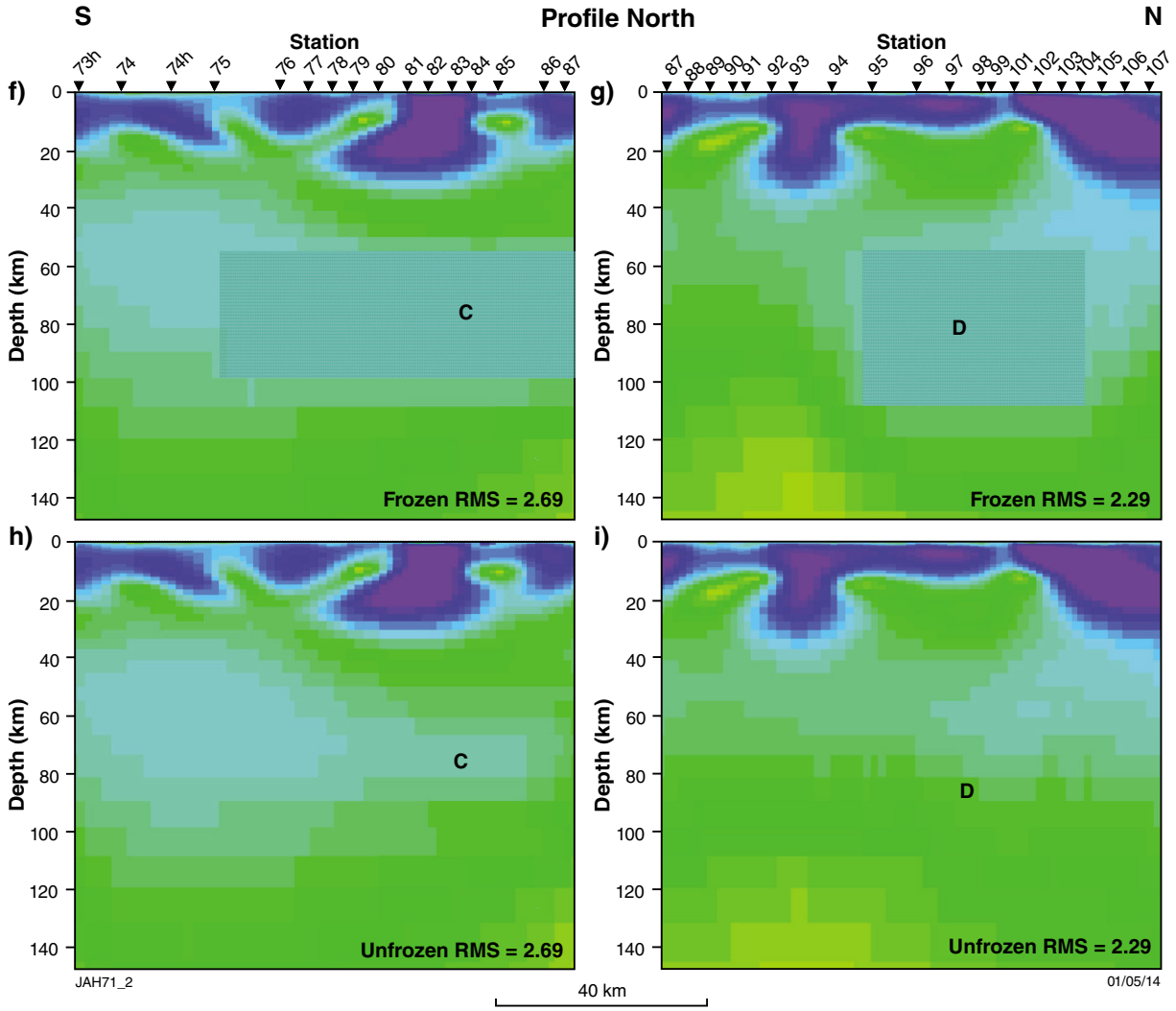

Figure 45. continued

Profile Central

2D models generated along Profile Central, using all of the data acquired are shown in Figure 46. Although there is some variation between models with differing strike angles, many features appear to be robust, with the lowest overall RMS value obtained with data rotated to a strike angle of –45°. RMS values plotted for each site at each strike direction also show that a strike of –45° is suitable for most sites along the profile.

Our preferred model along Profile Central was generated using data edited to remove 3D effects at a strike angle of –45° (Fig. 47). As results of strike analysis showed that the easternmost sites are better modelled with a strike of 62°, models were also generated for the easternmost sites of Profile Central and the westernmost sites of Profile East independently (Profile C-E; Fig. 47). A thin near-surface conductive layer (about 200 Ω•m) is imaged that varies in thickness up to about 5 km, likely representing the volcanic and sedimentary units of the Kimberley Basin. The upper- to mid-crust is resistive (>10 000 Ω•m) to roughly 10 km along most of the profile, thickening to 20 km beneath sites 73H–75 (consistent with results along Profile North), and thickening to 40 km beneath site 111. This resistive layer is cut by less resistive features (marked by white dashed lines in Fig. 47) that correspond to mapped dyke-filled fractures at the surface. With the exception of sites 111 and 115, the resistive crust is underlain by a lower crustal conductor (about 200 Ω•m) with crustal thickness estimates between 27 and 40 km (red dashed line in Fig. 47). The black dotted lines in Figure 47 mark conductivity changes in the upper mantle with values of about 600 Ω•m to the west, increasing to typical mantle values of about 5000 Ω•m beneath the central part of the profile to depths of at least 120 km. The eastern part of the profile at a strike of –45° shows the uppermost mantle to be resistive, with values of 5000–10 000 Ω•m to depths of 90 km beneath site 108 and shallowing to 60 km beneath site 115. At a strike of 62°, the upper mantle is shown to be very resistive (>10 000 Ω•m) between 50 and 120 km beneath sites 110–115.

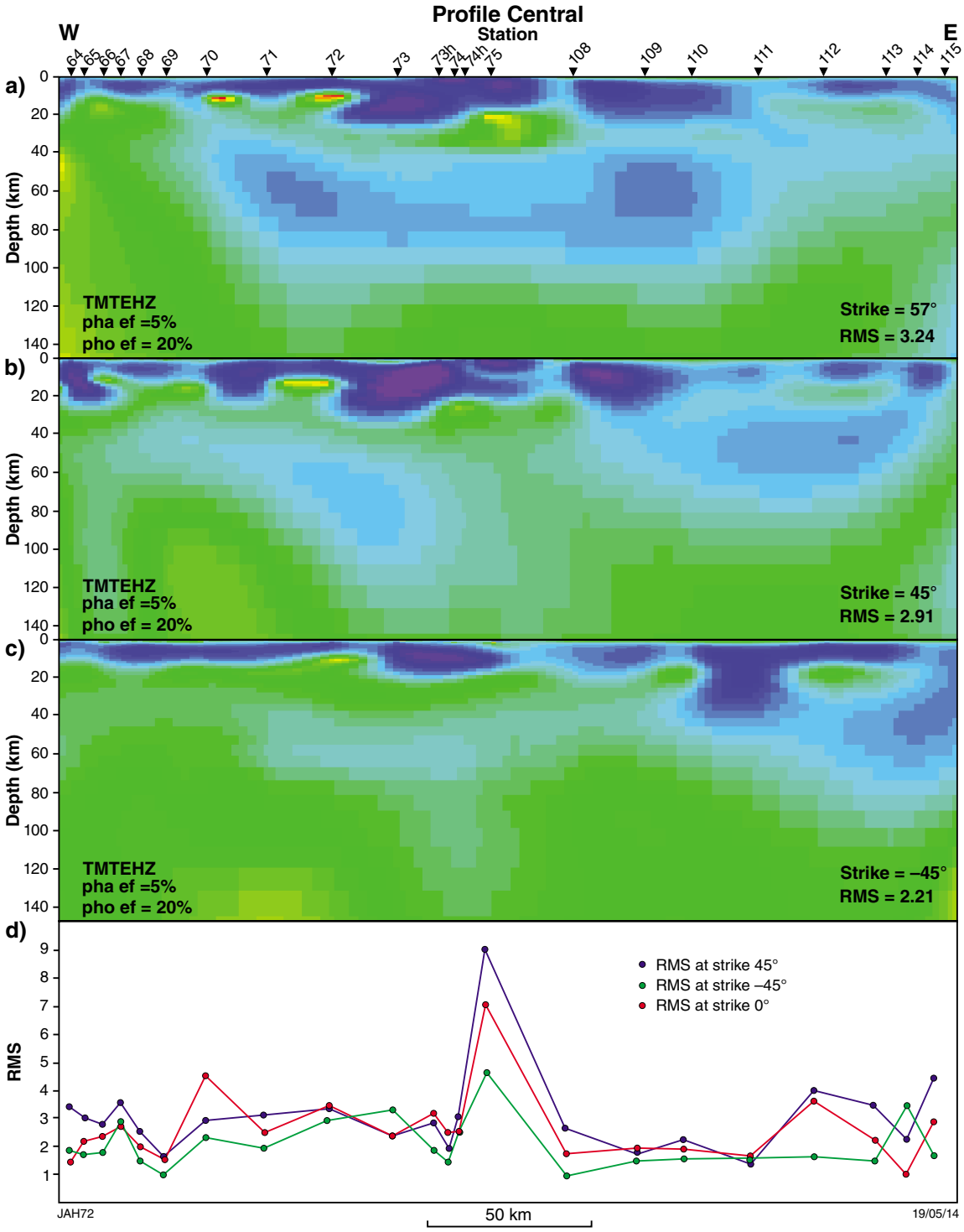

Figure 46. Results of 2D modelling along Profile Central using all data not deemed exceptionally noisy with the data rotated to a geoelectric strike angle of: a) 0°; b) 45°; c) –45°; d) RMS misfit value for each site along the profile for each model. See Figure 1 for the locations of the profiles.

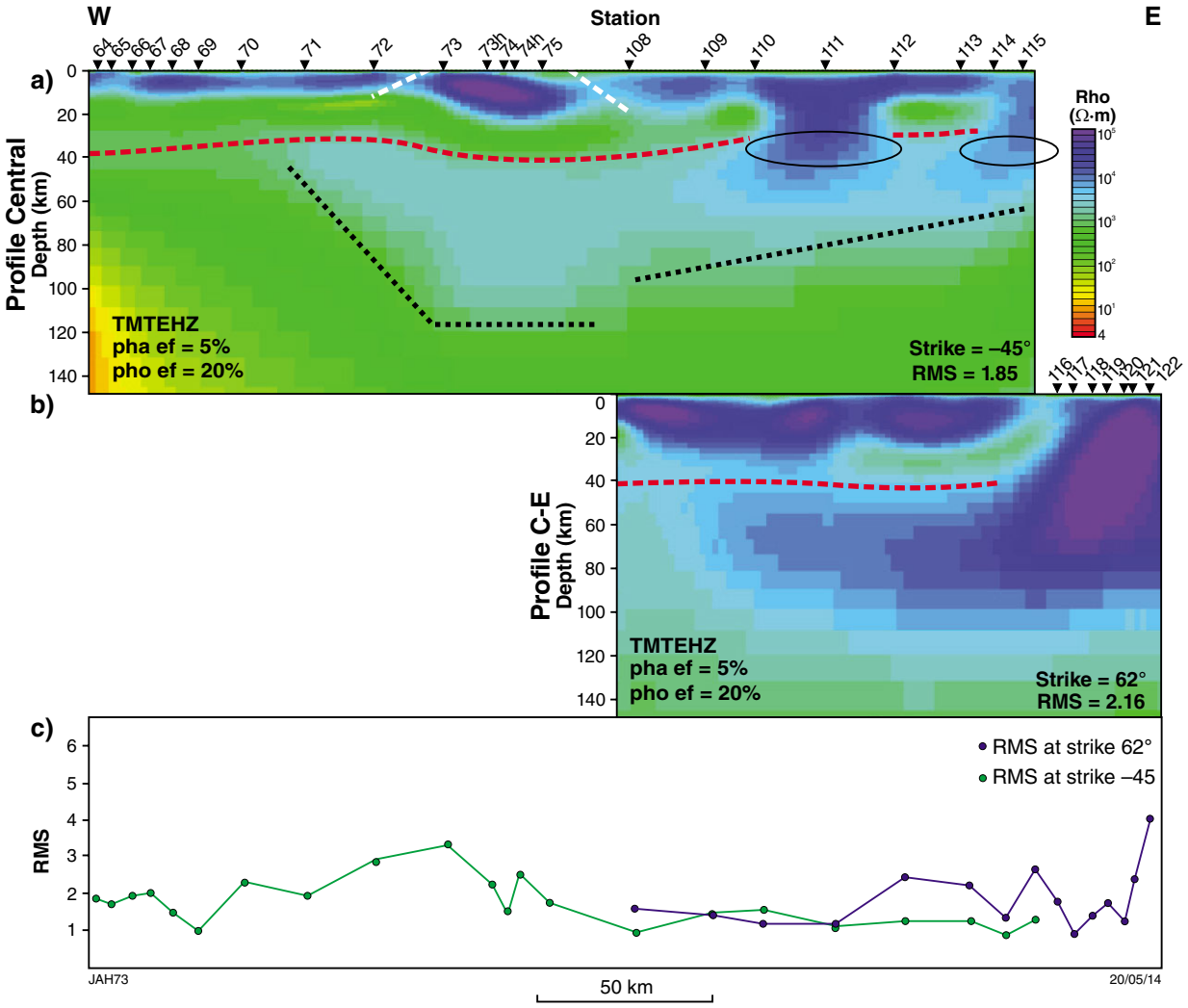

Figure 47. The preferred 2D model along Profile Central and Profile C-E and the RMS values for each site along the profile. The warm colours represent areas that are conductive and blue represents resistive. The dashed white lines mark steeply dipping features observed in the upper crust; the black ellipses highlight areas with a resistive lower crust; the red dashed line marks the approximate crust–mantle boundary; and the black dashed lines mark possible variations in the upper mantle. See Figure 1 for the locations of the profiles.

Feature testing (Fig. 48) has been undertaken to assess the lack of a lower crustal conductor beneath site 111 (feature A), the low upper mantle resistivities at the east end of the profile (feature B), and the depth extent of the resistive upper mantle to the west (feature C). Inserting a lower crustal conductive layer beneath site 111 resulted in an RMS value increase from 1.85 to 1.98. After 100 iterations with feature A frozen, the RMS value was reduced to 1.86 (a value slightly higher than the original model) and increased resistivity at lower crust depths was observed to the west of the frozen region (Fig. 48b). Unfrozen, feature A reverted to the original preferred model with an even lower RMS value of 1.84 (Fig. 48c). These results indicate that the lower crust in the section is resistive and that the lower crustal conductor is discontinuous along the profile. Feature B was tested by inserting a resistive block between 60 and 120 km beneath the western part of the profile. Forward modelling produced a small increase in the overall RMS value to 1.89 suggesting that the data are sensitive to the structure at these depths. Subsequent inversions for both a frozen and unfrozen block resulted in lowered RMS values; however, the shape and location of the enhanced conductivity zone, even for the unfrozen iterations, differs from the preferred model (Fig. 48d,e). This suggests that lateral changes in the mantle exist, but that the specific locations and orientations of these changes are still unresolved. Inserting a resistive block in the upper mantle at the east end of the profile (feature C) also saw a small increase in RMS to 1.89. Models with feature C frozen and unfrozen both obtained low RMS values and the unfrozen model, although slightly less resistive, retained a westward dipping resistive unit with an RMS value of 1.84 (Fig. 48f,g) indicating that the data along Profile Central may not be sensitive to this feature. Note that feature C lies at the edge of the profile. MT sites sample larger areas with greater depths meaning that sites farther to the east may be able to help resolve the structure in the vicinity of feature C.

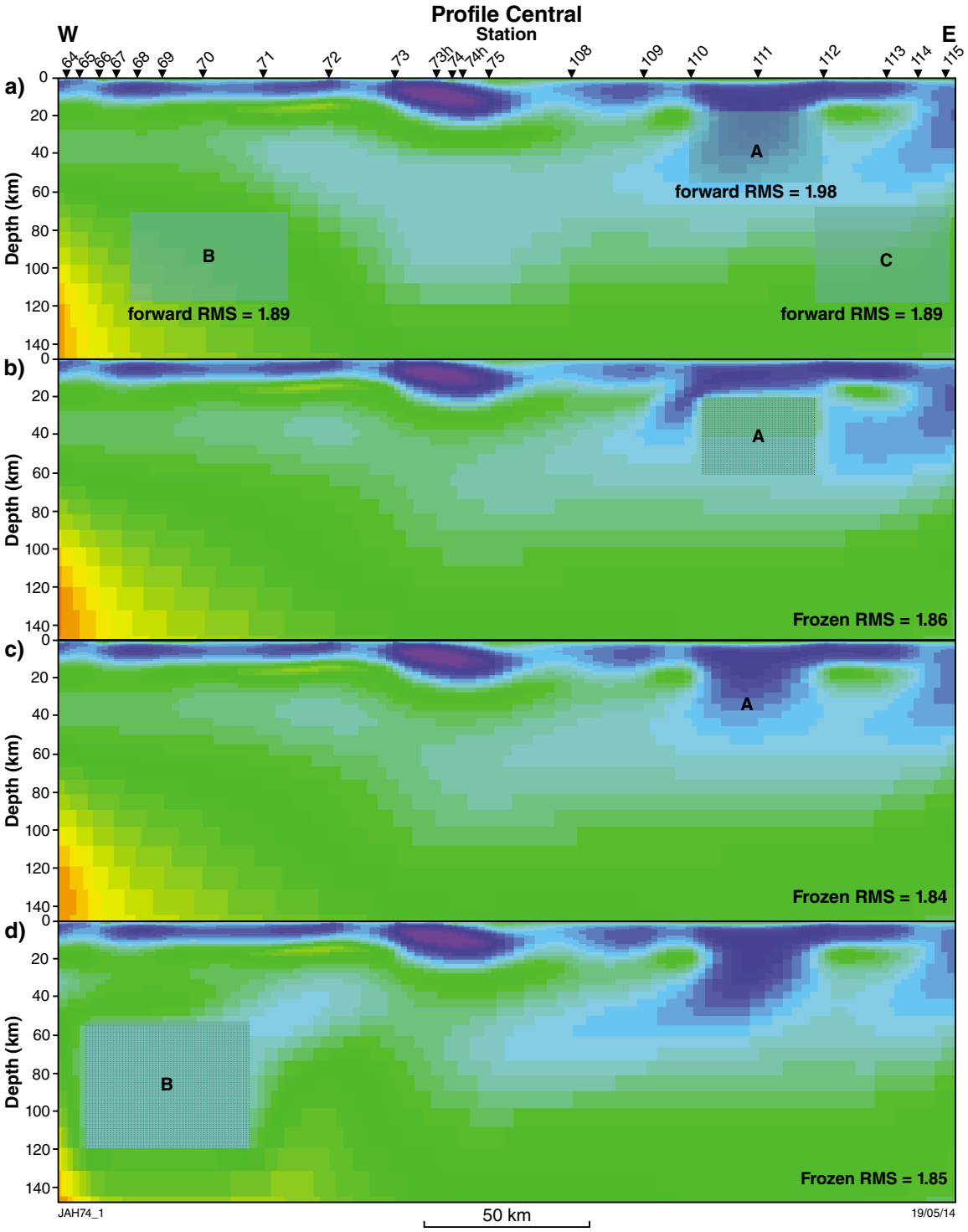

Figure 48. **Assessment of the reliability of features with anomalous electrical properties in the preferred resistivity cross-section along Profile Central: a) shows the lettered features that are altered and the resulting RMS values after forward modelling; b) new model with feature A frozen; c) new model with feature A unfrozen; d) new model with feature B frozen; e) new model with feature B unfrozen; f) new model with feature C frozen; g) new model with feature C unfrozen**

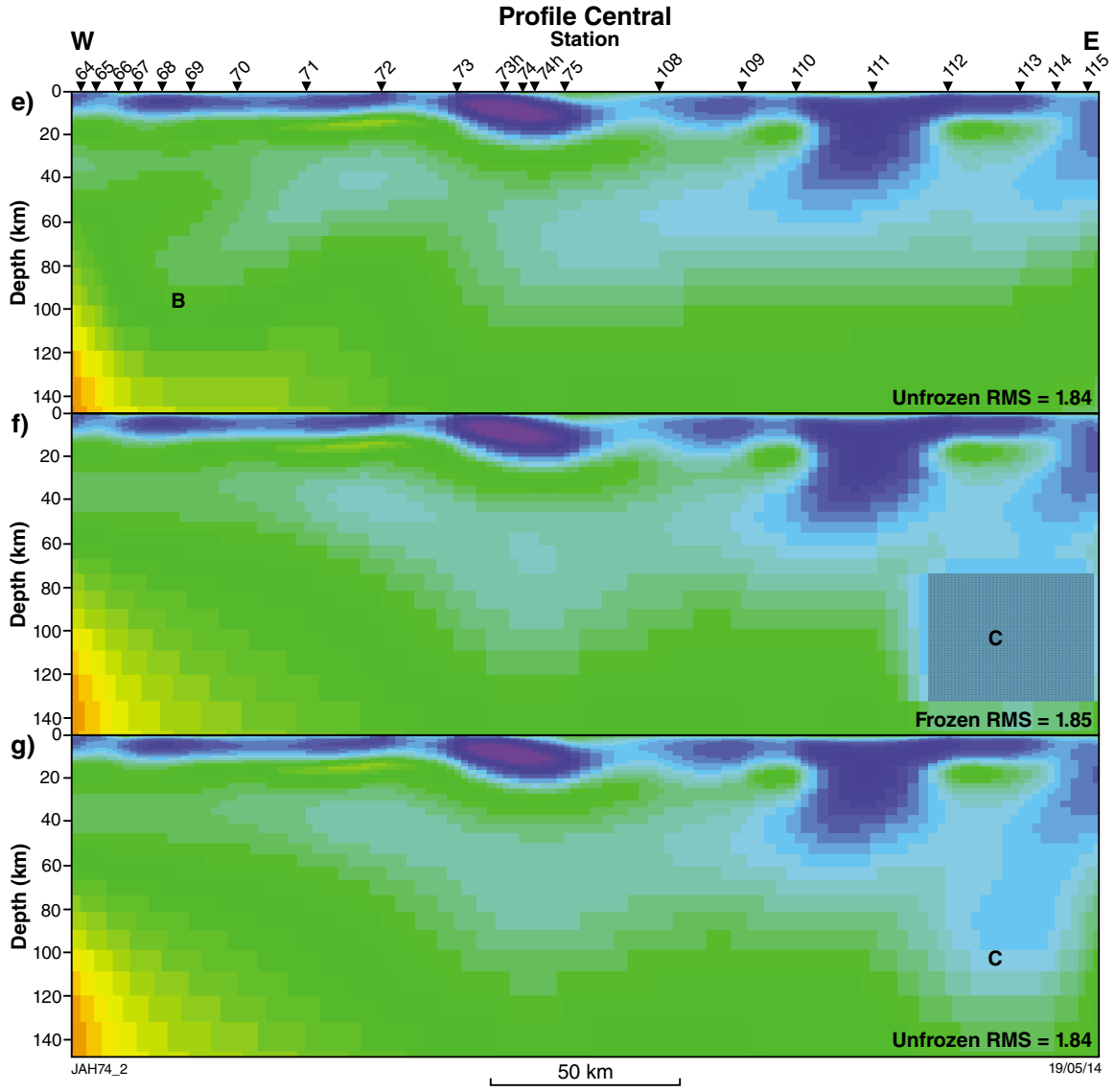

Figure 48. continued

Profile East

Results of 2D modelling using all of the data acquired along Profile East are shown in Figure 49. There is little difference in the overall RMS value or conductivity structure revealed between the models inverted at a strike angle of 62° and those at a strike angle of 38° (c.f Profile C-E). The data at all sites were deemed to have 3D effects at periods greater than 10 to 30 s. The resulting models using data edited for high-skew values, therefore, show little to no structure in the deep mantle lithosphere. Our preferred model along Profile East (Fig. 50) was generated at a strike of 38°, using data from the TE-mode, TM-mode, and Tipper with an error floor of 5% on the phase, 20% on apparent resistivity, and 0.02 absolute value on tipper.

The model reveals a thin layer (<5 km thick) with moderate conductivities (about 500 Ω•m) along the surface of the western half of the profile (probably the Kimberley Basin) that overlies a resistive crust to about 20 km. The resistive crust is underlain by a conductive lower crust with a transition to a more resistive upper mantle at 3–40 km depth. Shallow high conductivities (<10 Ω•m) imaged beneath sites 148–155 are likely due to pyritic black shales within the Mesoproterozoic Carr Boyd Group that unconformably overlies the Kimberley Group and Lamboo Province. A northwestward-dipping resistive wedge (>60 000 Ω•m) is imaged along the eastern margin of the Kimberley Craton, which extends to at least 80 km in depth. This may represent a remnant of subducted crustal material (see Interpretations and discussion). East of the resistive zone, the resistivity decreases significantly to <500 Ω•m. Even further east the values increase again to those more consistent with average mantle conductivities (about 10 000 Ω•m).

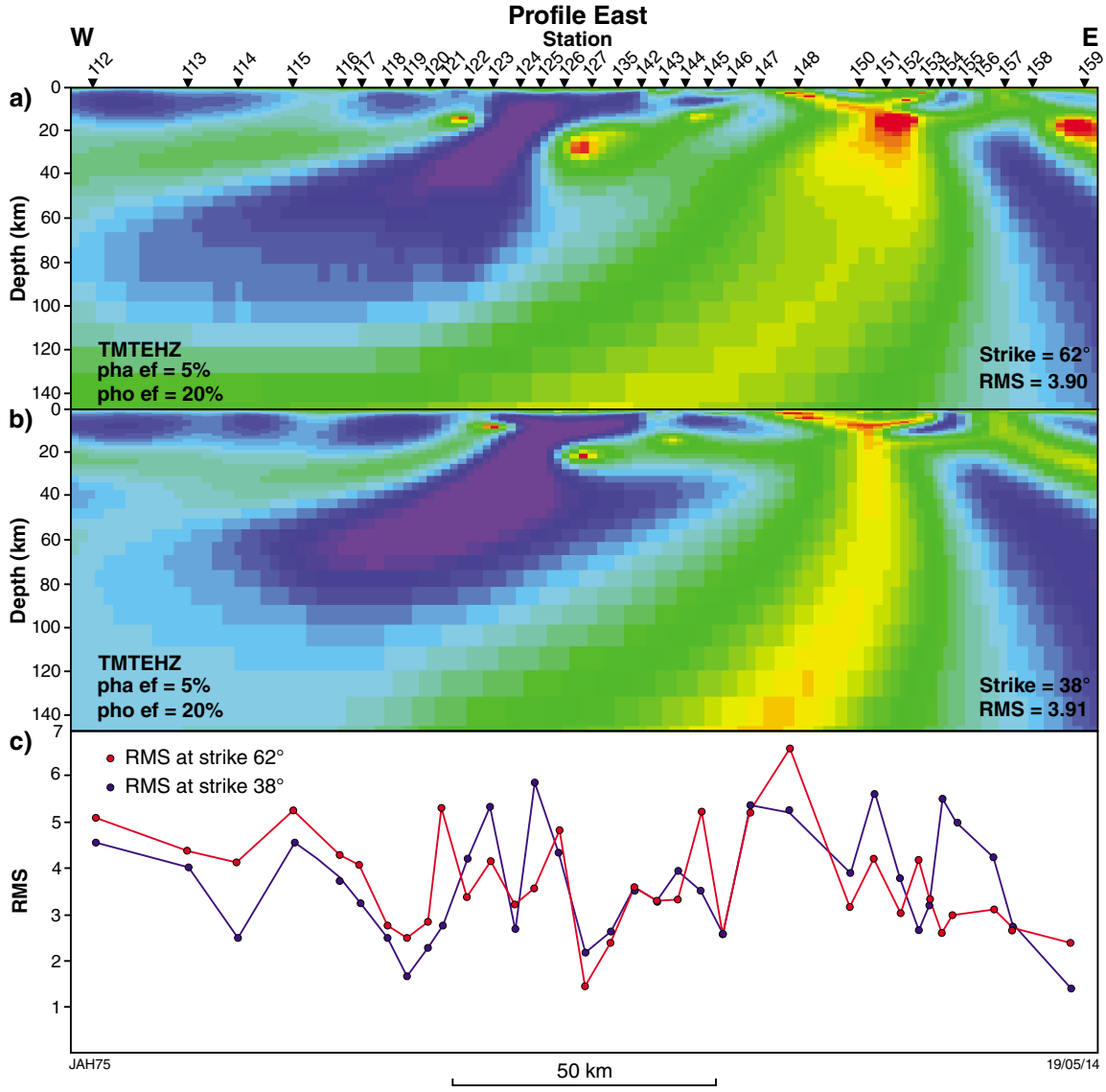

Figure 49. Results of 2D modelling along Profile East using all data not deemed exceptionally noisy with the data rotated to a geoelectric strike angle of: a) 62°; b) 38°; c) RMS misfit value for each site along the profile for each model. See Figure 1 for the locations of the profiles.

Several features have been tested to ascertain whether they are robust and required by the data (Fig. 51). Features A and B are anomalously high conductivities in the mid- and lower-crust. Features C, D, and E test the lateral variations in the upper mantle. A resistive block was inserted into the preferred model at upper-mid crustal depths beneath sites 115–124. The overall RMS value increased significantly with forward modelling and subsequent inversions were not able to reduce the RMS to its original value with the altered area, frozen or unfrozen, indicating that the conductive middle crust is a robust feature of the preferred model (Fig. 51b,c). Adding a resistive block in the lower crust beneath sites 145–150 (feature B) showed no change to the RMS value with forward modelling or further iterations indicating that the data are not sensitive to the crustal structure beneath the near-surface high conductivities (Figures 51d and e).

Features C, D, and E model alterations, testing the sensitivity of the data to the upper mantle structure, resulted in minimal increases in the overall RMS value after forward modelling. Both frozen and unfrozen inversions of the altered model resulted in an RMS value that was equal to or below the original value (Fig. 51f–k). Unfrozen, feature C reverted back to the structure revealed in the preferred model; however, features D and E did not. This suggests that the northwestward-dipping resistive wedge is a reliable feature, but that the data do not penetrate to the deep mantle.

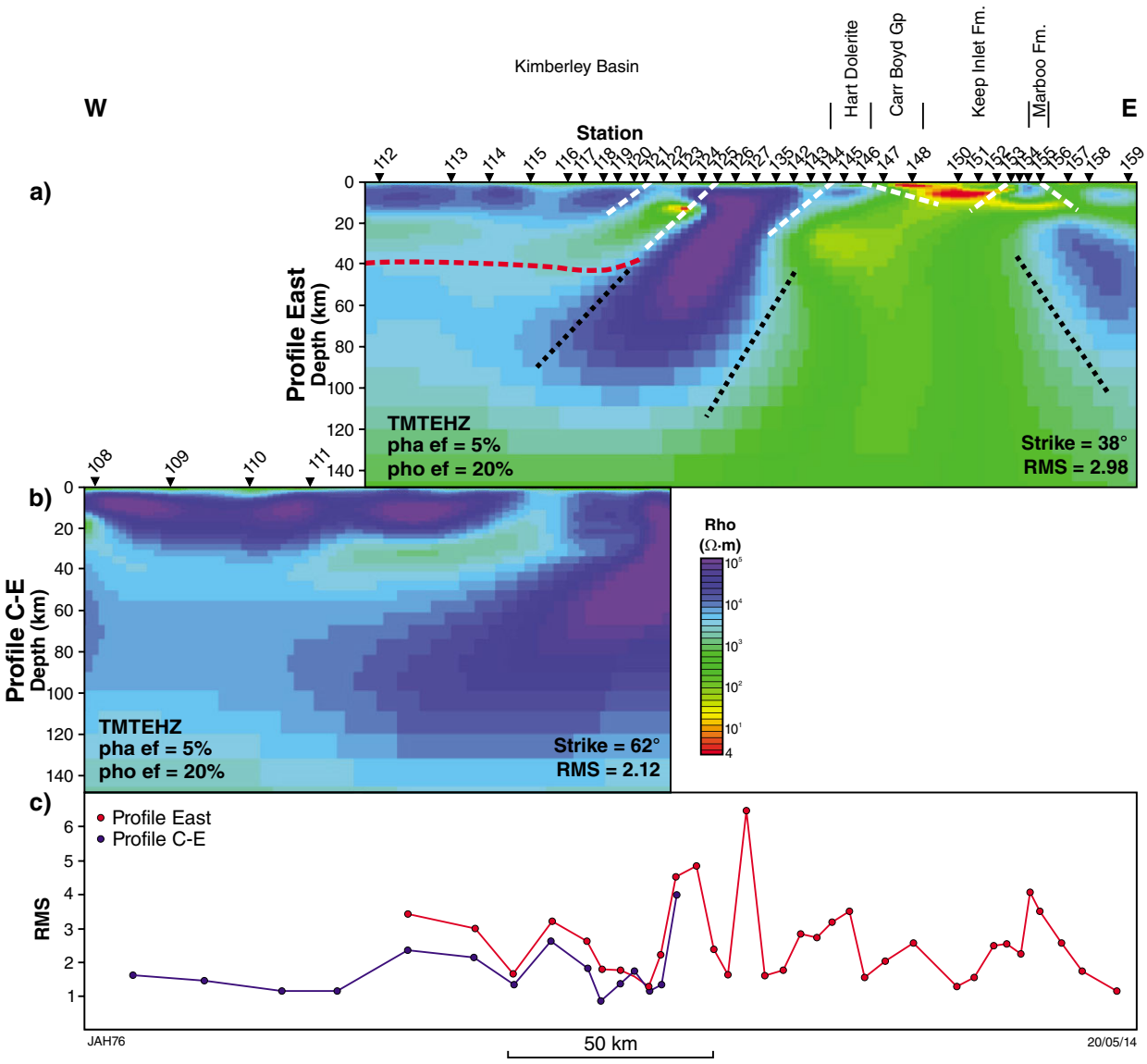

Figure 50. The preferred 2D model along Profile East and Profile C-E and the RMS values for each site along the profile. The warm colours represent areas that are conductive and blue represents resistive. The dashed white lines mark steeply dipping features observed in the upper crust; the red dashed line marks the approximate crust–mantle boundary; and the black dashed lines mark possible variations in the upper mantle. See Figure 1 for the locations of the profiles.

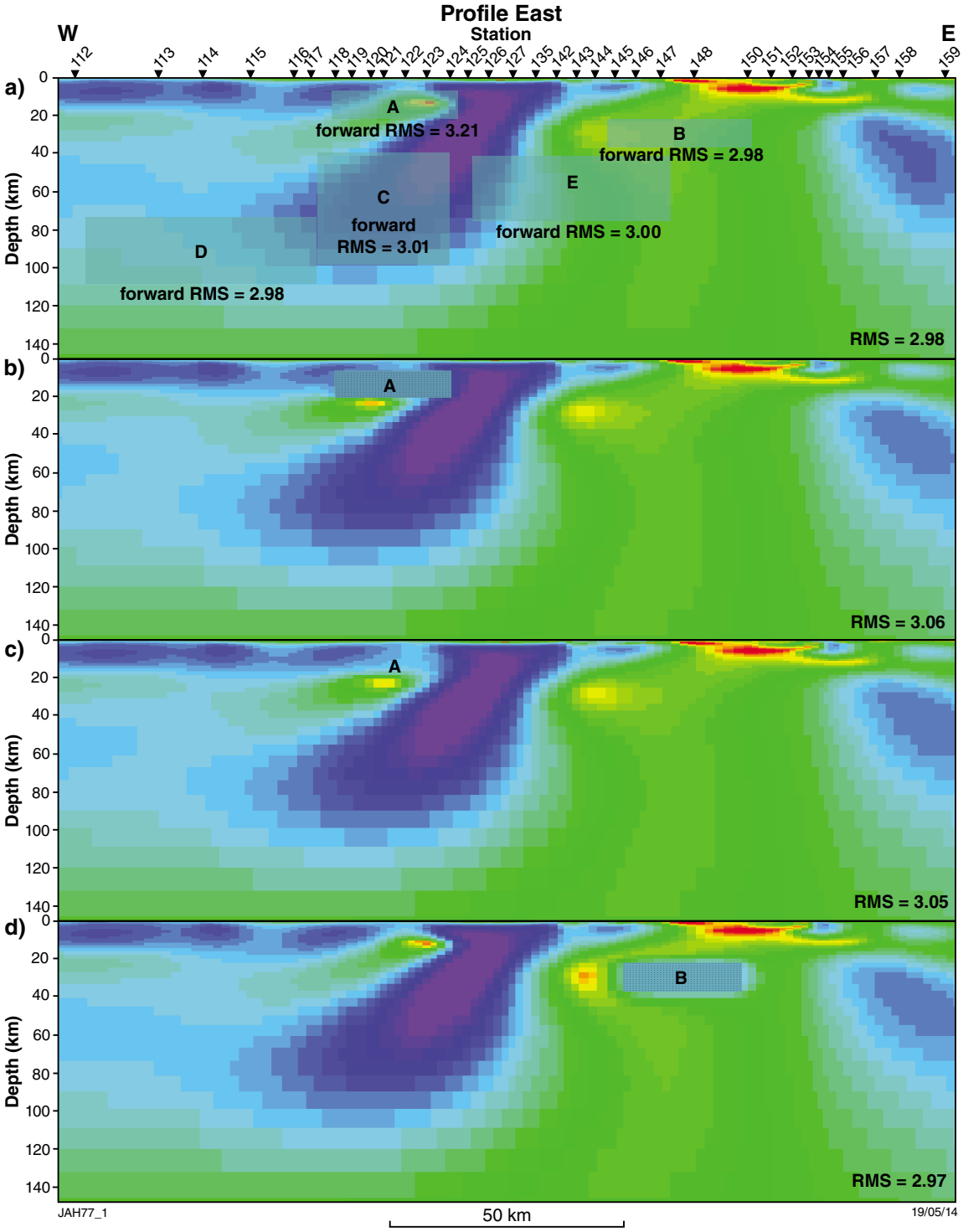

Figure 51. **Assessment of the reliability of features with anomalous electrical properties in the preferred resistivity cross-section along Profile East; a) shows the lettered features that are altered and the resulting RMS values after forward modelling; b) new model with feature A frozen; c) new model with feature A unfrozen; d) new model with feature B frozen; e) new model with feature B unfrozen; f) new model with feature C frozen; g) new model with feature C unfrozen; h) new model with feature D frozen; i) new model with feature D unfrozen; j) new model with feature E frozen; k) new model with feature E unfrozen**

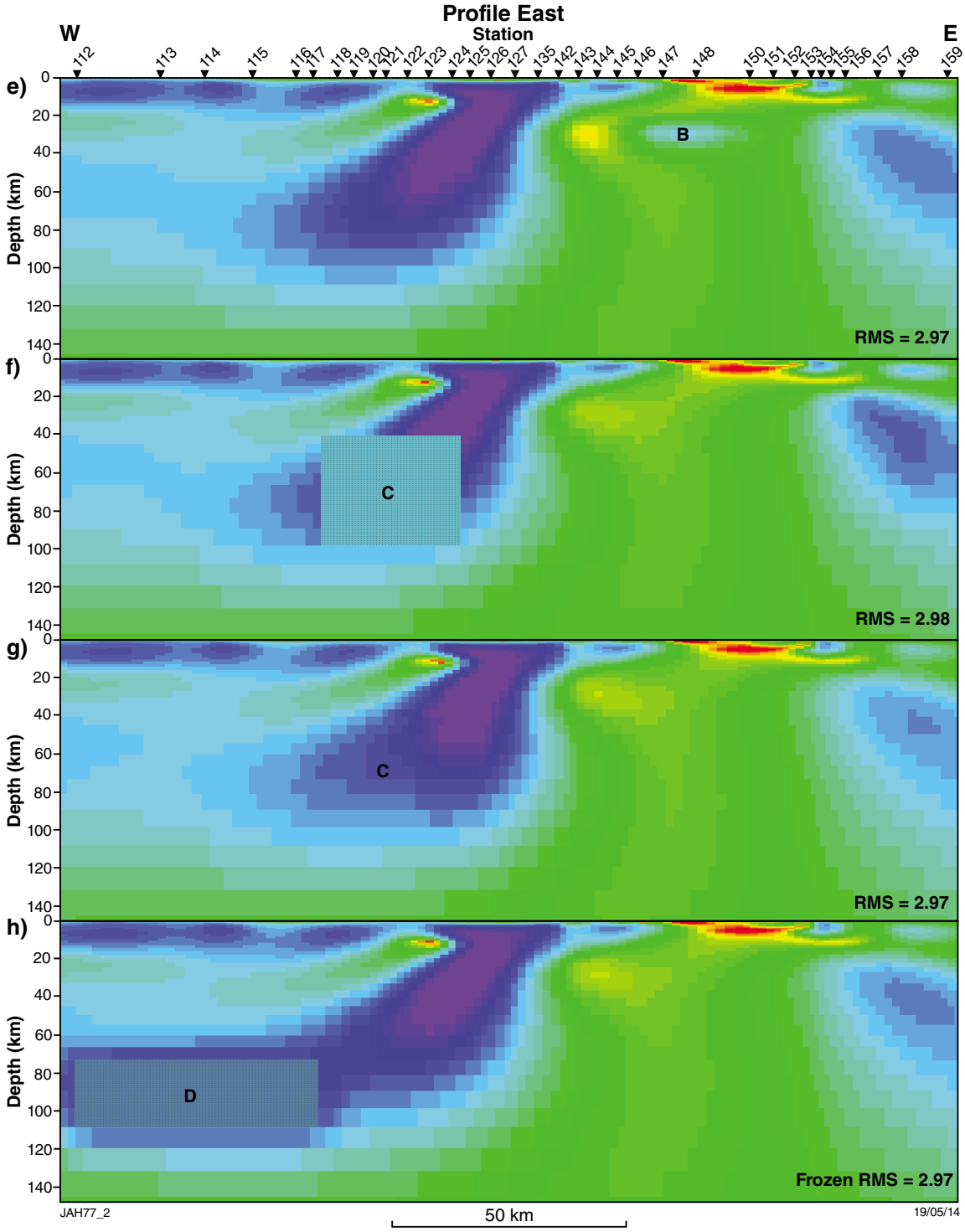

Figure 51. continued

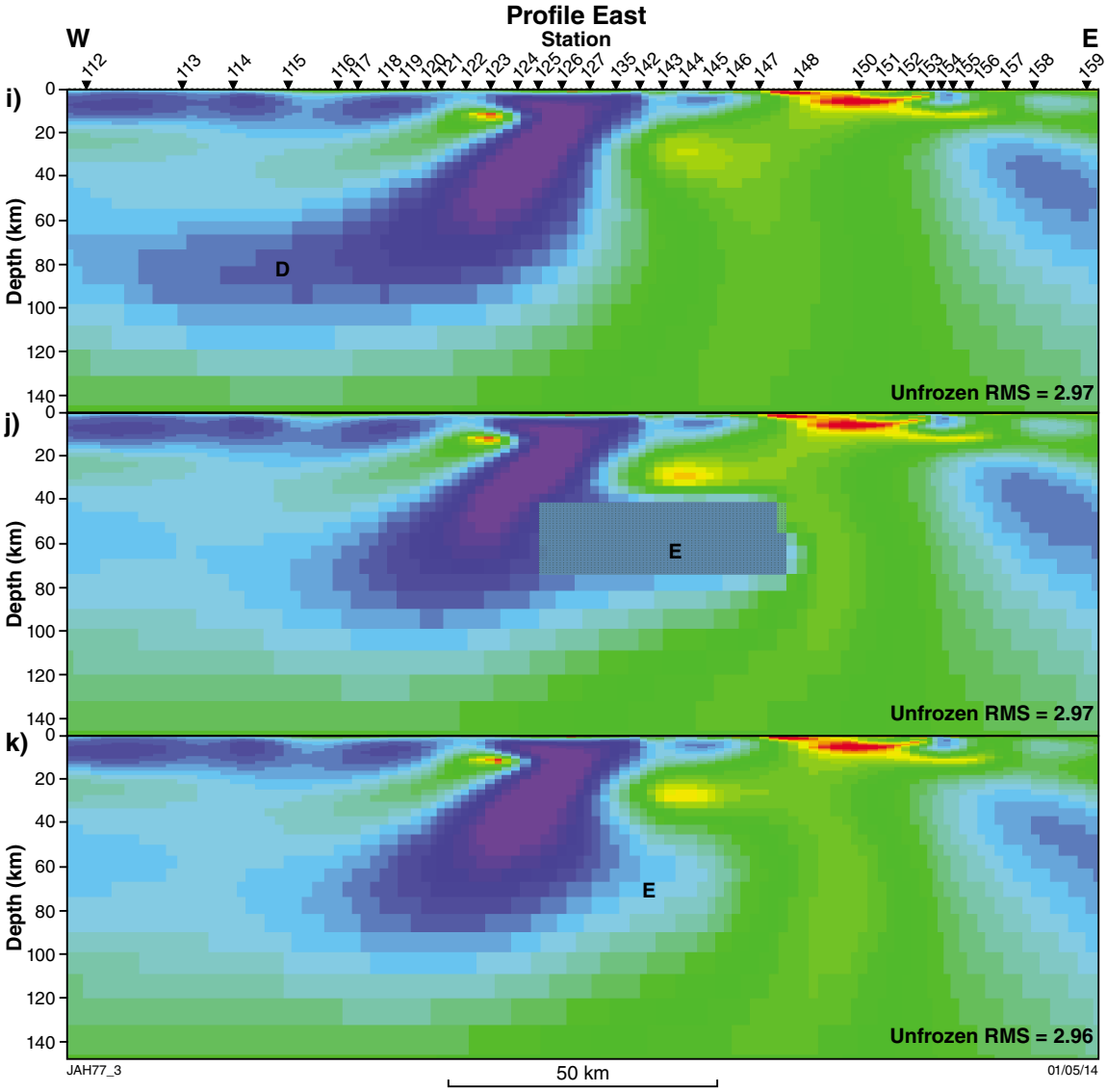

Figure 51. continued

Profile West

Results of 2D modelling along Profile West using all of the data not deemed excessively noisy are shown in Figure 52. Inversions with data at a strike angle of 0° resulted in a high degree of variability in the conductivity structure when different modelling parameters and components were applied (Fig. 52a). A smoother model and lower overall RMS value were attained using data at a strike of –52° (Fig. 52b). RMS values plotted for each site show that a strike of –52° is preferred along the whole profile (Fig. 52c).

The preferred model along Profile West reveals near-surface high conductivities (<10 Ω•m) west of site 20 to at least 5 km depth, likely to be caused by conductive sedimentary units in the Canning Basin (Fig. 53). East of site 46, there is a thin moderately conductive (about 500 Ω•m) layer to <5 km, which is probably the Kimberley Basin. East of site 21, high resistivities (>10 000 Ω•m) are observed, ranging in a thickness 10–35 km and are cut by commonly steeply dipping, less resistive (1000–5000 Ω•m) features that extend from the surface to lower crustal depths. These features, some of which coincide with fault traces or folds at the surface (white dashed lines in Fig. 53), probably represent the subsurface expression of faults that either cut through resistive crust, or mark the boundary between different crustal units. In general, the high resistivities are underlain by a less resistive lower crust (about 500 Ω•m) to depths of 35–40 km, consistent with estimates of crustal thicknesses. The central portion of the profile is an exception, where high resistivities are observed through to the lower crust beneath sites 46–53. The western end of the profile reveals anomalously low resistivities imaged both at crustal depths and through the upper mantle. The near-surface high conductivities may be masking the conductivity structure and depth and sensitivity analysis needs to be undertaken to ascertain its validity. Upper mantle resistivity is shown to be about 6000 Ω•m beneath the central portion of the profile, with an increase beneath the eastern part of the

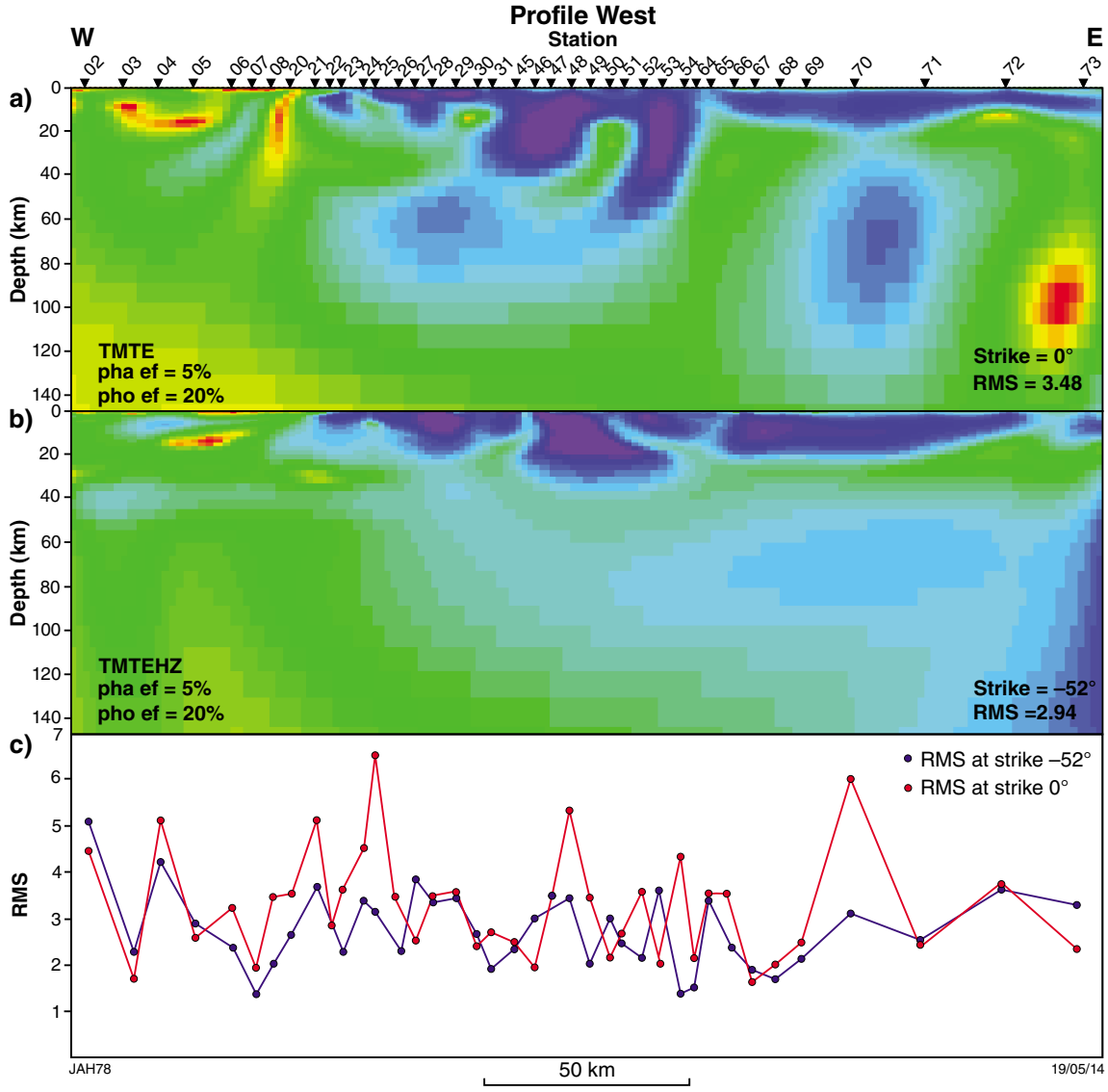

Figure 52. Results of 2D modelling along Profile West using all data not deemed exceptionally noisy with the data rotated to a geoelectric strike angle of: a) 0°; b) –52°; c) the RMS misfit value for each site along the profile for each model. See Figure 1 for the locations of the profiles.

profile to values of >20 000 Ω•m. This increase from west to east at mantle depths differs significantly from models generated at a strike of 0° and is inconsistent with results along Profile Central. Prior to inversion, much of the long period data at sites 70–73 were removed due to poor data quality or 3D effects (Fig. 35), and the data at the east of the profile may not be sensitive to the deep structure.

Feature testing was undertaken on features marked A–F in Figure 54a. Feature A is a resistive block that does not appear to be underlain by a conductive lower crust. The depth of this resistor is tested, as well as the conductivity value of the underlying layer by altering the preferred model to have a continuous lower crustal conductive layer east of site 26. Forward modelling of the altered model saw a large increase in overall RMS value from 2.66 to 3.07. After 100 iterations with feature A frozen, the RMS did not reduce to its original value and the lower crust to the west of the frozen area was imaged as resistive (Fig. 54b). Unfrozen, the model reverted to its original structure and RMS value indicating that the resistive lower crust is required by the data (Fig. 54c).

Features B, C, and D are dipping conductive zones within the upper crust. A resistive block consistent with regional upper crustal values was inserted between 5 and 20 km beneath sites 24–28 (feature B) and the RMS increased to 2.84 after forward modelling. Further inversions with feature B frozen resulted in an increase in the conductivity value of the lower crust beneath the frozen resistive block and a decrease in conductivity to the west of the block with an RMS of 2.68. Resistive blocks were inserted over near-vertical conductive structures cutting through the resistive upper crust (features C and D). The small increase in RMS value is expected as alterations to the shallow structure would be detected by only a few sites.

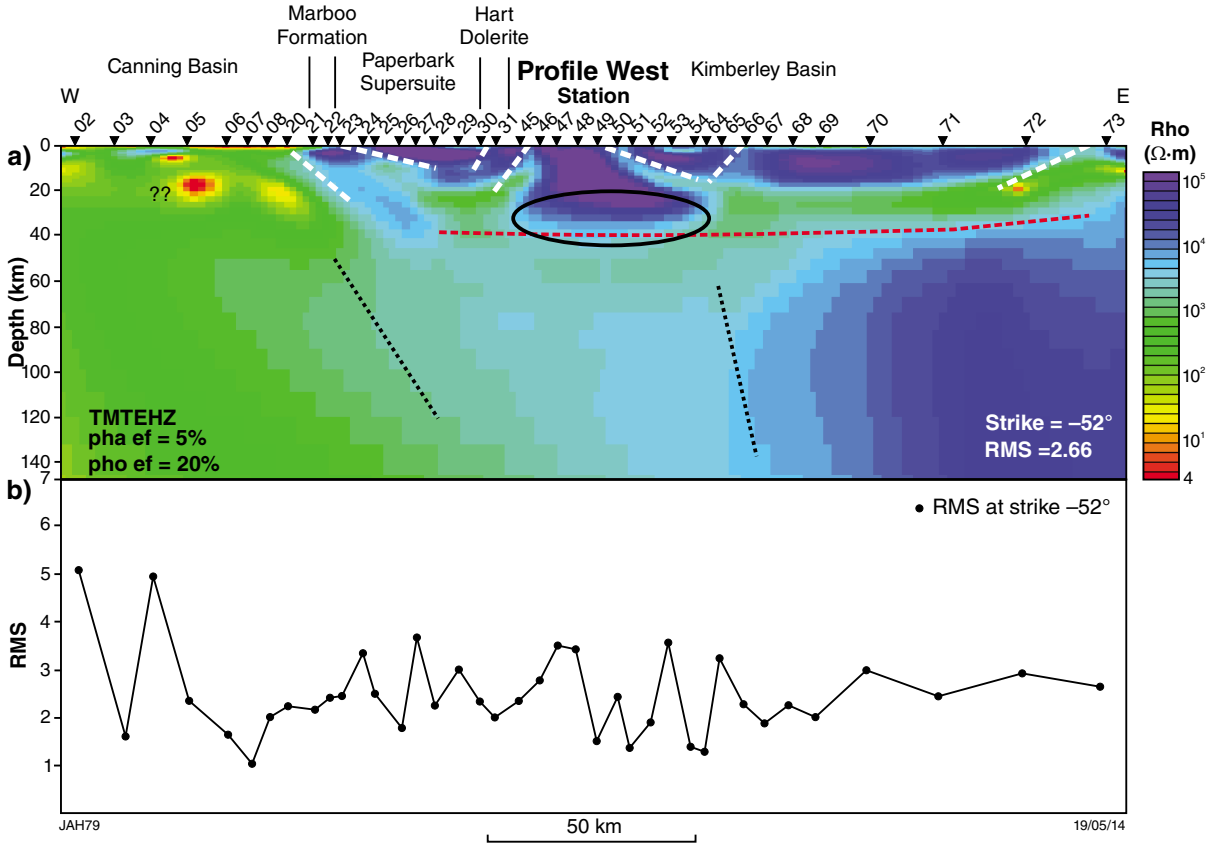

Figure 53. The preferred 2D model along Profile West and the RMS values for each site along the profile. The warm colours represent areas that are conductive and blue represents resistive. The dashed white lines mark steeply dipping features observed in the upper crust; the black ellipse highlights an area of resistive lower crust; the red dashed line marks the approximate crust–mantle boundary; and the black dashed lines mark possible variations in the upper mantle. See Figure 1 for the locations of the profiles.

Inversion with unfrozen areas results in the original conductivity model for features B, C, and D and in each case further inversions resulted in the same or slightly lower RMS as the preferred model (Fig. 54d–i). From the above it is concluded that dipping conductors are generally a reliable aspect of the model.

Features E and F — designed to test the sensitivity of the data to the upper mantle structure — resulted in minimal increases in the overall RMS value after forward modelling. Both frozen and unfrozen inversions of the altered model resulted in an RMS value that was equal to, or below, the original value (Fig. 54j–m). Unfrozen, feature E did not revert back to the original conductivity structure, whereas feature F did. This suggests that the data are not sensitive to the deep structure to the west beneath the near-surface high conductivities. To the east, the data appear to have minimal sensitivity to the deep structure.

Cross profiles

The results of 2D modelling using all of the acquired data at various strike angles for each of the four cross profiles are shown in Figure 55. The lowest RMS value was obtained using a strike of –47° along Profile Cross 1 (Fig. 55a), –20° along Profile Cross 2 (Fig. 55b), 94° along Profile Cross 3 (Fig. 55c), and 60° along Profile Cross 4 (Fig. 55d). For the most part, significant differences are observed for models at different strike angles, meaning the results are largely dependent on the geoelectric strike angle selected for modelling. The preferred models along each cross profile used data that were edited to remove effects of 3D distortion and were generated with an error floor of 20% on the apparent resistivity, 5% on the phase, and 0.02 absolute value on the tipper data (Fig. 56).

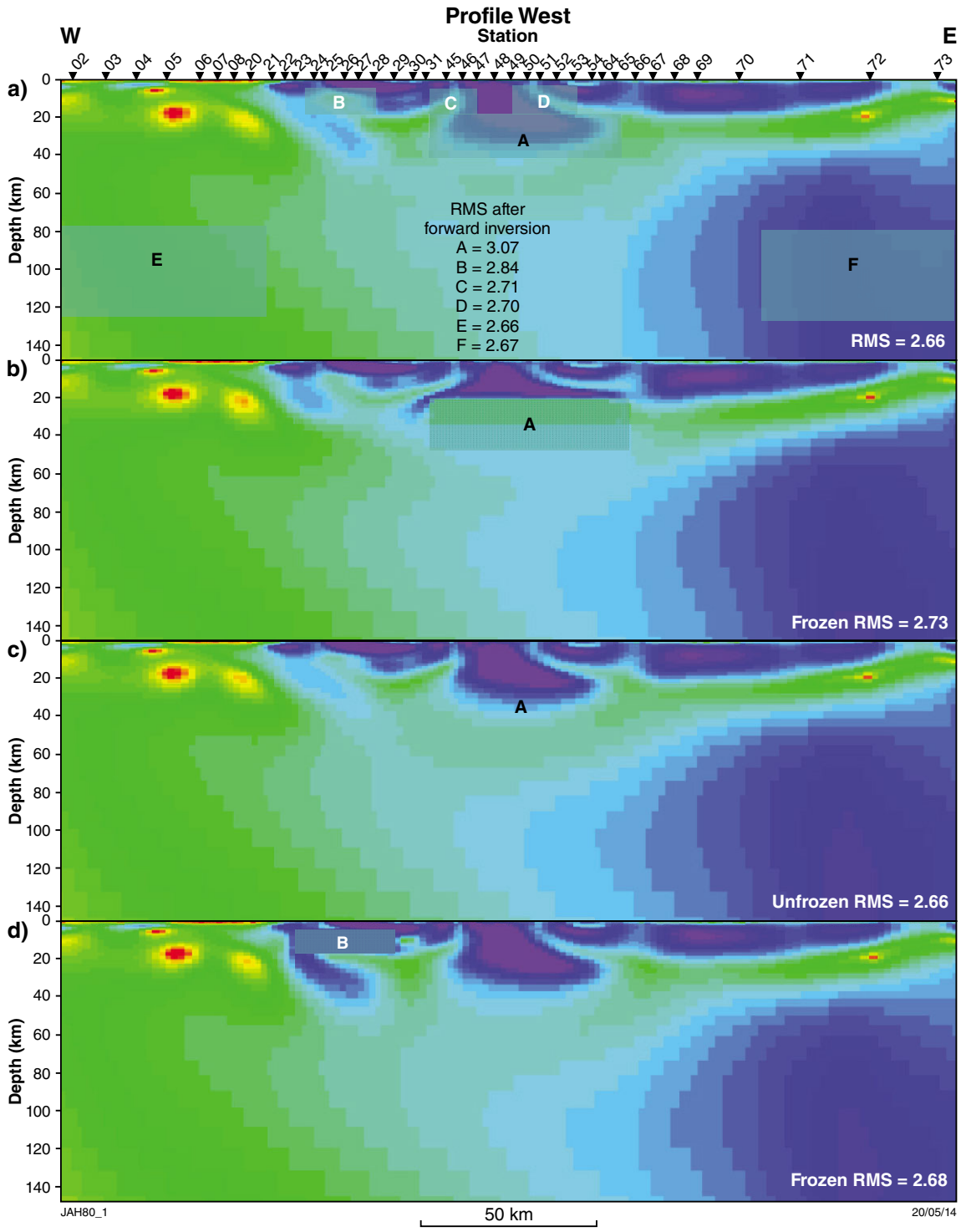

Figure 54. Assessment of the reliability of features with anomalous electrical properties in the preferred resistivity cross-section along Profile West: a) shows the lettered features that are altered and the resulting RMS values after forward modelling; b) new model with feature A frozen; c) new model with feature A unfrozen; d) new model with feature B frozen; e) new model with feature B unfrozen; f) new model with feature C frozen; g) new model with feature C unfrozen; h) new model with feature D frozen; i) new model with feature D unfrozen; j) new model with feature E frozen; k) new model with feature E unfrozen; l) new model with feature F frozen; m) new model with feature F unfrozen

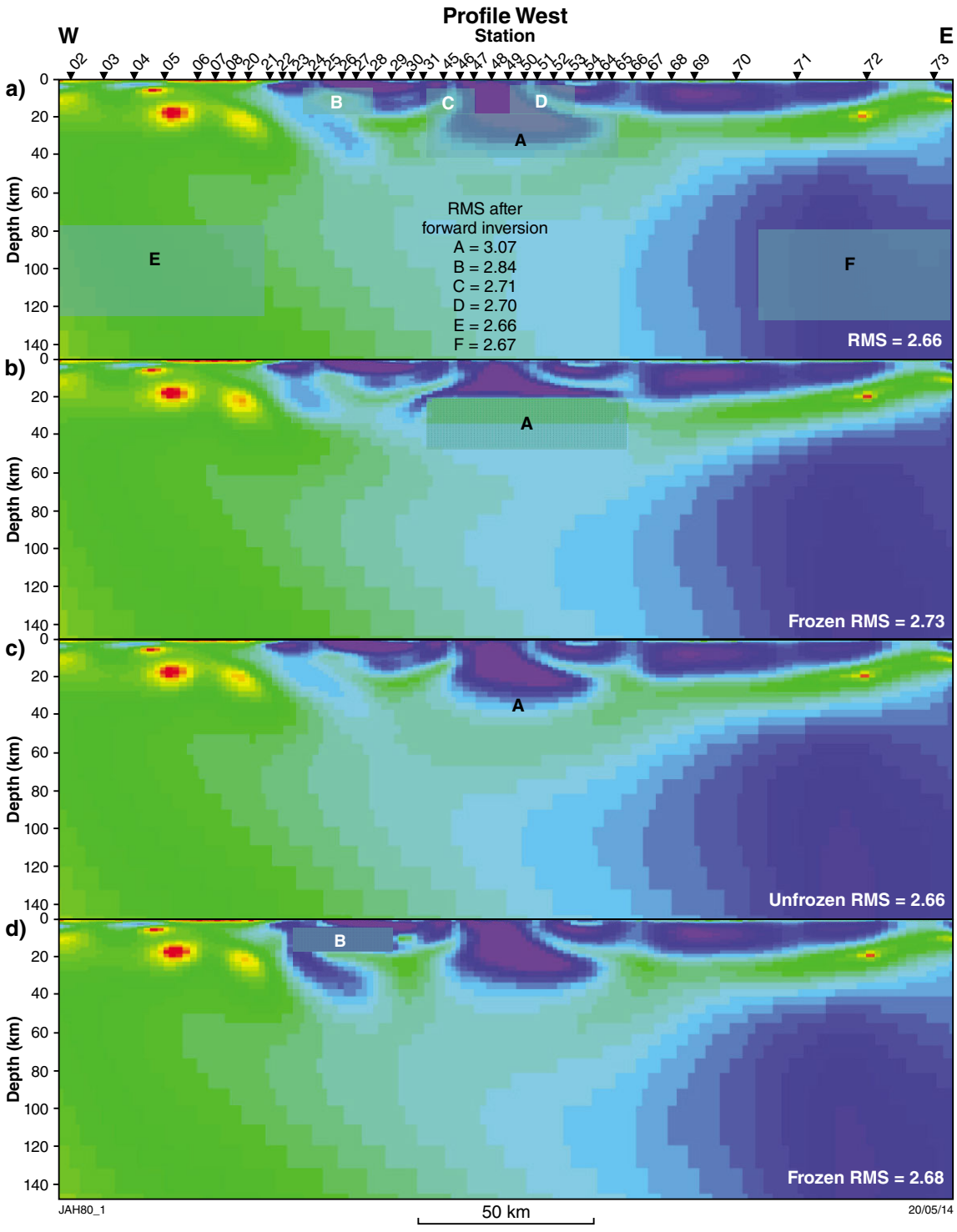

Figure 54. continued

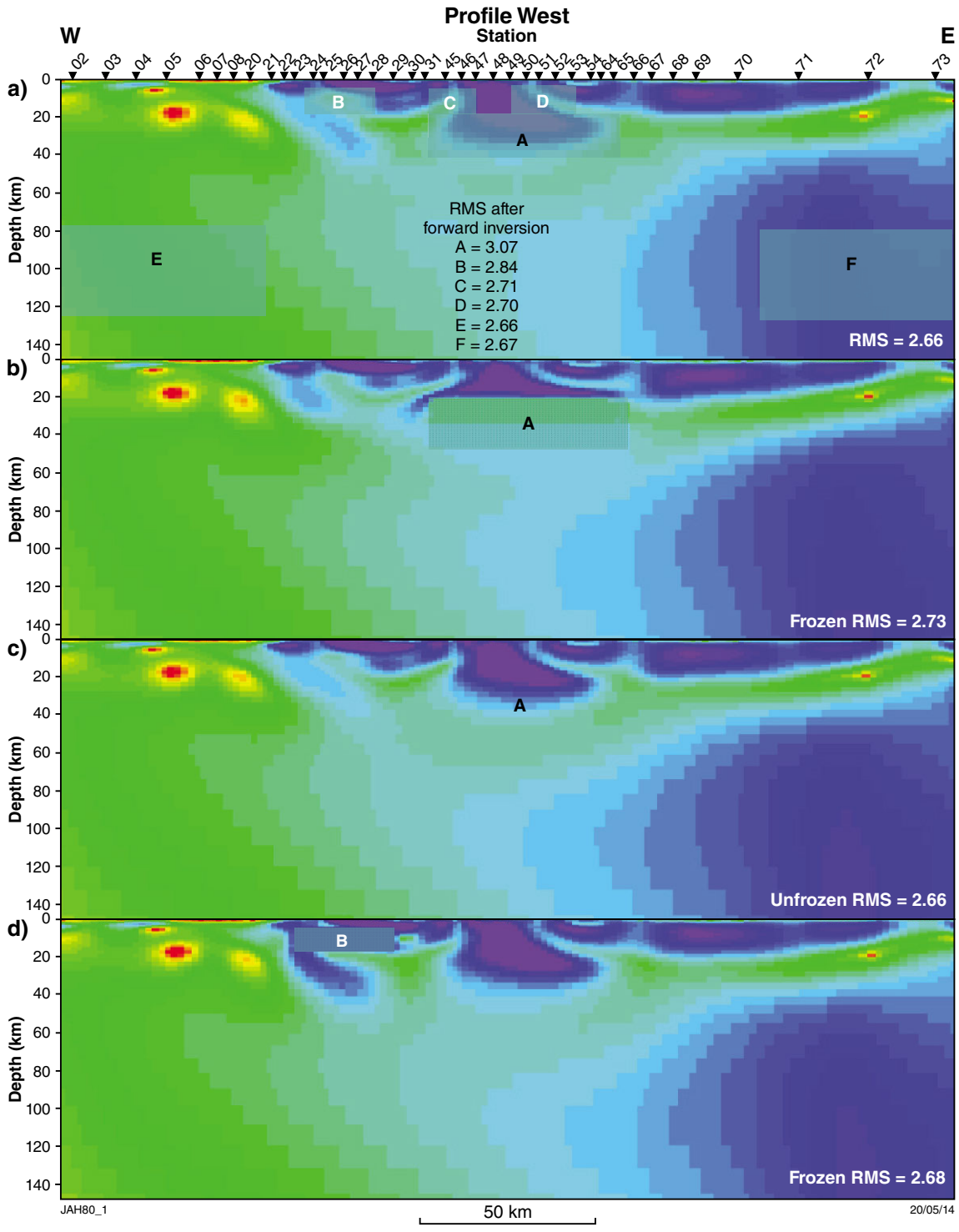

Figure 54. continued

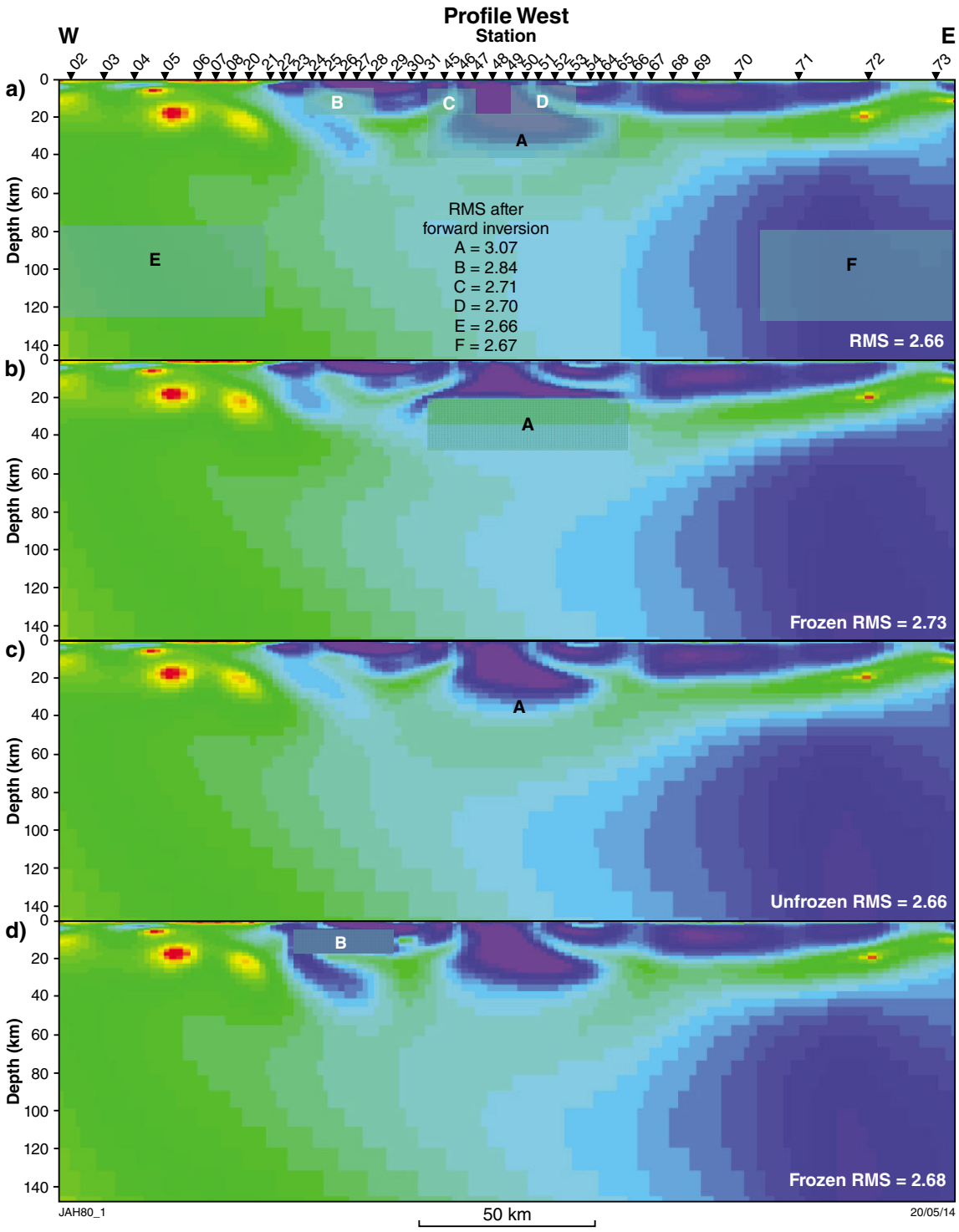

Figure 54. continued

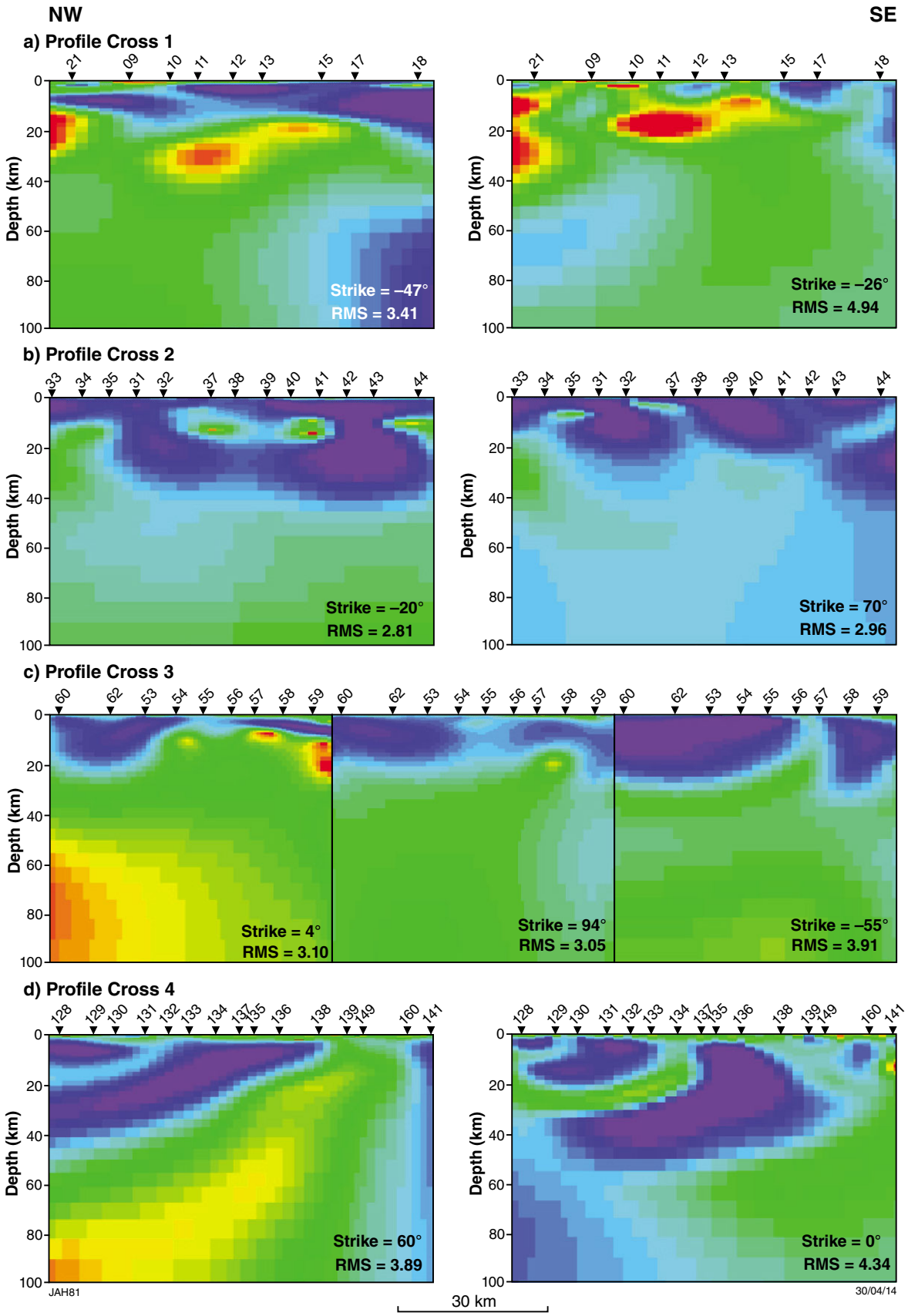

Figure 55. Results of 2D modelling along: a) Profile Cross 1 at strike angles of –47 and –26°; b) Profile Cross 2 at strike angles –20 and 70°; c) Profile Cross 3 at strike angles 4, 94, and –55°; d) Profile Cross 4 at strike angles 60 and 0°. See Figure 1 for the locations of the cross profiles.

Profile Cross 1–3 were designed to test the margins of northeast-trending basement zones inferred by Gunn and Meixner (1998). Although not apparent in strike analysis, these profiles have also been modelled with an assumed geoelectric strike angle of 40° in order to try to delineate these zones (Fig. 56). The preferred models show little structure at depths greater than about 30 km. At a strike of 40°, profiles Cross 1, Cross 2 and Cross 3 reveal northeast-dipping features that extend from the surface to at least 20 km depth and may be related to the structure described by Gunn and Meixner (1998); dashed white lines in Fig. 56a–c. Profile Cross 4 shows a northwest-dipping resistive unit to about 50 km (Fig. 56d) that is consistent with a northwest-dipping resistive unit imaged along Profile East (Fig. 50). The upper and lower bounds of the resistive slab line up with mapped faults at the surface (dashed white lines in Fig. 56d).

Interpretations and discussion

Upper- to mid-crustal structure

The 2D images of electrical conductivity variations reveal the Kimberley Basin sedimentary and volcanic succession as a thin conductive unit (approximately 200–500 Ω•m) with a maximum thickness of 5 km. Beneath the thin conductive layer, the upper crust is predominantly highly resistive (>10 000 Ω•m), consistent with laboratory measurements for crystalline rocks (Fig. 6) and with values observed in stable Archean cratons worldwide. Examples include the Slave Craton in northern Canada (Jones et al., 2003), the Kaapvaal Craton in South Africa (Muller et al., 2009), and the Yilgarn Craton in Western Australia (Dentith et al., 2013). Thus, the data support isotopic and seismic evidence for Archean crust in the Kimberley.

Features revealed in the 2D models at upper- to mid-crustal depths, which are either low resistivity structures that cut through the resistive crust or lateral variations marking the juxtaposition of materials of differing conductivity values, have been plotted over the regional geology map (Fig. 57) as well as the map of basement structure from Gunn and Meixner (1998). The resistive upper crust beneath the Kimberley Basin is cut by several less resistive, steeply dipping zones (thick red lines in Fig. 57), most of which show an excellent correlation with the location of known mafic dykes. These zones are likely to have been emplaced along pre-existing faults. These zones are not conductive, as they are still within the range typical of crystalline rocks, with values greater than 2000 Ω•m, and are visible in the MT data due to the extremely resistive nature of the host rock (Figs 44 and 47). This suggests that the faults are dry with minimal mineralization along the fault plane. The fractures are shown to extend to lower crust depths, and may extend deeper; however, the presence of a lower crustal conductor (described below) masks their response. Similar structures have been observed in the northern Melville Peninsula of the Rae Craton (northern Canada), and were interpreted as faults extending through to the lower crust (Spratt et al., 2013a). It is important to note that, as shown both here and in the data from the Melville Peninsula, the geometry and conductivity of these features in the MT models is highly sensitive to the geoelectric strike angle selected for 2D modelling.

Across the western margin of the Kimberley Basin, there appears to be important along-profile conductivity signatures that define boundaries between different structural blocks (Figs 53 and 57). These include structures that coincide with the location of mapped faults at the surface, bounding to the east and west the deformed boundary to Kimberley Basin and King Leopold Orogen (stations 45–46 and 30–31), the exposed Marboo Formation and the Paperbark Supersuite (stations 21–30) and the northern boundary to the Lennard Shelf (stations 20 and 21). Profiles Cross 1, 2, and 3, were designed to determine if there was a conductivity signature associated with the crustal zones described by Gunn and Meixner (1998). Features in the upper crust are identified in the conductivity models (white lines in Fig. 56, thick red lines in Fig. 57) that correlated closely with the boundary between zones C and B. Several surface mapped faults are not observed in the MT models, either due to a lack of conductivity contrast across the fault or because they are shallow dipping and limited to the upper few kilometres.

The most significant variations observed in the electrical resistivity models occur across the eastern margin of the Kimberley Basin, where a northwest-dipping resistive feature is interpreted as representing ancient subducted crustal material (Fig. 50). This feature extends through the lower crust and into the upper mantle along three separate profiles, and at differing strike angles indicating that the feature is robust (Figs 47, 50, 56). This interpretation is consistent with the current tectonic models for the survey area, which describe the accretion of a crustal fragment at >1900 Ma during west-directed subduction followed by generation of post-collisional granites of the 1865–1850 Ma Paperbark Supersuite in the western zone of the Lamboo Province (Griffin et al., 2000). This interpretation is consistent with the current location of the interpreted remnant slab to the west of the central zone and beneath the western zone, as indicated by the MT data (Fig. 50).

In most cases, MT surveys over modern and ancient subduction zones map zones of enhanced conductivity (Jones et al., 1993). In the case of ancient zones, the most likely cause of the higher conductivities is sedimentary rocks under thrust beneath the overriding plate. This interpretation allows for subduction zones without associated conductive features, e.g. in the instance of a sediment-starved convergent margin.

Although generally present, not all ancient orogenic zones are associated with conductive features and some have shown to preserve resistive features that may be relics of ancient tectonic processes akin to modern subduction and accretion. For example, in the Western Superior Province of central Canada, a steeply north-dipping high-resistivity zone and coincident subvertical high-velocity zone in the subcontinental upper mantle were imaged between two sutures consistent with northward-directed subduction.

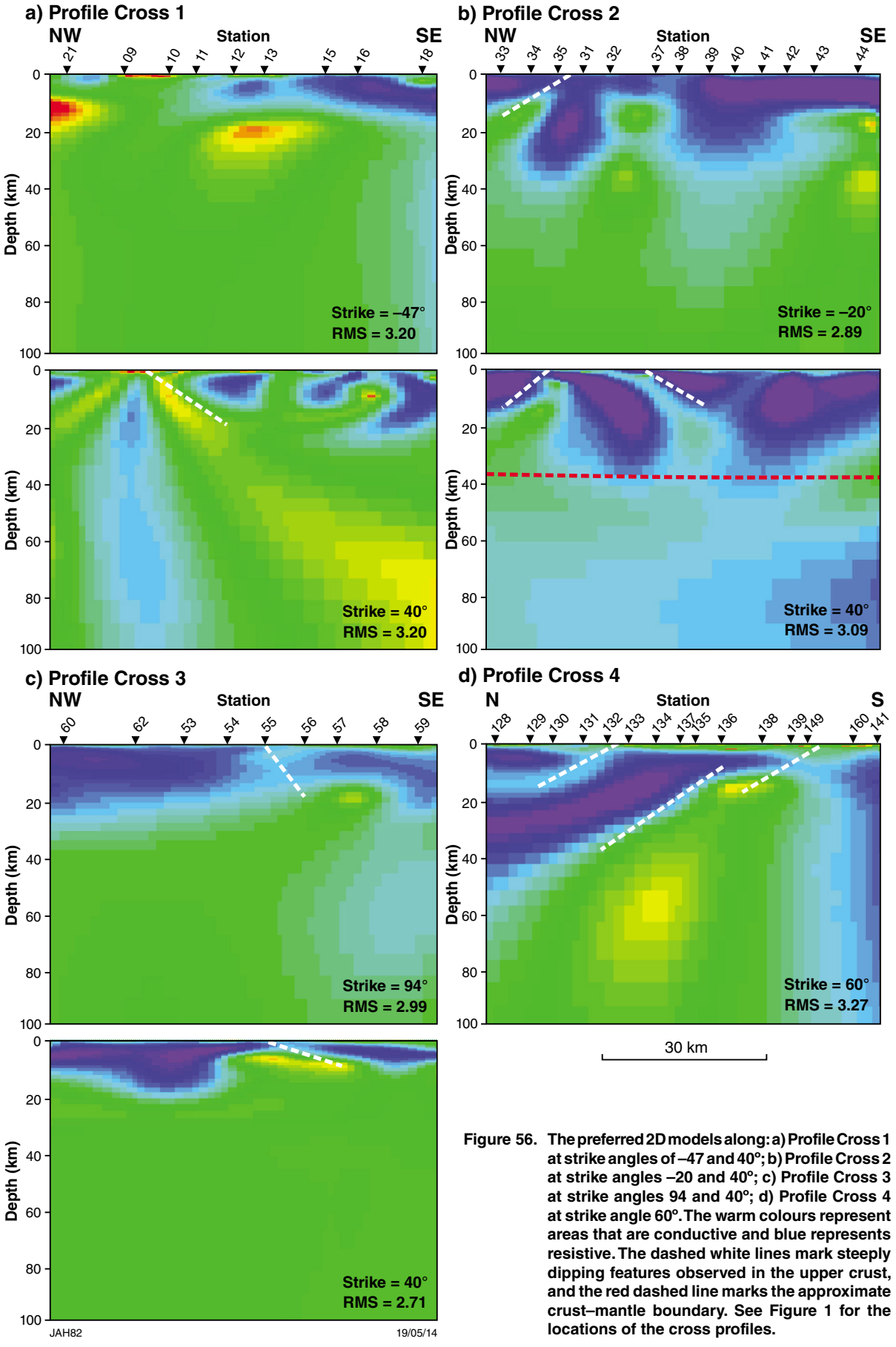

Figure 56. The preferred 2D models along: a) Profile Cross 1 at strike angles of –47 and 40°; b) Profile Cross 2 at strike angles –20 and 40°; c) Profile Cross 3 at strike angles 94 and 40°; d) Profile Cross 4 at strike angle 60°. The warm colours represent areas that are conductive and blue represents resistive. The dashed white lines mark steeply dipping features observed in the upper crust, and the red dashed line marks the approximate crust–mantle boundary. See Figure 1 for the locations of the cross profiles.

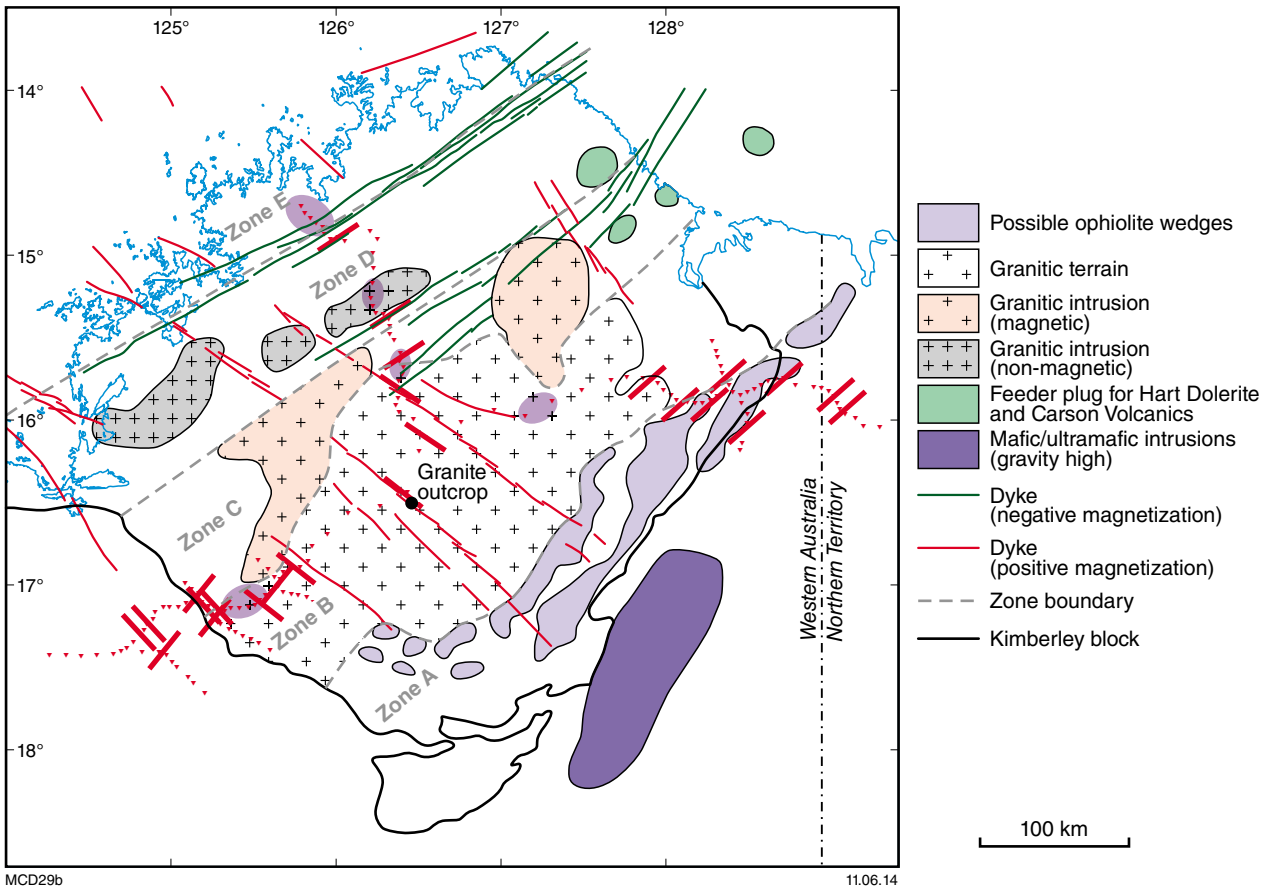

Figure 57. Interpreted basement geology of the Kimberley region from Gunn and Meixner (1998) with selected features identified from the MT data overlain. The thick red lines illustrate the location of steeply dipping structures observed in the upper crust, and the blue ellipses mark areas where a resistive lower crust is imaged.

The low resistivities have been attributed to a steep slab of subducted crustal material emplaced during lateral growth and accretion of the Superior Craton (Craven et al., 2004; Percial et al., 2006; Helmstaedt, 2013). In northeast Brazil, MT data imaged two resistive features dipping from the upper crust into the upper mantle in downward convergence beneath the Borborema Province (Padilha et al., 2014). The observed high-resistivity zones are consistent with a dehydrated oceanic lithosphere depleted of sediments and are interpreted to be related to remnants of former subduction slabs during Neoproterozoic accretion and collision.

Lower crustal conductive layer and the Moho

Each of the conductivity models show that a regional conductive lower crust is present (Figs 44, 47, 53) and the depth to its base is in reasonable agreement with Moho depth estimates of 38–45 km from seismic data (Clitheroe et al., 2000). The base of this conductive layer is also consistent with the shallow 29 km Moho depth near station 120, although it is unclear whether this represents the electrical Moho or the top of the slab. Although the cause of the conductive lower crust in the Kimberley Craton remains uncertain, its presence is consistent with MT studies worldwide that have shown much of the lower continental crust to exhibit relatively uniform enhanced conductivites, typically 10–100 times more conductive than middle- to upper-crustal values (Fig. 6; Jones, 1992; Hyndman et al., 1993). The two most widely supported explanations for the cause of enhanced conductivity in stable continental regions are ionic conduction through interconnected saline pore fluids, and electronic conduction through graphite films or sulfides. Studies are hindered by the need to recreate extreme conditions of temperature and pressure in the laboratory and the impossibility of accounting for the effects of time. An explanation of the reduced resistivity in terms of saline fluids in Archean crust, which is probably present in the Kimberley Craton, is weakened by long resident times and lack of fluid regeneration mechanisms, and the fact that the presence of free water in the deep crust has been

argued against on petrological grounds (Yardley and Valley, 1997). Given the long resident times of potential conductors in Archean crust and a lack of evidence for fluid generation, one interpretation for the enhanced lower crustal conductivity observed in our profiles is the presence of metasedimentary rocks that may contain graphite or sulfides.

The lower crustal conductor beneath the Kimberley region appears to be discontinuous in several locations (blue ovals in Figure 57). A resistive lower crust has been observed in other Archean cratonic settings such as the Slave and Rae Cratons in northern Canada (Jones et al., 2003; Spratt et al., 2013a). MT studies of the western Slave Craton revealed resistivity values of c. 40 000 Ω•m to the base of the crust, and it was suggested that differences in composition or tectonic processes are responsible for the formation of such resistive crust (Jones et al., 2003). It was shown that in the absence of a lower-crustal conductor, a decrease in resistivity to values of c. 4000 Ω•m, is observed at depths consistent with interpretations for the crust–mantle boundary, suggesting that where the lower crust is resistive, the crust–mantle boundary can be observed electrically (Jones and Ferguson, 2001). In the Kimberley region, areas of resistive lower crust (with one exception along Profile East) correlate closely with the crustal block boundaries identified by Gunn and Meixner (1998). This is similar to results of MT studies from the Rae Craton that showed the lower crustal conductive layer to be discontinuous through the Craton and that areas of resistive lower crust may be related to major block boundaries (Spratt et al., 2013b). Alternatively, the high resistivities in the Kimberley Craton may be due to large intrusions, some of the responses correlating with subcircular gravity anomalies.

Mantle structure

The complex tectonic history of the Kimberley region has resulted in a deep structure that is largely 3D. This is evident in the variation in geoelectric strike direction from east to west in the MT data set and in the high skew values observed at long periods. 2D models of the deep structure are, therefore, unreliable with large differences in models derived at differing strike angles. That said, with the exception of the mantle structure along the eastern margin of the Kimberley Basin, there do not appear to be any anomalous zones of enhanced conductivity such as the Central Slave Mantle conductor observed beneath the Slave Craton (Jones et al., 2003), or associated with mantle shearing like that interpreted beneath the Wopmay Orogen (Spratt et al., 2009) and beneath the southern Melville Peninsula of the Rae Craton (Spratt et al., 2013a). There may be minor variations across the region, but these remain unresolved with 2D methods.

The lithosphere–asthenosphere boundary is traditionally and formally defined as a change in rheology from a strong outer shell which is underlain by a less viscous asthenosphere. For decades, MT studies have globally detected an increase in electrical conductivity between 50 and 250 km that has been widely recognized as the electrical lithosphere–asthenosphere boundary (Korja, 2007; Eaton et al., 2009). This increase has not been observed in the Kimberley data — an indication that a thick lithosphere is present beneath the region. Sensitivity testing along each of the four main profiles shows that in some areas the resolution of the models is limited to the uppermost 60–80 km. However, this analysis has shown that along Profile Central, the western half of Profile East, and the eastern half of Profile West the data are sensitive to at least 120 km depths. These depths represent an estimate of the minimum thickness of the lithosphere in the survey area.

Conclusions

The MT data have imaged the deep 2D conductivity structure of the crust and uppermost mantle successfully. Strike and dimensionality analysis reveal that the regional geoelectric strike angle varies greatly across the profile area and with depth, but that locally, 2D models can be reliable.

The models reveal a thin conductive near-surface layer, interpreted as Kimberley Basin sedimentary and volcanic rocks, up to 5 km thick. In general, the upper crust is resistive to depths of 15–40 km, and is underlain by a conductive layer which appears to be discontinuous at or near major crustal block boundaries. Several upper-crustal features are identified that correlate with the location of fractures, or boundaries between crustal terrains that are either mapped at the surface or inferred from gravity and aeromagnetic data. A northwest-dipping resistive unit is imaged along the eastern margin of the Kimberley Basin that extends into the upper mantle and is interpreted as the remnants of a subducted lithosphere.

In general, significant 3D distortion effects are predicted for the upper mantle; however, the models do not reveal any major zones of enhanced conductivity in the Kimberley region.

Acknowledgements

We thank Ray Addenbrooke for his considerable assistance in the field, pastoralists at Kimberley Downs, Napier Downs, and Mount House Stations; the Department of Parks and Wildlife rangers at Silent Grove, Windjana Gorge, and Mitchell Falls; and the field crew — Nick Mann, Cody Graco, Dean Clinnick and Christian Anzenhofer.

References

Chave, AD and Jones, AG (editors) 2012, The magnetotelluric method: theory and practice: Cambridge University Press, New York, USA, 552p.

Banks, RJ, Livelybrooks, D, Jones, P and Longstaff, R 1996, Causes of high crustal conductivity beneath the Iapetus suture zone in Great Britain: Geophysical Journal International, v. 124, p. 433–455.

Betts, PG and Giles, D 2006, The 1800–1100 Ma tectonic evolution of Australia: Precambrian Research, v. 144, p. 92–125.

Betts, PG, Giles, D, Lister, GS and Frick, LR 2002, Evolution of the Australian Lithosphere: Australian Journal of Earth Sciences, v. 49, p. 661–695.

Blake, DH, Tyler, IM and Page, RW 2000, Regional Geology of the Halls Creek Orogen, *in* Geology and economic potential of the Palaeoproterozoic layered mafic–ultramafic intrusions in the East Kimberley, Western Australia *edited by* DM Hoatson and DH Blake: Australian Geological Survey Organisation, Bulletin 246, p. 35–62.

Bodorkos, S, Cawood, PA and Oliver, NHS 2000, Timing and duration of synmagmatic deformation in the Mabel Downs Tonalite, northern Australia: Journal of Structural Geology, v. 22, p. 1181–1198.

Bodorkos, S and Reddy, SM 2004, Proterozoic cooling and exhumation of the northern central Halls Creek Orogen, Western Australia: constraints from a reconnaissance $^{40}Ar/^{39}Ar$ study: Australian Journal of Earth Sciences, v. 51, no. 4, p. 561–609.

Bostick, FX 1977, A simple almost exact method of magnetotelluric analysis, in Processing workshop on electrical methods in geothermal exploration: US Geological Survey, p. 174–183.

Cagniard, L 1953, Basic theory of the magnetotelluric method of geophysical prospecting: Geophysics, v. 18, p. 605–635.

Caldwell, TG, Bibby, HM and Brown, C 2004, The magnetotelluric phase tensor: Geophysical Journal International, v. 158, p. 457–469.

Cawood, PA and Korsch, RJ 2008, Assembling Australia: Proterozoic building of a continent: Precambrian Research, v. 166, no. 1–4, p. 1–38.

Clitheroe, G, Gudmundsson, O and Kennett, BLN 2000, The crustal thickness of Australia: Journal of Geophysical Research, v. 105, p. 13697–13713.

Coats, R and Preiss, W 1980, Stratigraphic and geochronological reinterpretation of late Proterozoic glaciogenic sequences in the Kimberley region, Western Australia: Precambrian Research, v. 13, p. 181–208.

Collins, CDN, Drummond, BJ and Nicoll, MG 2003, Crustal thickness patterns in the Australian continent: Geological Society of America Special Papers, v. 372, p. 121–128.

Constable, SC 2006, SEO3: A new model of olivine electrical conductivity: Geophysical Journal International, v. 166, p. 435–437.

Craven, JA, Skulski, T and White, DW 2004, Lateral and vertical growth of cratons: seismic and magnetotelluric evidence from the western Superior transect, in Lithoprobe Report 86: The University of British Columbia; Lithoprobe Celebratory Conference, Toronto, 12 October 2004.

Davis, WJ, Jones, AG, Bleeker, W and Grutter, H 2003, Lithosphere development in the Slave craton: a linked crustal and mantle perspective: Lithos, v. 71, p. 575–589.

Dentith, MC, Evans, S, Thiel, S, Gallardo, L, Joly, A and Romano, SS 2013, A magnetotelluric traverse across the southern Yilgarn Craton: Geological Survey of Western Australia, Report 121, 43p.

Downes, PP, Griffin, BJ and Griffin, WL 2007, Mineral chemistry and zircon geochronology of xenocrysts and altered mantle and crustal xenoliths from the Aries micaceous kimberlite: Constraints on the composition and age of the central Kimberley Craton, Western Australia: Lithos, v. 93, p. 175–198.

Duba, AL and Shankland, TJ 1982, Free carbon and electrical conductivity in the Earth's mantle: Geophysical Research Letters, v. 9, p. 1271–1274.

Ducea, MN and Park, SK 2000, Enhanced mantle conductivity from sulfide minerals, southern Sierra Nevada, California: Geophysical Research Letters, v. 27, p. 2405–2408.

Eaton, DW, Darbyshire, F, Evans, RL, Grutter, H, Jones, AG and Yuan, X 2009, The elusive lithosphere-asthenosphere boundary (LAB) beneath cratons: Lithos, v. 109, p. 1–22, doi:10.1016/j.lithos.2008.05.009.

Evans, RL, Jones, AG, Garcia, X, Muller, M, Hamilton, M, Evans, S, Fourie, S, Sprat, J, Webb, S, Jelsma, H and Hutchins, D 2011, The electrical lithosphere beneath the Kaapvaal Craton, Southern Africa: Journal of Geophysical Research, v. 116, no. B04105 (Solid Earth), doi:10.1029/2010JB007883.

Fishwick, S, Kennett, BLN and Reading, AM 2005, Contrasts in lithospheric structure within the Australian Craton: Earth and Planetary Science Letters, v. 231, p. 163–176.

Gamble, TD, Goubau, WM and Clarke, J 1979, Magnetotellurics with a remote reference: Geophysics, v. 44, p. 53–68.

Gellatly, DC 1971, Possible Archaean rocks of the Kimberley region, Western Australia: Geological Society of Australia, v. 3 (Special Publication), p. 93–101.

Gellatly, DC, Derrick, GM and Plumb, KA 1970, Proterozoic palaeocurrent directions in the Kimberley region, northwestern Australia: Geological Magazine, v. 107, p. 249–257.

Glass, LM and Phillips, D 2006, The Kalkarindji continental flood basalt province: a new Cambrian large igneous province in Australia with possible links to faunal extinctions: Geology, v. 34, no. 6, p. 461–464, doi:10.1130/G22122.1.

Glover, PWJ, Pous, J, Queralt, P, Munoz, J-A, Liesa, M and Hole, MJ 2000, Integrated two-dimensional lithospheric conductivity modeling in the Pyrenees using field-scale and laboratory measurements: Earth and Planetary Science Letters, v. 178, p. 59–72.

Graham, S, Lambert, DD, Shee, SR, Smith, CB and Reeves, S 1999, Re-Os isotopic evidence for Archaean lithospheric mantle beneath the Kimberley block, Western Australia: Geology, v. 27, no. 5, p. 431–434.

Griffin, TJ and Myers, JS 1988, A Proterozoic terrane boundary in the King Leopold Orogen, Western Australia: Australian Journal of Earth Sciences, v. 35, p. 131–132.

Griffin, TJ, Page, RW, Sheppard, S and Tyler, IM 2000, Tectonic implications of Palaeoproterozoic post-collisional, high-K felsic igneous rocks from the Kimberley region of northwestern Australia: Precambrian Research, v. 101, p. 1–23.

Griffin, TJ, Tyler, IM and Playford, PE 1993, Explanatory notes on the Lennard River 1:250 000 geological sheet SE/51-8, Western Australia (3rd edition): Geological Survey of Western Australia, Record 1992/5, 85p.

Gunn, PJ and Meixner, AJ 1998, The nature of the basement to the Kimberley Block, northwestern Australia: Exploration Geophysics, v. 29, p. 506–511.

Hanley, LM and Wingate, MTD 2000, SHRIMP zircon age for an Early Cambrian dolerite dyke: an intrusive phase of the Antrim Plateau Volcanics of northern Australia: Australian Journal of Earth Sciences, v. 47, p. 1029–1040.

Hyndman, RD, Vanyan, LL, Marquid, G and Lay, LK 1993, The origin of electrically conductive lower continental crust: saline water or graphite?: Physics of the Earth and Planetary Interiors, v. 81, p. 325–345.

Jones, AG 1992, Electrical conductivity of the continental lower crust, *in* Continental lower crust *edited by* DM Fountain, R Arculus and RW Kay: Elsevier, Amsterdam, The Netherlands, Developments in geotectonics 23, p. 81–144.

Jones, AG 1999, Imaging the continental upper mantle using electromagnetic methods: Lithos, v. 48, p. 57–80.

Jones, AG, Craven, JA, McNeice, GA, Ferguson, IJ, Boyce, T, Farquharson, C and Ellis, RG 1993, North American Central Plains conductivity anomaly within the Trans-Hudson orogen in northern Saskatchewan: Geology, v. 21, p. 1027–1030.

Jones, AG 2006, Electromagnetic interrogation of the anisotropic Earth: Looking into the Earth with polarized spectacles: Physics of the Earth and Planetary Interiors, v. 158, p. 281–291.

Jones, AG, Evans, RL and Eaton, DW 2009a, Velocity–conductivity relationships for mantle mineral assemblages in Archean cratonic lithosphere based on a review of laboratory data and Hashin–Shtrikman extremal bounds: Lithos, v. 109, p. 131–143.

Jones, AG, Evans, RL, Muller, MR, Hamilton, MP, Miensopust, MP, Garcia, X, Cole, P, Ngwisanyi, T, Hutchins, D, Fourie, CJS, Jelsma, H, Aravanis, T, Pettit, W, Webb, S and Wasborg, J 2009b, Area selection for diamonds using magnetotellurics: examples from South Africa: Lithos, v. 112S, p. 83–92.

Jones, AG and Ferguson, IJ 2001, The electric Moho: Nature, v. 409, no. 6818 (18 January), p. 331–333.

Jones, AG, Fullea, J, Evans, RL and Muller, MR 2012, Calibrating laboratory-determined models of electrical conductivity of mantle minerals using geophysical and petrological observations: Geochemistry, Geophysics, Geosystems, v. 13, no. Q06010, doi:10.1029/2012GC004055.

Jones, AG and Jödicke, H 1984, Magnetotelluric transfer function estimation improvement by a coherence based rejection technique (EM1.5), *in* Abstract Volume: 54th Society of Exploration Geophysics Annual General Meeting, Atlanta, Georgia, USA, SEG Extended Abstracts v. 3, p. 51–55.

Jones, AG, Ledo, J and Ferguson, IJ 2005, Electromagnetic images of the Trans-Hudson orogen: The North American Central Plains anomaly revealed: Candian Journal of Earth Sciences, v. 42, p. 495–515.

Jones, AG, Lezaeta, P, Ferguson, IJ, Chave, AD, Evans, R, Garcia, X and Spratt, J 2003, The electrical structure of the Slave craton: Lithos, v. 71, p. 505–527.

Karato, S 1990, The role of hydrogen in the electrical conductivity of the upper mantle: Nature, v. 347, p. 272–273.

Karato, S 2006, Influence of hydrogen-related defects on the electrical conductivity and plastic deformation of mantle minterals: a critical review, *in* Earth's Deep Water Cycle *edited by* SD Jacobson and S van der Lee: American Geophysical Union, Washington DC, US, p. 113–129.

Kennard, JM, Jackson, MJ, Romine, KK, Shaw, RD and Southgate, PN 1994, Depositional sequences and associated petroleum systems of the Canning Basin, WA, *in* The Sedimentary Basins of Western Australia *edited by* PG Purcell and RR Purcell: Petroleum Exploration Society of Australia, Western Australian Branch, Perth, Western Australia, p. 657–676.

Korja, T 2007, How is the European lithosphere imaged by magnetotellurics?: Surveys in Geophysics, v. 28, p. 239–272.

Ledo, J and Jones, AG 2005, Upper mantle temperature determined from combining mineral composition, electrical conductivity laboratory studies and magnetotelluric field observations: Application to the Intermontane Belt, Norther Canadian Cordillera: Earth and Planetary Science Letters, v. 236, p. 479–493.

Mackie, RL and Madden, TR 1993, Three dimensional magnetotelluric inversion using conjugate gradients: Geophysical Journal International, v. 115, p. 215–229.

Mory, AJ 1990a, Bonaparte Basin, in Geology and mineral resources of Western Australia: Geological Survey of Western Australia, Memoir 3, p. 380–415.

Mory, AJ 1990b, Ord Basin, in Geology and mineral resources of Western Australia: Geological Survey of Western Australia, Memoir 3, p. 415–425.

Muller, MR, Jones, AG, Evans, RL, Grutter, HS, Hatton, C, Garcia, X, Hamilton, MP, Miensopust, MP, Cole, P, Ngwisanyi, T, Hutchins, D, Fourie, CJS, Jelsma, HA, Evans, SF, Aravanis, T, Pettit, W, Webb, SJ and Wasborg, J 2009, Lithosphere structure evolution and diamond prospectivity of the Rehoboth Terrane and western Kaapvaal Craton, southern Africa: constraints from broadband magnetotellurics: Lithos, v. 112S, p. 93–105.

Myers, JS, Shaw, RD and Tyler, IM 1996, Tectonic evolution of Proterozoic Australia: Tectonics, v. 15, p. 1431–1146.

Niblett, ER and Sayn-Wittgenstein, C 1960, Variation of electrical conductivity with depth by the magnetotelluric method: Geophysics, v. 25, p. 998–1008.

Orth, K 2002, Setting of the Palaeoproterozoic Koongie Park Formation and carbonate-associated base metal mineralisation, at Koongie Park, northwestern Australia: University of Tasmania, Hobart, Tasmania, PhD thesis (unpublished), 460p.

Page, RW, Blake, DH, Sun, S-S, Tyler, IM, Griffin, TJ and Thorne, AM 1994, New geological and geochronological constraints on volcanogenic massive sulphide prospectivity near Halls Creek (WA): AGSO Research Newsletter, v. 20, p. 5–7.

Page, RW, Griffin, TJ, Tyler, IM and Sheppard, S 2001, Geochronological constraints on tectonic models for Australian Palaeoproterozoic high-K granites: Journal of the Geological Society, v. 158, p. 535–545.

Percial, JA, Sanborn-Barrie, M, Skulski, T, Stott, GM, Helmstaedt, H and White, JJ 2006, Tectonic evolution of the western Superior Province from NATMAP and Lithoprobe studies: Candian Journal of Earth Sciences, v. 42, p. 1085–1117.

Pidgeon, RT, Smith, CB and Fanning, CM 1989, Kimberlite and lamproite emplacement ages in Western Australia, *in* Kimberlites and related rocks: their composition, occurrence, origin and emplacement *edited by* J Ross: Geological Society of Australia, Special Publication 14, p. 369–381.

Plumb, KA and Gemuts, I 1976, Precambrian geology of the Kimberley region, Western Australia: 25th International Geological Congress, Excursion guide 44C, 69p.

Poe, BT, Romano, C, Nestola, F and Smyth, JR 2010, Electrical conductivity anisotropy of dry and hydrous olivine at 8 GPa: Physics of the Earth and Planetary Interiors, doi:10.1016/j.pepo.2010.05.003.

Rodi, W and Mackie, RL 2001, Nonlinear conjugate gradients algorithm for 2-D magnetotelluric inversion: Geophysics, v. 66, p. 174–187.

Saygin, E and Kennett, BLN 2012, Crustal structure of Australia from ambient seismic noise tomography: Journal of Geophysical Research: Solid Earth, v. 117, no. B1, p. n/a–n/a, 10.1029/2011JB008403.

Schmucker, U 1970, An introduction to induction anomalies: Journal of Geomagnetism and Geoelectricity, v. 22, p. 9–33.

Shaw, RD, Sexton, MJ and Zeilinger, I 1995, The tectonic framework of the Canning Basin, Western Australia, including 1:2 million structural elements map of the Canning Basin: Australian Geological Survey Organisation, Record 1994/048.

Shaw, RD, Tyler, IM, Griffin, TJ and Webb, AW 1992, New K-Ar constraints on the onset of subsidence in the Canning Basin, Western Australia: Journal of Australian Geology and Geophysics, v. 13.

Sheppard, S, Griffin, TJ and Tyler, IM 1997, The tectonic setting of granites in the Halls Creek and King Leopold Orogens, northwest Australia: Australian Geological Survey Organisation, Record 1997/44.

Sheppard, S, Griffin, TJ, Tyler, IM and Page, RW 2001, High- and low-K granites and adakites at a Palaeoproterozoic plate boundary in northwestern Australia: Journal of the Geological Society, v. 158, p. 547–560.

Sheppard, S, Page, RW, Griffin, TJ, Rasmussen, B, Fletcher, IR, Tyler, IM, Kirkland, CL, Wingate, MTD, Hollis, J and Thorne, AM 2012, Geochronological and isotopic constraints on the tectonic setting of the c. 1800 Ma Hart Dolerite and the Kimberley and Speewah Basins, northern Western Australia: Geological Survey of Western Australia, Record 2012/7, 28p.

Sheppard, S, Tyler, IM, Griffin, TJ and Taylor, RW 1999, Palaeoproterozoic subduction-related and passive margin basalts in the Halls Creek Orogen, northwest Australia: Australian Journal of Earth Sciences, v. 46, p. 679–690.

Simpson, F and Bahr, K 2005, Practical magnetotellurics: Cambridge University Press, Cambridge, England, 270p.

Spratt, JE, Jones, AG, Jackson, VA, Collins, L and Avdeeva, A 2009, Lithospheric geometry of the Wopmay Orogen from a Slave craton to Bear Province magnetotelluric transect: Journal of Geophysical Research, v. 114, no. B01101, doi:10.1029/2007JB005326.

Spratt, J, Jones, AG, Corrigan, D and Hogg, C 2013a, Lithospheric geometry revealed by deep-probing magnetotelluric surveying, Melville Peninsula, Nunavut: Current Research, 2013–12.

Spratt, JE, Skulski, T, Craven, JA, Jones, AG, Snyder, DB and Kiyan, D 2013b, Magnetotelluric investigations of the lithosphere beneath the central Rae craton, Mainland Nunvut, Canada: Journal of Geophysical Research.

ten Grotenhius, SM, Drury, MR, Peach, CJ and Spiers, CJ 2004, Electrical properties of fine grained olivine: evidence for grain boundary transport: Journal of Geophysical Research, v. 109, no. B06203, doi: 10.1029/2003JB002799.

Tyler, IM and Griffin, TJ 1993, Yampi, Western Australia (2nd edition): Geological Survey of Western Australia, 1:250 000 Geological Series Explanatory Notes, 32p.

Tyler, IM, Griffin, TJ, Page, RW and Shaw, RD 1995, Are there terranes within the Lamboo Complex of the Halls Creek Orogen?, *in* Geological Survey of Western Australia Annual Review 1993–94: Geological Survey of Western Australia, Perth, Western Australia, p. 37–46.

Tyler, IM and Griffin, WL 1990, Structural development of the King Leopold Orogen, Kimberley region, Western Australia: Journal of Structural Geology, v. 12, p. 703–714.

Tyler, IM, Hocking, RM and Haines, PW 2012, Geological evolution of the Kimberley region of Western Australia: Episodes, v. 35, p. 298–306.

Tyler, IM and Page, RW 1996, Palaeoproterozoic deformation, metamorphism and igneous intrusion in the central zone of the Lamboo Complex, Hall Creek Orogen: Geological Society of Australia; Australian Geological Convention, Canberra, February 1996; Abstract 41, 450p.

Tyler, IM, Page, RW and Griffin, TJ 1999, Depositional age and provenance of the Marboo Formation from SHRIMP U–Pb zircon geochronology: Implications for the early Palaeoproterozoic tectonic evolution of the Kimberley region, Western Australia: Precambrian Research, v. 95, no. 3, p. 225–243.

Tyler, IM, Sheppard, S, Bodorkos, S and Page, RW 2005, Tectonic significance of detrital zircon age profiles across Palaeoproterozoic orogens in the Kimberley region of northern Australia, *in* Geological Society of Australia, Abstracts 81: p. 33–33, 1p.

Wait, JR 1962, Theory of magnetotelluric fields: Journal of Research of the National Bureau of Standards, v. 66 (D Radio Propagation), p. 509–541.

White, SH and Muir, MD 1989, Multiple reactivation of coupled orthogonal fault systems: An example from the Kimberley region in north Western Australia: Geology, v. 17, p. 618–621.

Wight, DE and Bostick, FX 1981, Cascade decimation — a technique for real time estimation of power spectra: Institute of Electrical and Electronic Engineers; International Conference on Acoustics, Speech, and Signal Processing, Atlanta, Georgia, USA, 30 March 1981; Proceedings, p. 626–629.

Wu, X, Ferguson, IJ and Jones, AG 2002, Magnetotelluric response and geoelectric structure of the Great Slave Lake shear zone: Earth and Planetary Science Letters, v. 196, p. 35–50.

Appendix

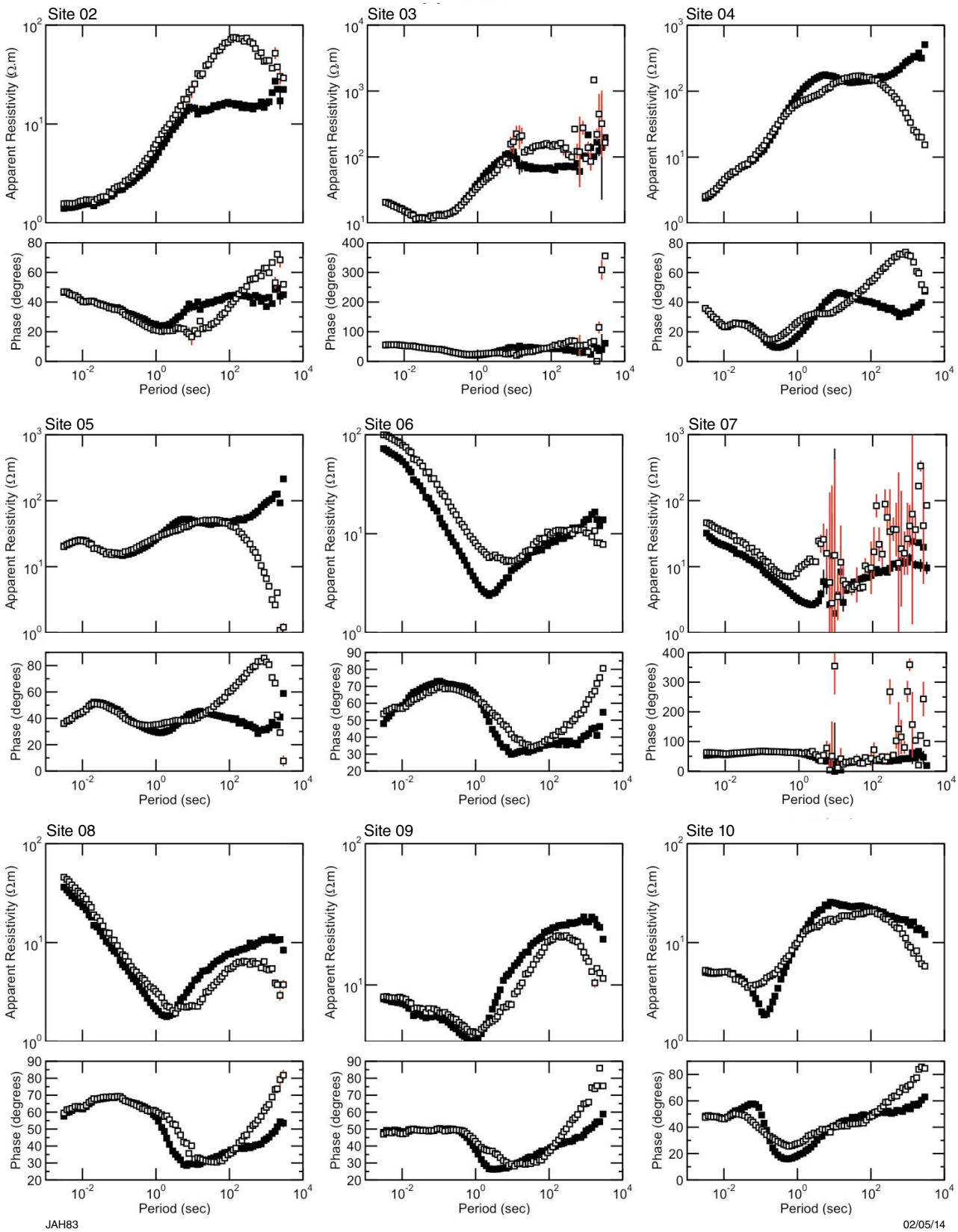
Site 02
Site 03
Site 04
Site 05
Site 06
Site 07
Site 08
Site 09
Site 10
Apparent Resistivity (Ωm)
Phase (degrees)
Period (sec)
JAH83
02/05/14

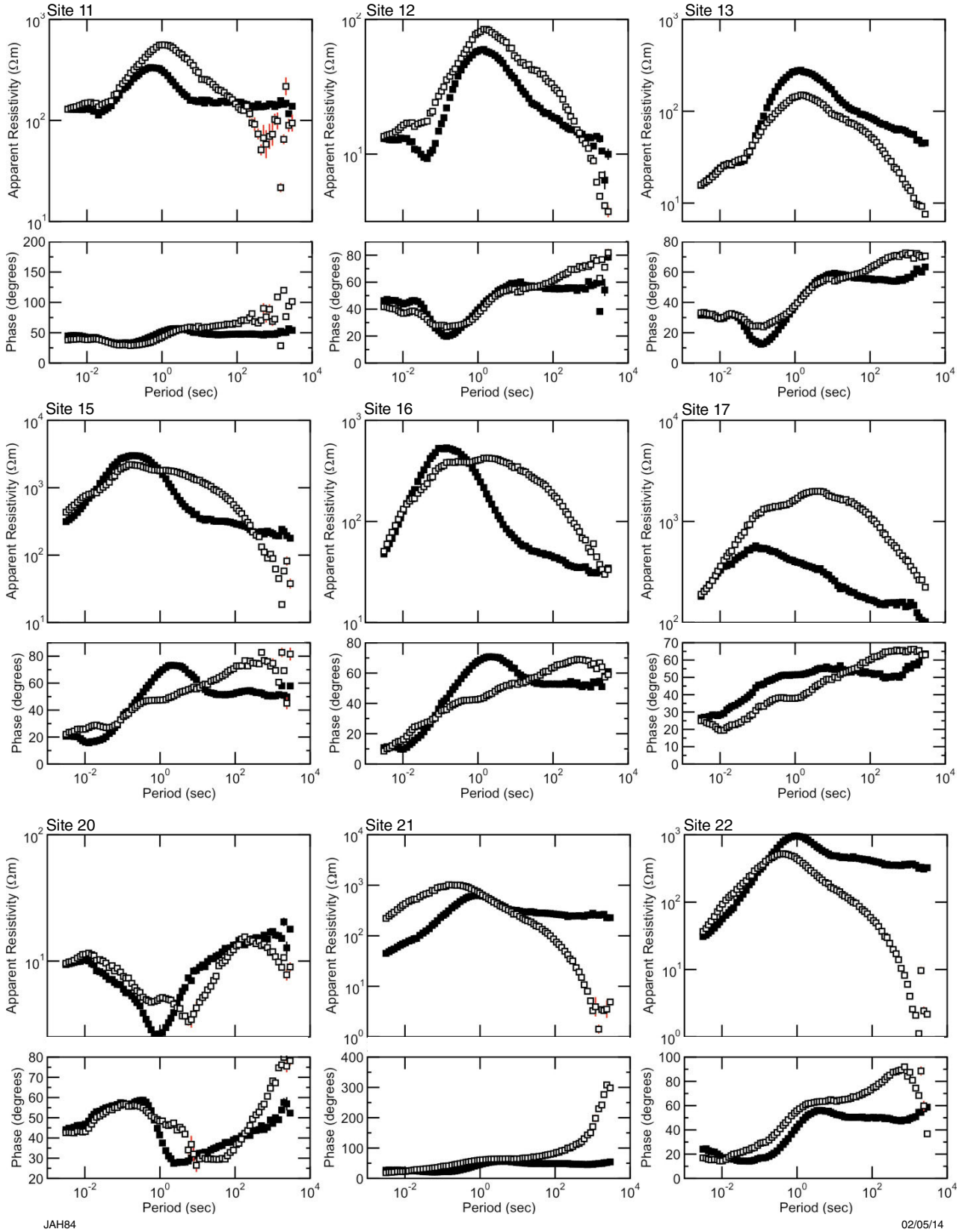
Site 11
Site 12
Site 13
Site 15
Site 16
Site 17
Site 20
Site 21
Site 22
Apparent Resistivity (Ωm)
Phase (degrees)
Period (sec)
JAH84
02/05/14

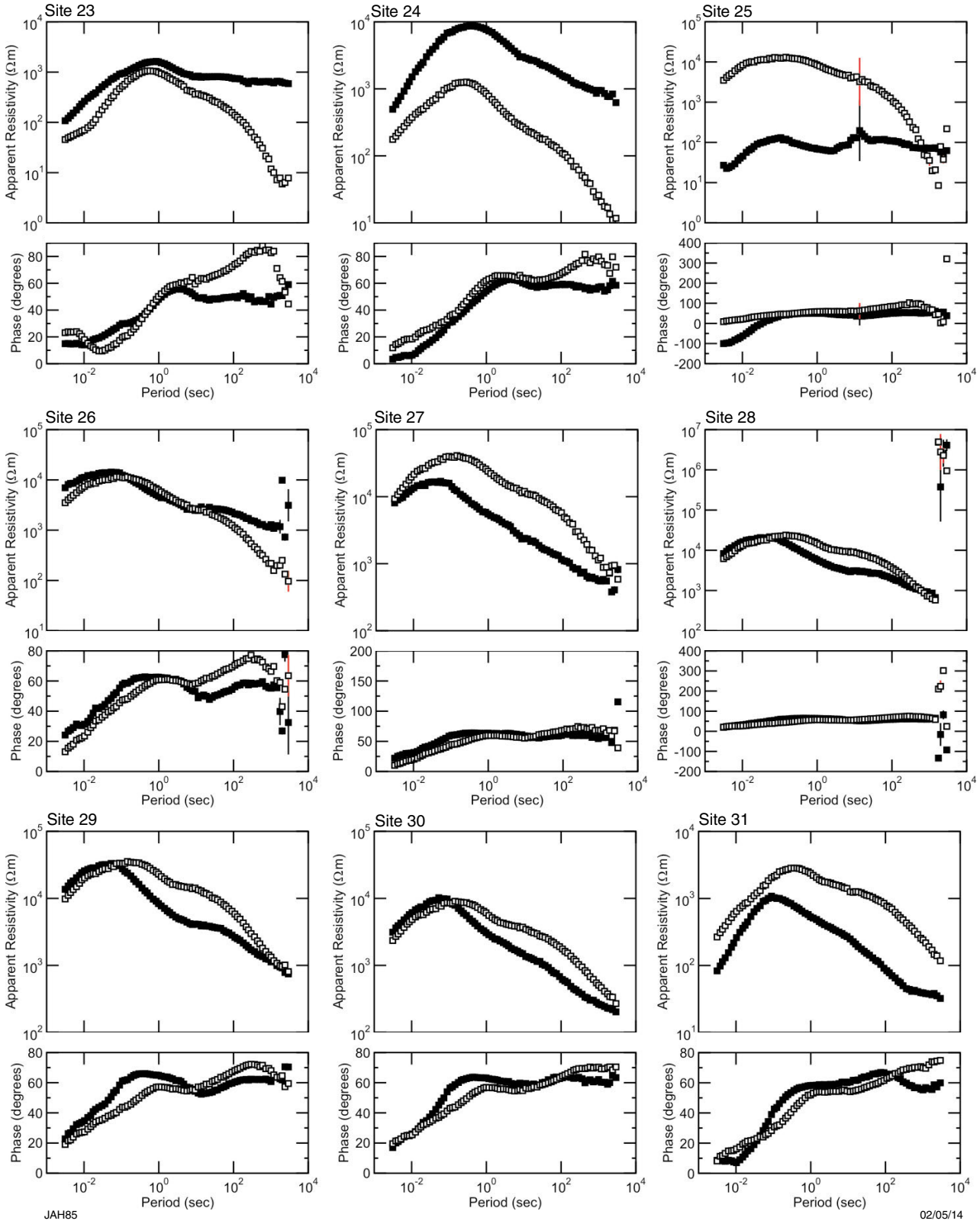
Site 23
Site 24
Site 25
Site 26
Site 27
Site 28
Site 29
Site 30
Site 31
Apparent Resistivity (Ωm)
Phase (degrees)
Period (sec)
JAH85
02/05/14

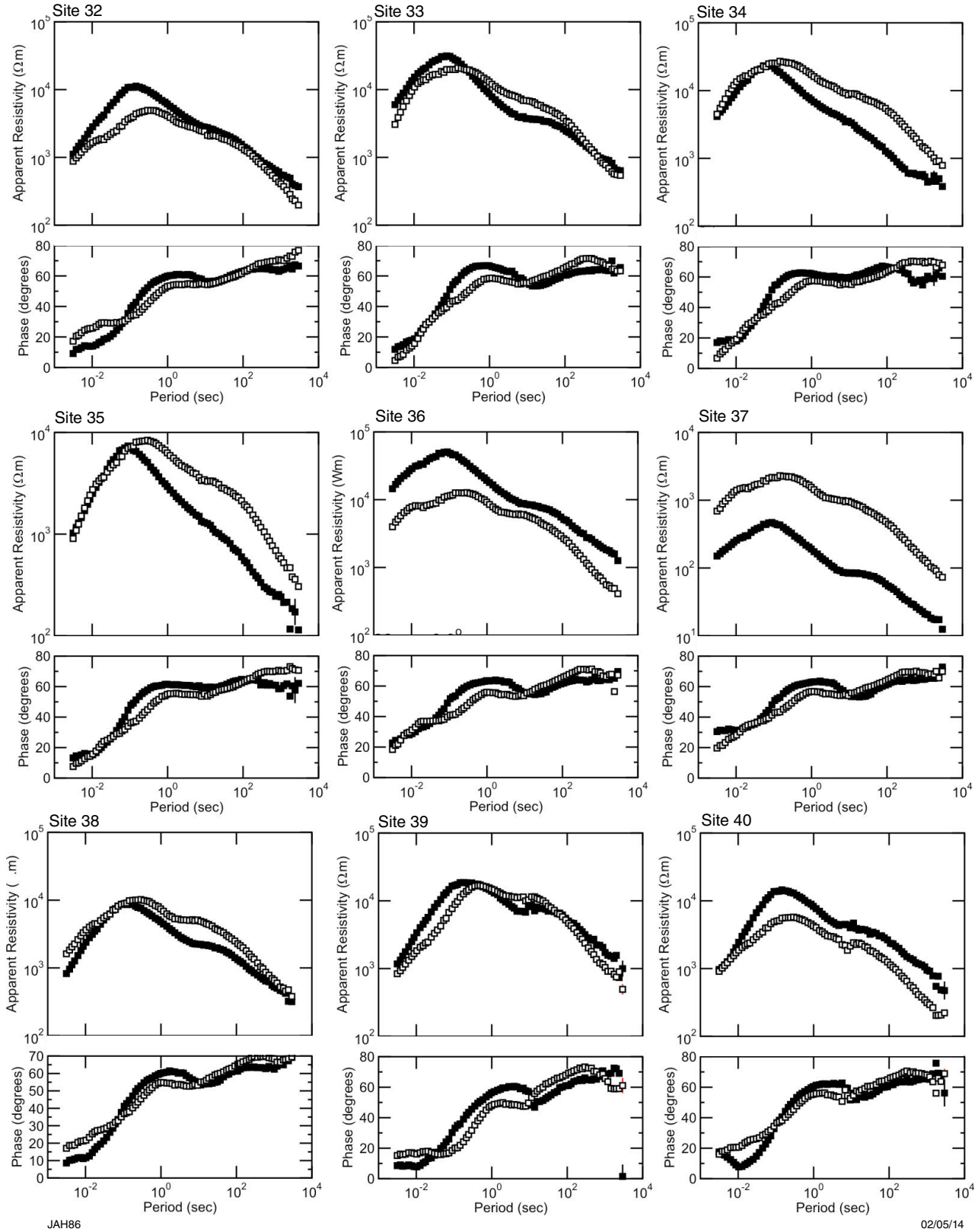
Site 32
Site 33
Site 34
Site 35
Site 36
Site 37
Site 38
Site 39
Site 40
Apparent Resistivity (Ωm)
Apparent Resistivity (Wm)
Phase (degrees)
Period (sec)
JAH86
02/05/14

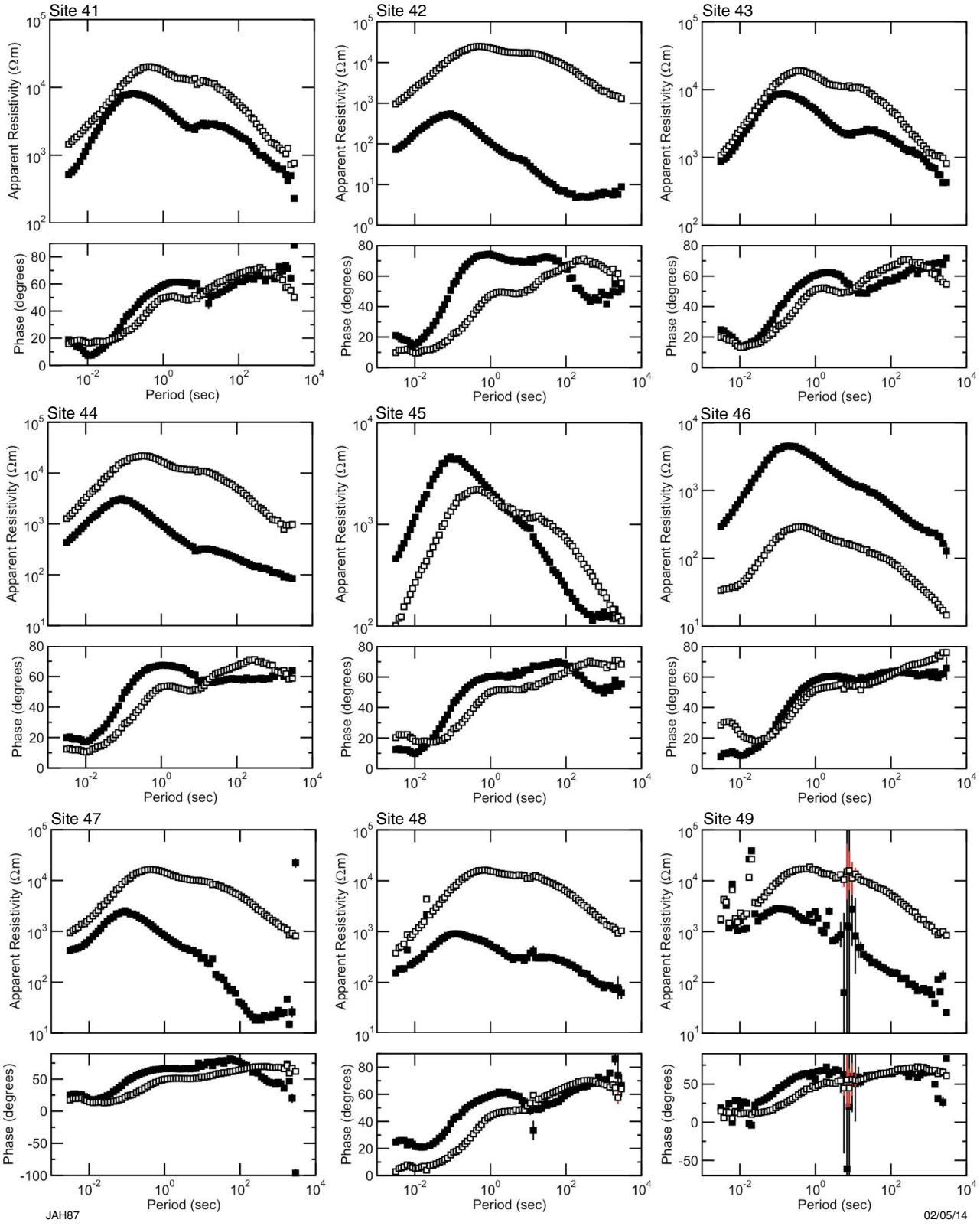
Site 41
Site 42
Site 43
Site 44
Site 45
Site 46
Site 47
Site 48
Site 49
Apparent Resistivity (Ωm)
Phase (degrees)
Period (sec)
JAH87
02/05/14

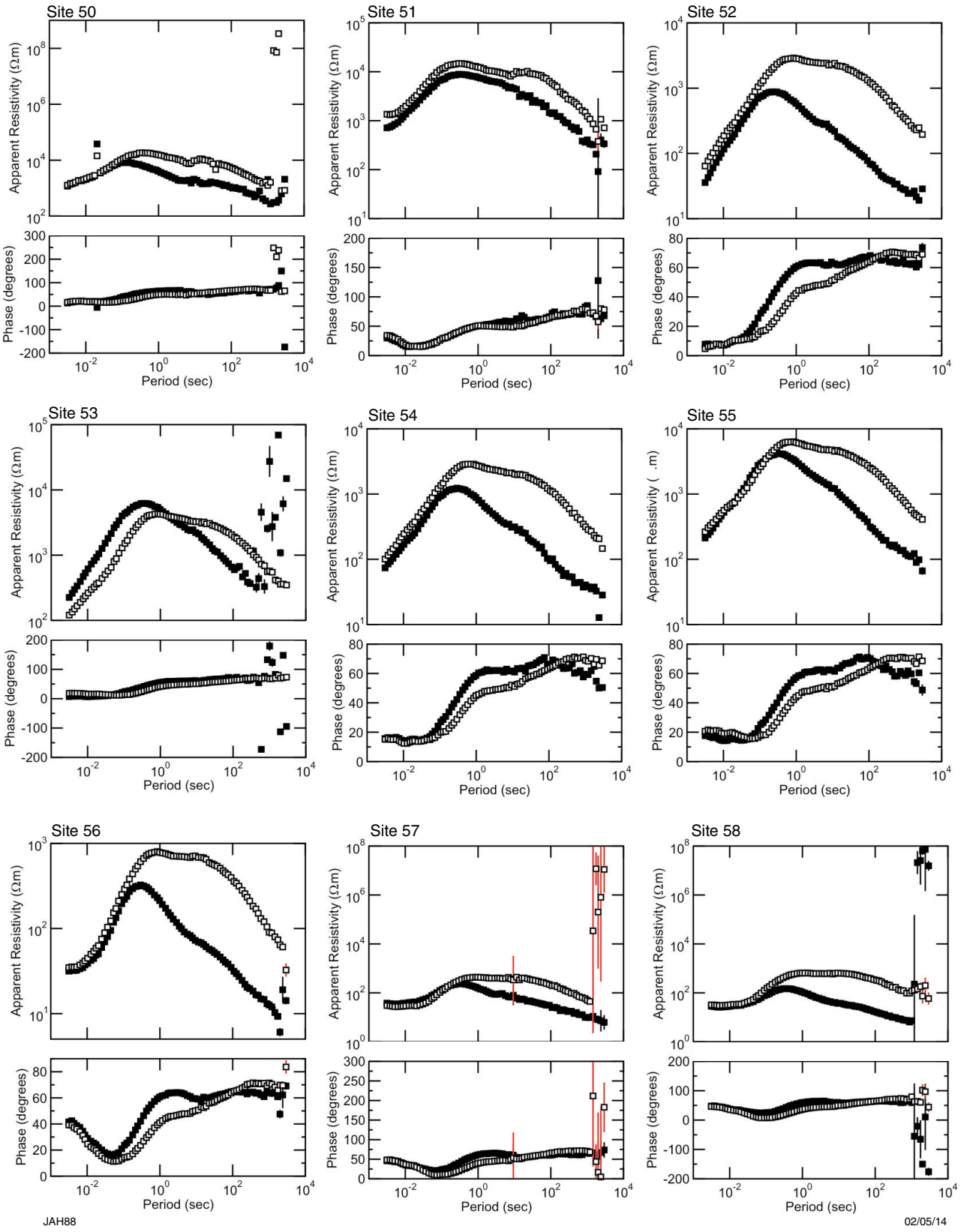
Site 50
Site 51
Site 52
Site 53
Site 54
Site 55
Site 56
Site 57
Site 58
Apparent Resistivity (Ωm)
Phase (degrees)
Period (sec)
JAH88
02/05/14

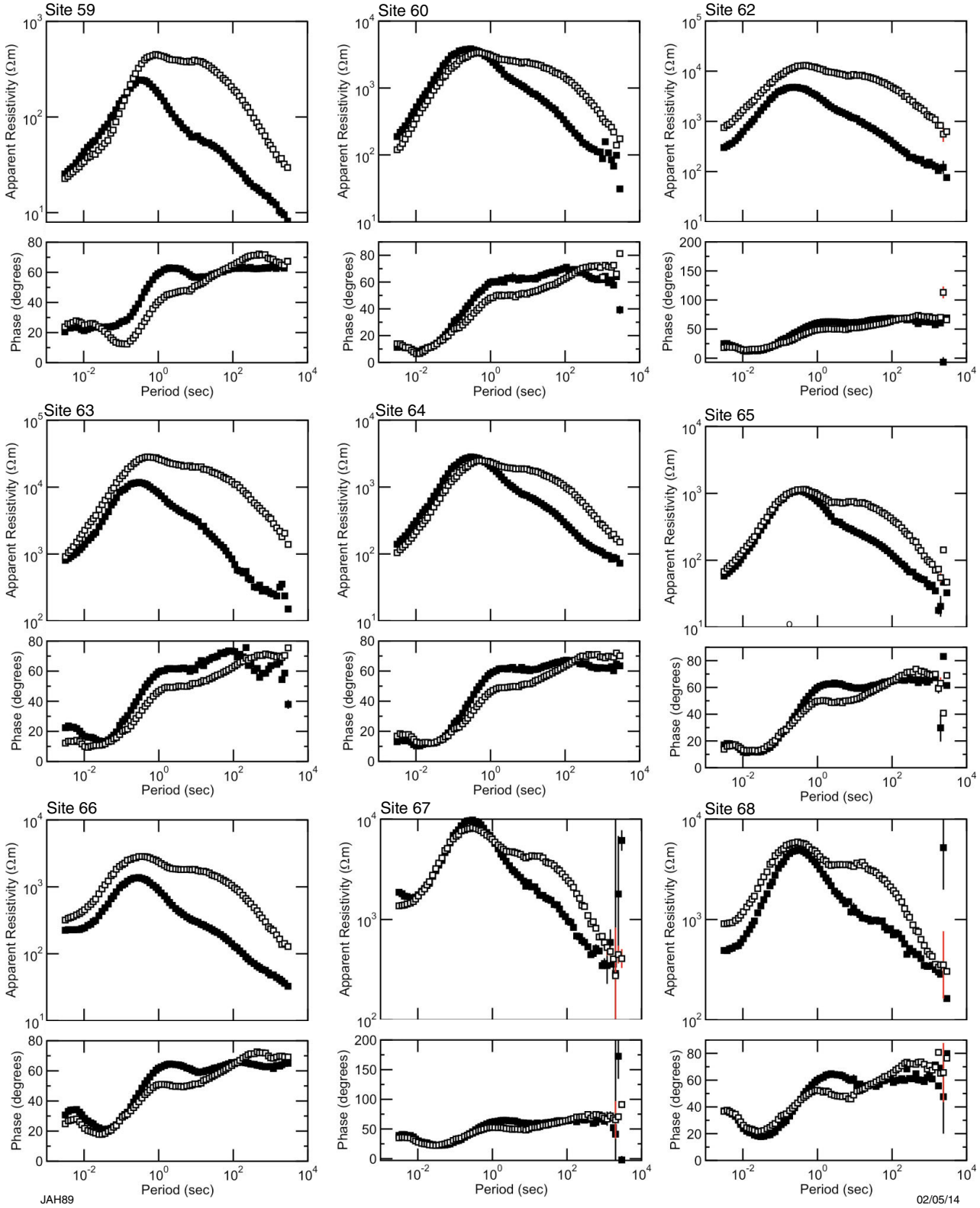
Site 59
Site 60
Site 62
Site 63
Site 64
Site 65
Site 66
Site 67
Site 68
Apparent Resistivity (Ωm)
Phase (degrees)
Period (sec)
JAH89
02/05/14

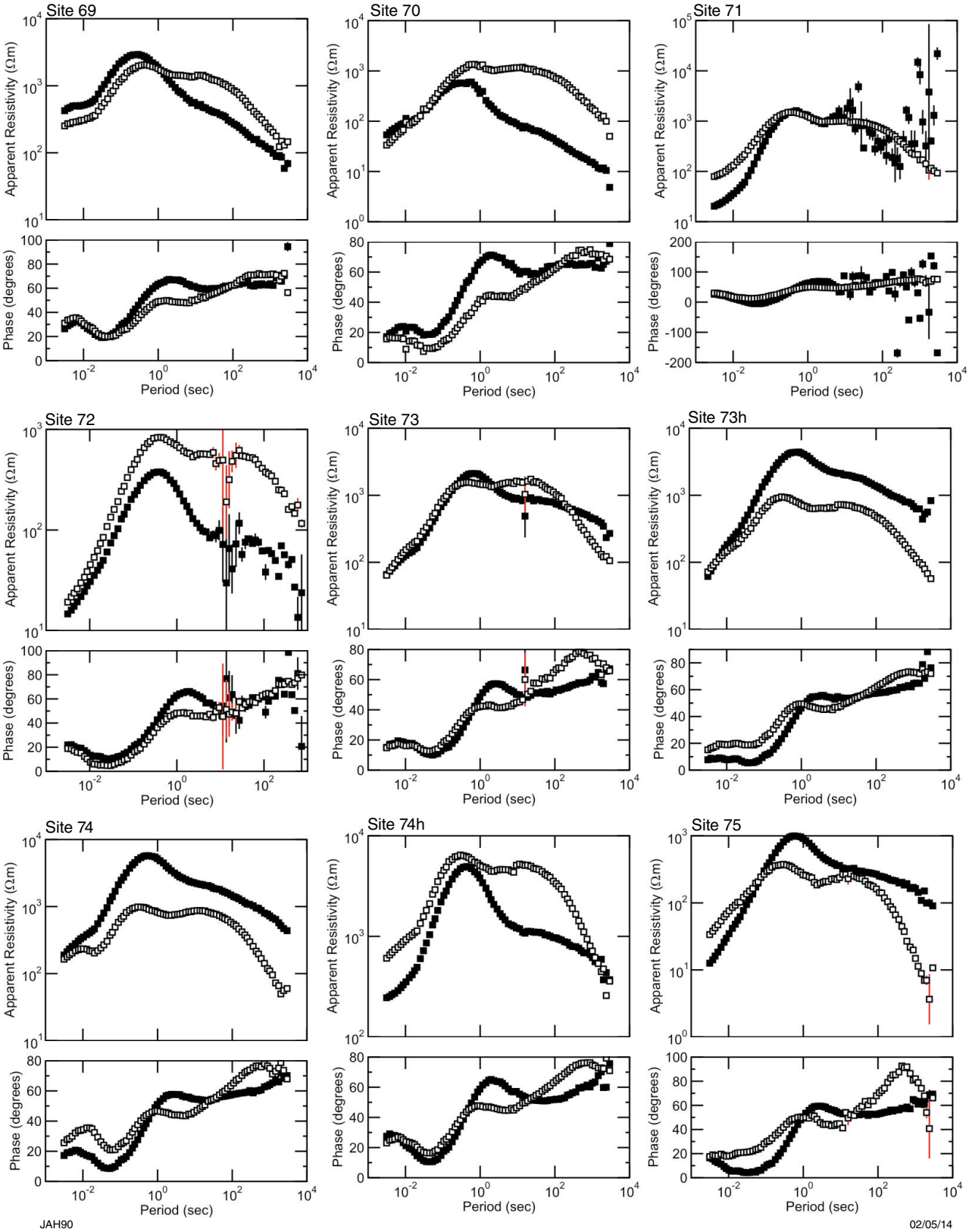
Site 69
Site 70
Site 71
Site 72
Site 73
Site 73h
Site 74
Site 74h
Site 75
Apparent Resistivity (Ωm)
Phase (degrees)
Period (sec)
JAH90
02/05/14

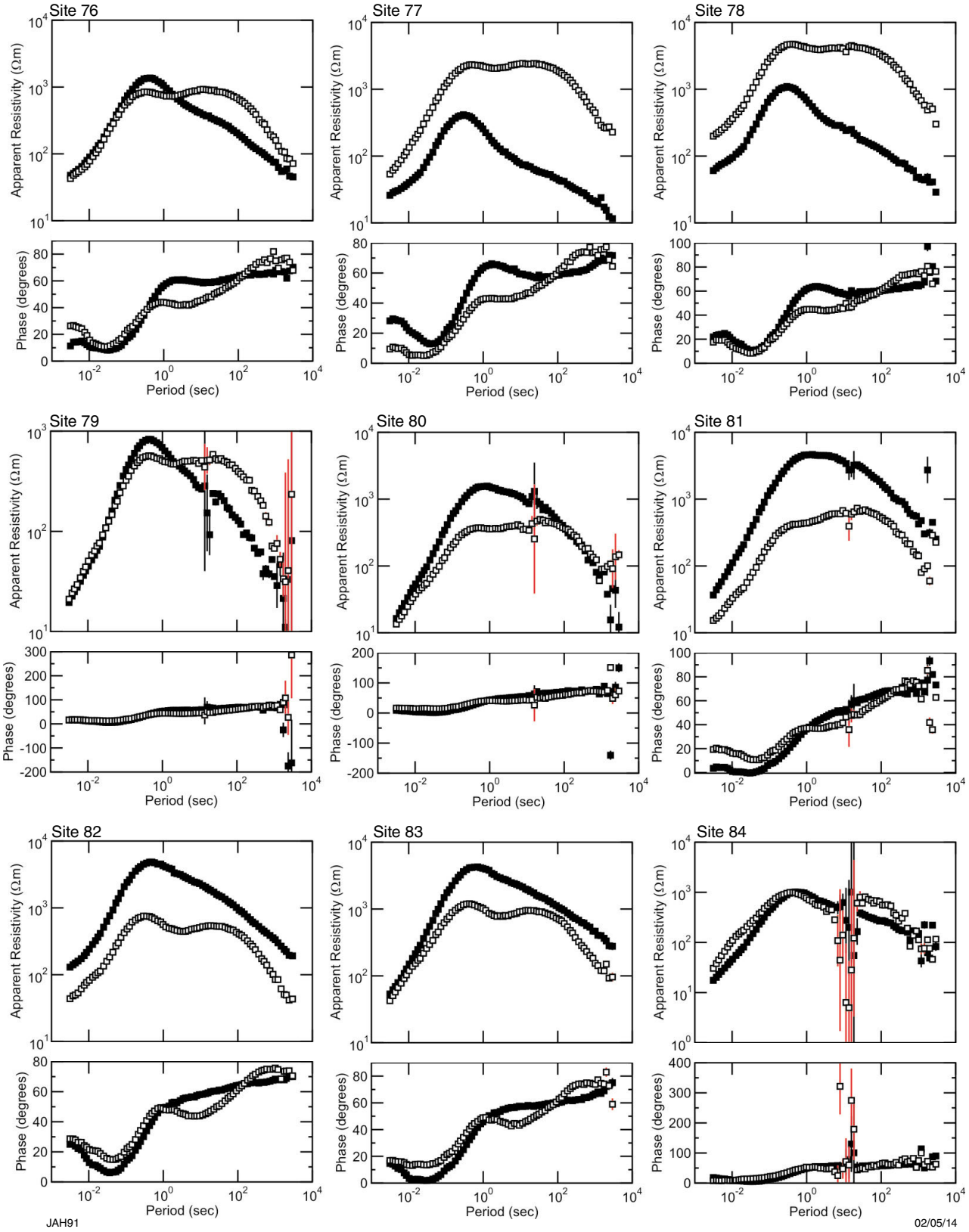
Site 76
Site 77
Site 78
Site 79
Site 80
Site 81
Site 82
Site 83
Site 84
Apparent Resistivity (Ωm)
Phase (degrees)
Period (sec)
JAH91
02/05/14

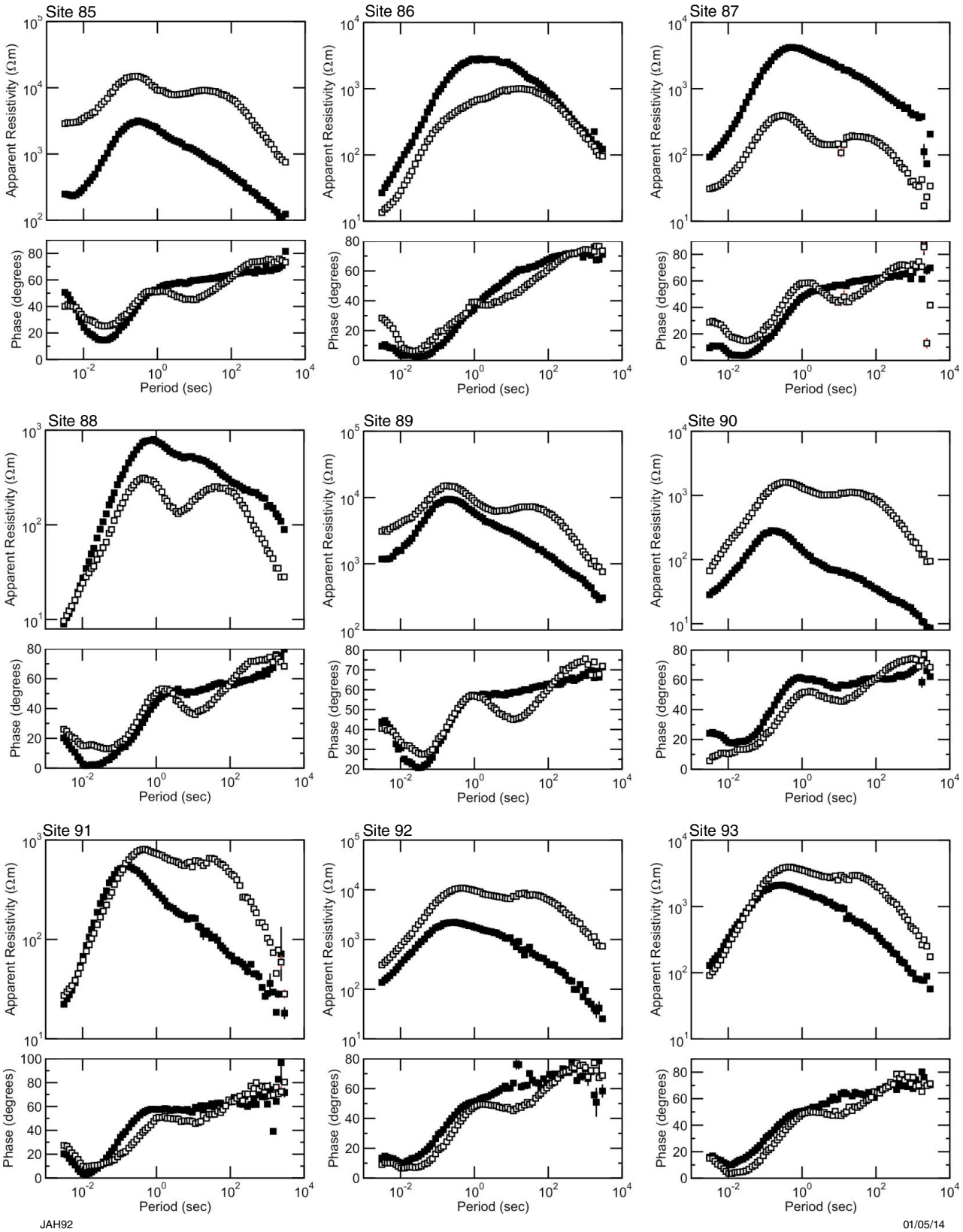
Site 85
Site 86
Site 87
Site 88
Site 89
Site 90
Site 91
Site 92
Site 93
Apparent Resistivity (Ωm)
Phase (degrees)
Period (sec)
JAH92
01/05/14

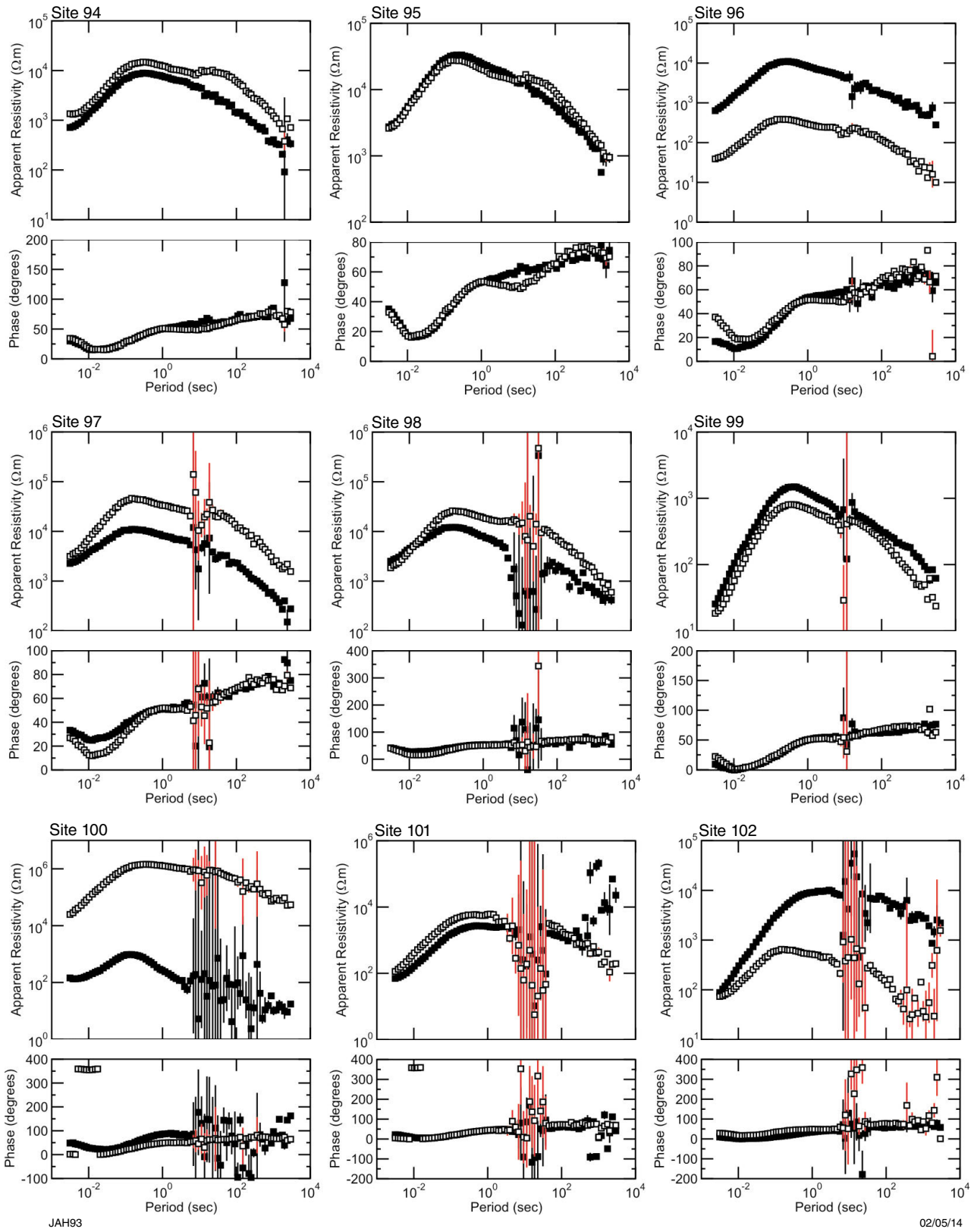
Site 94
Site 95
Site 96
Site 97
Site 98
Site 99
Site 100
Site 101
Site 102
Apparent Resistivity (Ωm)
Phase (degrees)
Period (sec)
JAH93
02/05/14

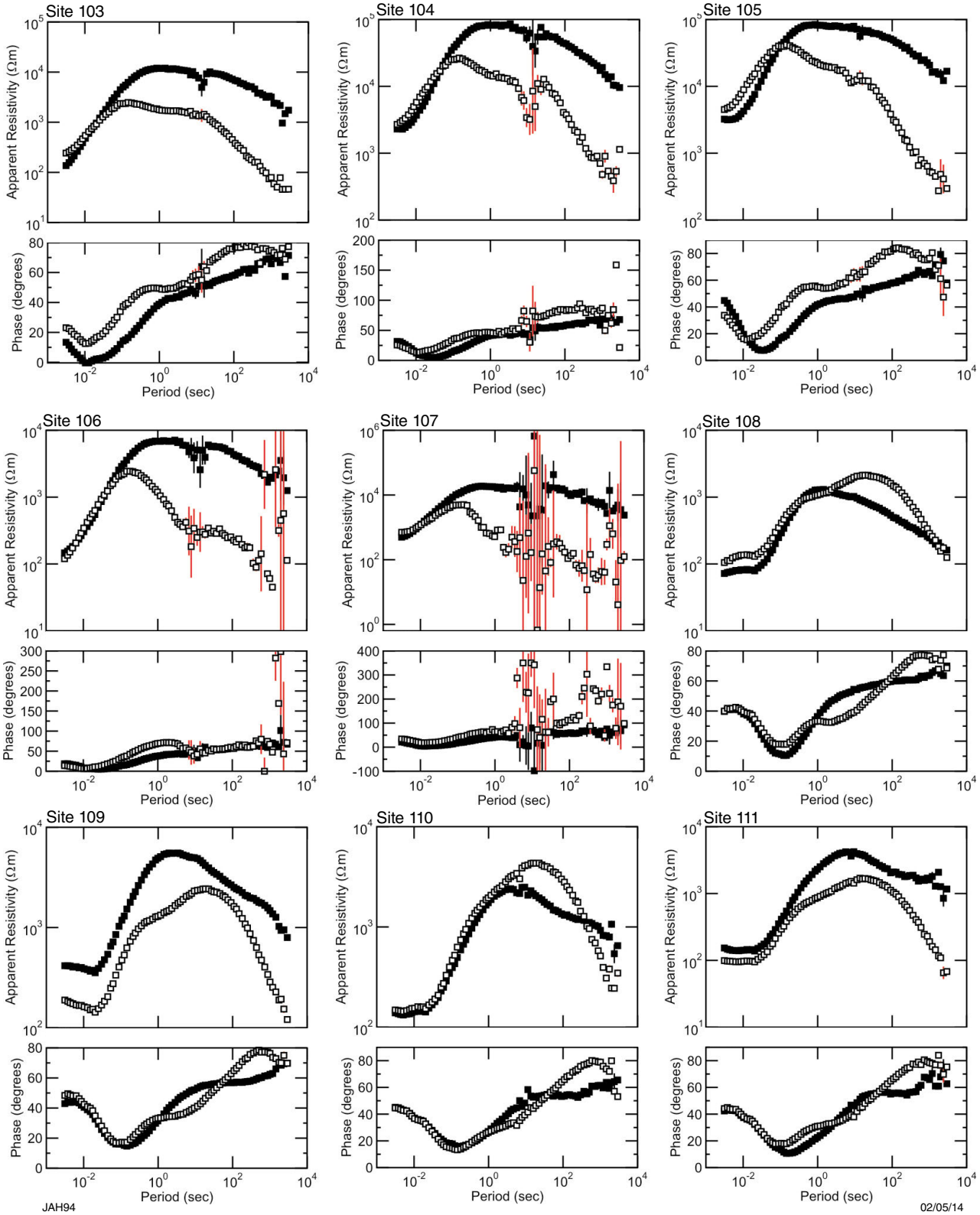
Site 103
Site 104
Site 105
Site 106
Site 107
Site 108
Site 109
Site 110
Site 111
Apparent Resistivity (Ωm)
Phase (degrees)
Period (sec)
JAH94
02/05/14

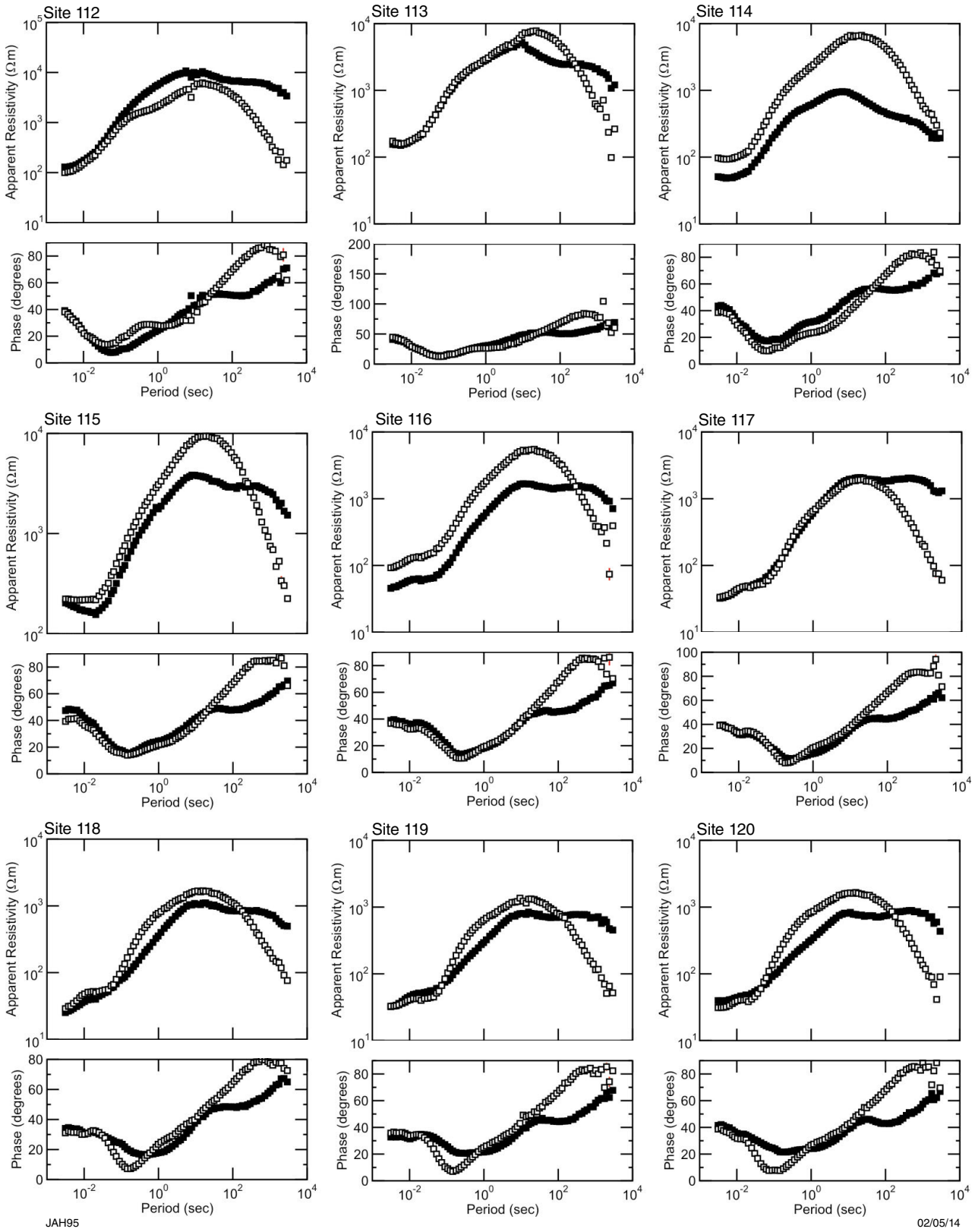
Site 112
Site 113
Site 114
Site 115
Site 116
Site 117
Site 118
Site 119
Site 120
Apparent Resistivity (Ωm)
Phase (degrees)
Period (sec)
JAH95
02/05/14

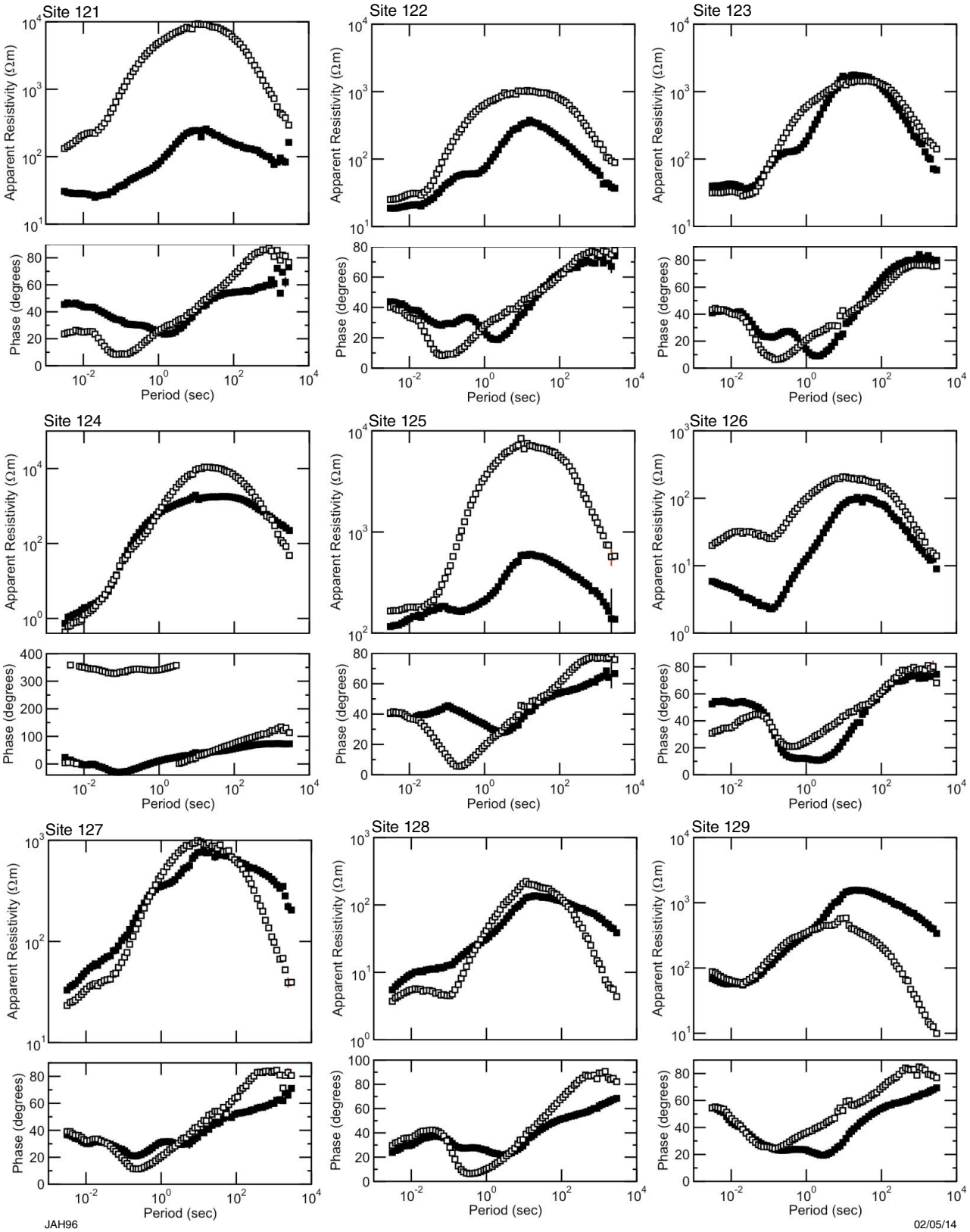
Site 121
Site 122
Site 123
Site 124
Site 125
Site 126
Site 127
Site 128
Site 129
Apparent Resistivity (Ωm)
Phase (degrees)
Period (sec)
JAH96
02/05/14

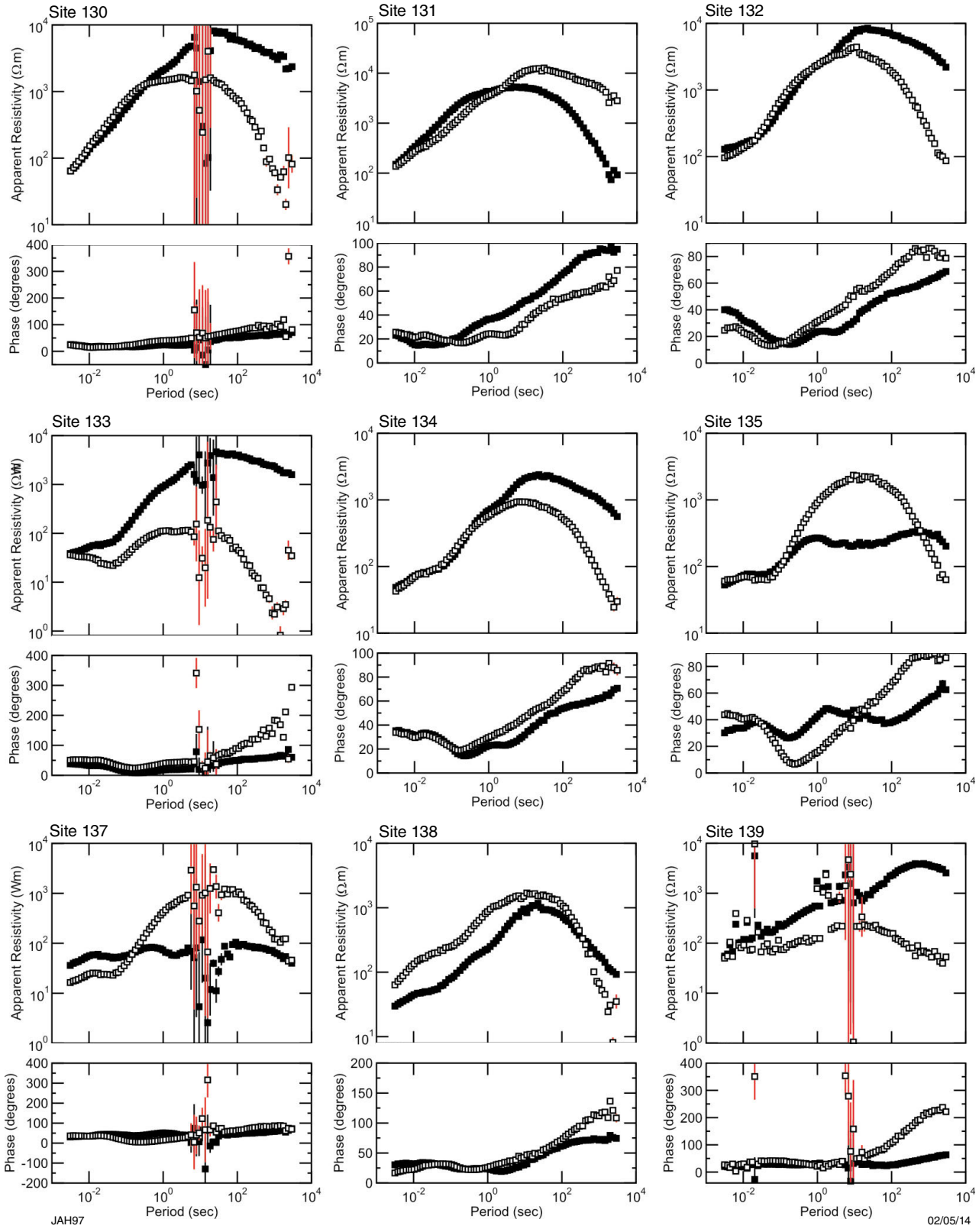
Site 130
Site 131
Site 132
Site 133
Site 134
Site 135
Site 137
Site 138
Site 139
Apparent Resistivity (Ωm)
Phase (degrees)
Period (sec)
JAH97
02/05/14

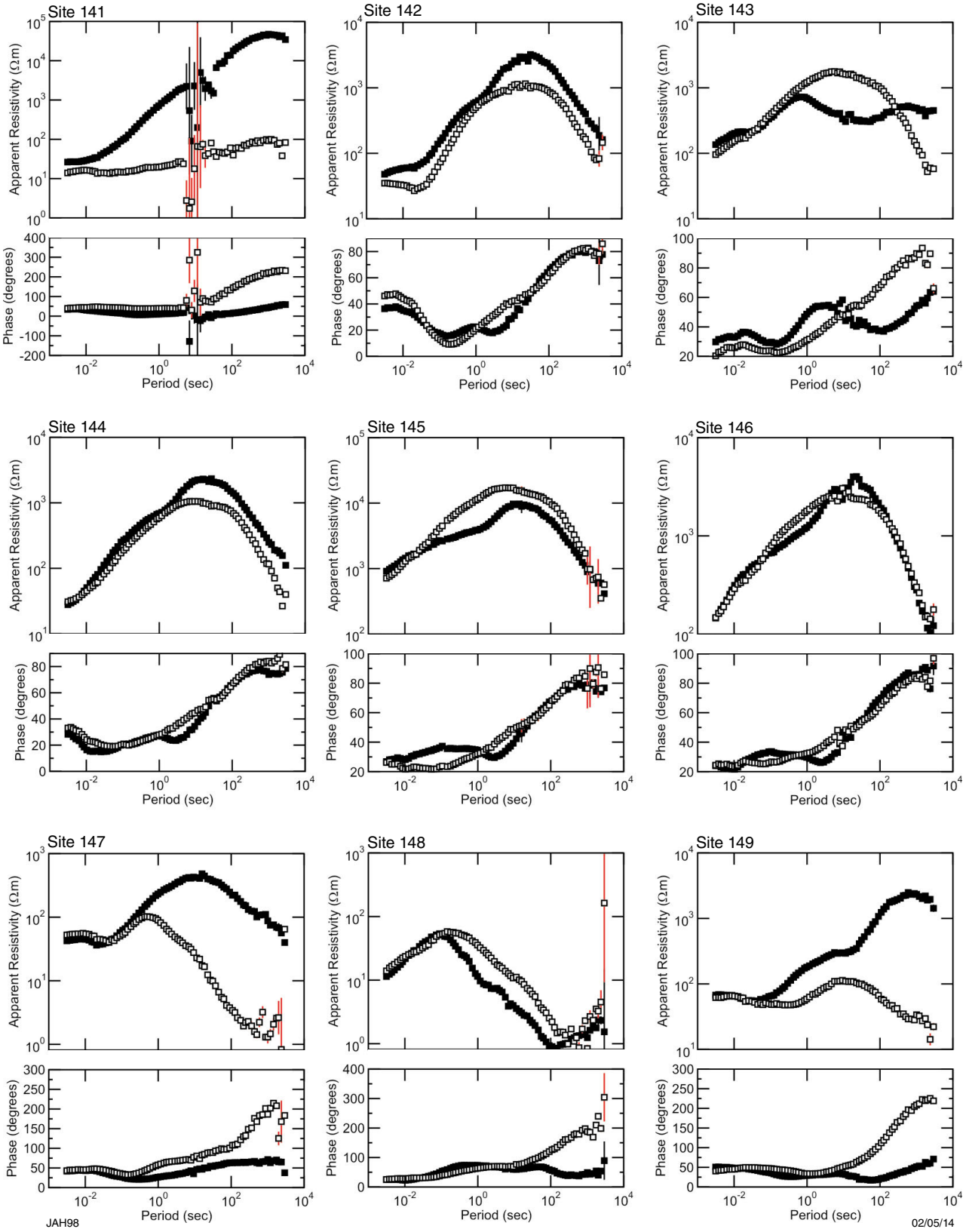
Site 141
Site 142
Site 143
Site 144
Site 145
Site 146
Site 147
Site 148
Site 149
Apparent Resistivity (Ωm)
Phase (degrees)
Period (sec)
JAH98
02/05/14

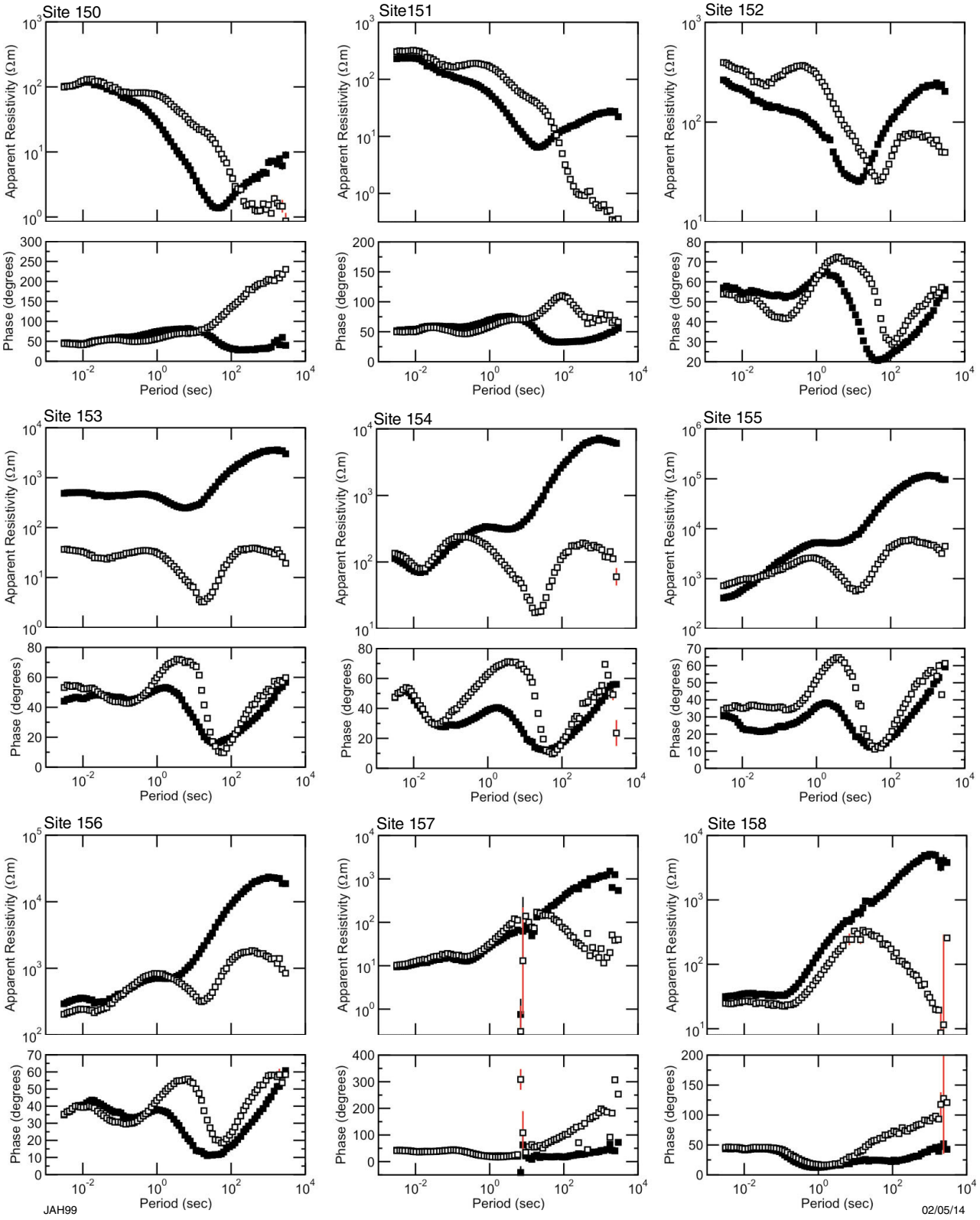
Site 150
Site151
Site 152
Site 153
Site 154
Site 155
Site 156
Site 157
Site 158
Apparent Resistivity (Ωm)
Phase (degrees)
Period (sec)
JAH99
02/05/14

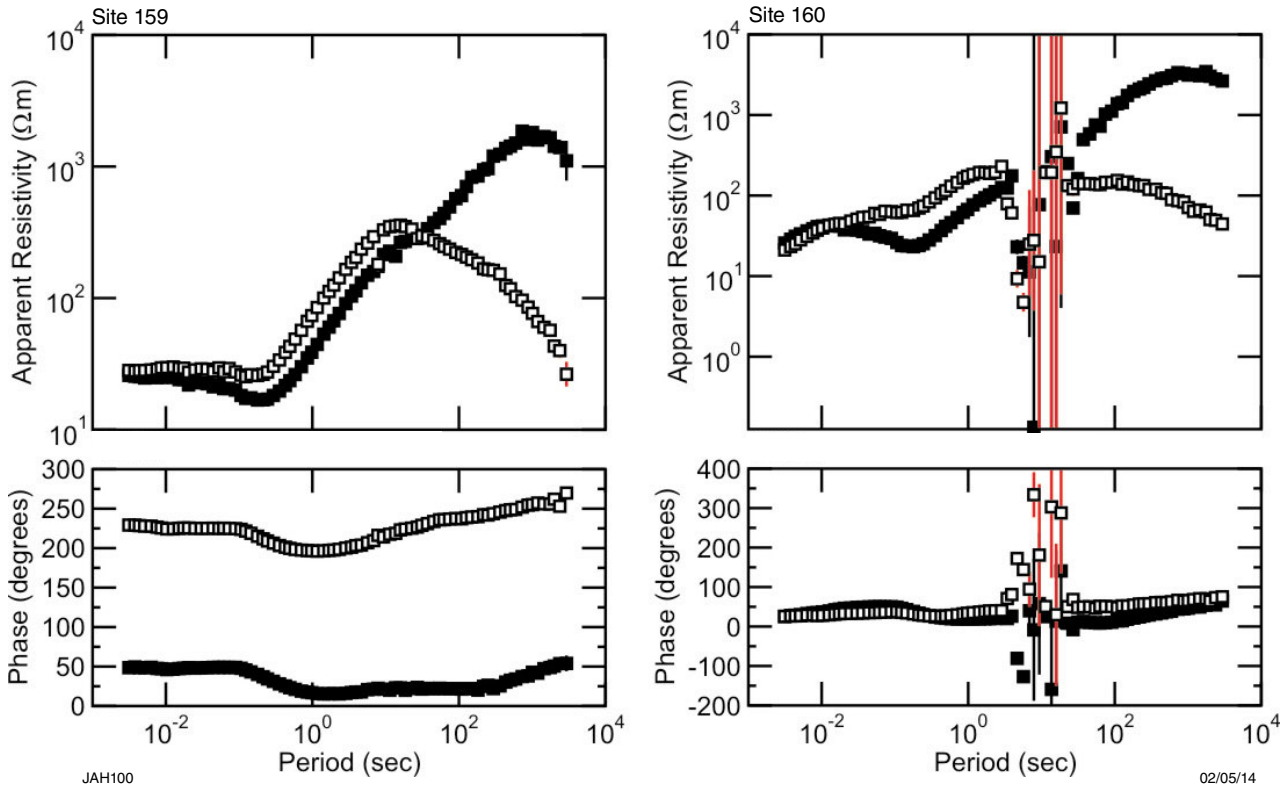
Site 159
Site 160
Apparent Resistivity (Ωm)
Phase (degrees)
Period (sec)
JAH100
02/05/14

The magnetotelluric (MT) method is a deep-penetrating, natural source electromagnetic technique used to image the electrical conductivity structure of the Earth's crust and upper mantle. An MT survey, comprising 155 stations, was completed in the Kimberley region in 2012. The survey was conducted along a southwest–northeast traverse extending from the Canning Basin, through the King Leopold Orogen, across the Kimberley Basin, and through the northern part of the Halls Creek Orogen. A second north-northwest trending traverse extends from the centre to the northern extent of the Kimberley Basin. The principal reason for the survey was to investigate the crustal architecture of the concealed basement of the Kimberley Craton, and the geometry of major tectonic structures within the adjacent King Leopold and Halls Creek Orogens. 2D modelling reveals the approximately 5 km-thick sedimentary and volcanic succession of the Kimberley Basin to be a conductive upper layer, which is underlain by resistive upper crust to depths of 15–35 km. Several steeply dipping, less resistive features in the upper crust identified in the MT model correlate with the location of known faults and major structural boundaries. A conductive lower crust appears to be discontinuous at, or near, major inferred crustal block boundaries. Along the eastern margin of the Kimberley Basin, a northwest-dipping resistive slab extending from the surface to at least 60 km depth is interpreted as ancient lithospheric material subducted during the Halls Creek Orogeny. The MT method is demonstrated to be a viable means of mapping the deep-crustal structure of the Kimberley Craton; however, variable electric strike directions suggest the need for 3D modelling of the data.

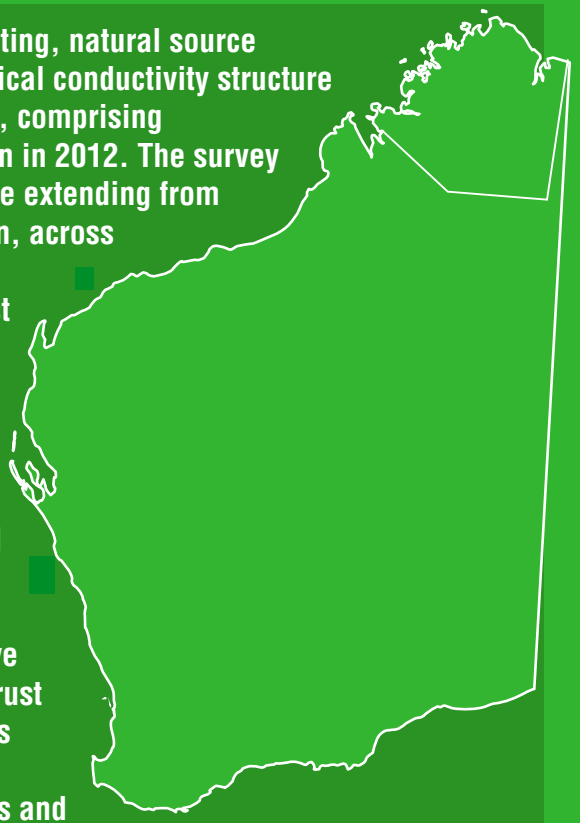

Further details of geological products and maps produced by the Geological Survey of Western Australia are available from:

Information Centre
Department of Mines and Petroleum
100 Plain Street
EAST PERTH WA 6004
Phone: (08) 9222 3459 Fax: (08) 9222 3444

www.dmp.wa.gov.au/GSWApublications

SPRATT et al.

A MAGNETOTELLURIC SURVEY ACROSS THE KIMBERLEY CRATON, NORTHERN WESTERN AUSTRALIA

REPORT 136